

Department of Physics and Astronomy

University of Heidelberg

Master thesis

in Physics

submitted by

Jonas Schulz

born in Werneck

2014

**Spin dynamics and active atom interferometry
with Bose-Einstein condensates**

This Master thesis has been carried out by Jonas Schulz

at the

Kirchhoff-Institute for Physics

under the supervision of

Prof. Dr. Markus K. Oberthaler

Spin dynamics and active atom interferometry with Bose-Einstein condensates:

In this thesis the dynamics caused by spin-changing collisions (SCC) and the realisation of an active non-linear interferometer in a spinor Bose-Einstein condensate of ^{87}Rb are studied.

We show the population growth of initially empty spin states (side modes) by pairwise scattering of atoms from a single spin mode in the course of an SCC-evolution. Numerical simulations of the dynamics are compared with experimental results showing good qualitative agreement. We demonstrate conservation of magnetisation despite large fluctuations in the atom numbers inside the magnetic sub states in the experiment.

An interferometer with active beam splitters is realised by two subsequent periods of SCC with intermediate phase evolution. Depending on the accumulated phase these are enhanced or reversed. A theory valid in the limit of a small side mode population (non-depleted regime) and based on the $SU(1,1)$ -Lie-group is discussed. We observe the amplification and partial reversibility of the SCC as well as the qualitative behaviour of the phase sensitivity in the experiment. We find indications that the realised interferometer surpasses the standard-quantum-limit (SQL), as predicted by the theory.

Numerical simulations show that the interferometer theoretically surpasses the SQL even in the depleted regime.

Spindynamik und aktive Atominterferometrie mit Bose-Einstein Kondensaten:

In dieser Arbeit werden die Dynamik aufgrund von spinändernden Stößen und die Umsetzung eines aktiven nichtlinearen Interferometers in einem Spinor Bose-Einstein Kondensat aus ^{87}Rb untersucht.

Wir zeigen die Populationszunahme von anfänglich leeren Spinzuständen (Seitenmoden) durch paarweise Streuung von Atomen aus einer einzelnen Mode im Verlauf einer SCC-Evolution. Numerische Simulationen der Dynamik werden mit experimentellen Ergebnissen verglichen und zeigen eine gute qualitative Übereinstimmung. Wir demonstrieren die Erhaltung der Magnetisierung bei gleichzeitig großen Fluktuationen in der Atomzahl der magnetischen Unterzustände im Experiment.

Ein Interferometer mit aktiven Strahlteilern wird durch zwei aufeinander folgende Perioden spinändernder Stöße realisiert, welche sich abhängig von der dazwischen akkumulierten Phase verstärken oder umkehren. Eine im Grenzfall schwach besetzter Seitenmoden gültige Theorie auf Grundlage der $SU(1,1)$ -Lie-Gruppe wird behandelt. Wir beobachten experimentell die Verstärkung und teilweise Reversibilität der spinändernden-Stöße sowie den qualitativen Verlauf der Phasensensitivität. Wir finden Indizien dafür, dass das realisierte Interferometer das Standard-Quanten-Limit (SQL) übertrifft, wie von der Theorie vorher gesagt.

Numerische Simulationen zeigen, dass das Interferometer auch in dem Regime stark besetzter Seitenmoden das SQL theoretisch übertrifft.

Contents

Introduction	1
I. Spin changing collisions	3
I.1. Theory	4
I.1.1. The SCC Hamiltonian	4
I.1.2. Magnetic fields	9
I.1.3. Microwave dressing	13
I.1.4. Effective Hamiltonian for the SCC	16
I.2. Experiment	21
I.2.1. Atom number distribution in the course of SCC	22
I.2.2. Conservation of magnetisation during spin changing collisions	24
I.2.3. SCC-evolution in $F=2$	26
II. SU(1,1)-interferometer	28
II.1. Mach-Zehnder interferometer in SU(2)-group representation	30
II.2. Introduction to SU(1,1)	36
II.2.1. Action of K_x, K_y, K_z	38
II.2.2. Coherent states of SU(1,1)-group and visualisation on an hyperbolic surface	40
II.3. The ideal SU(1,1)-interferometer	43
II.3.1. Interferometric sequence	43
II.3.2. Phase sensitivity	48
II.4. Experimental results of the SU(1,1)-interferometer in the non-depleted regime	50
II.4.1. Interferometric fringes	50
II.4.2. Phase sensitivity	53
II.4.3. Varying the second dressing time in the SU(1,1)-interferometer	56
II.5. SU(1,1)-interferometer in the depletion regime	58
II.5.1. Fisher information	60
II.5.2. Experimental results	66
Summary	69
List of Figures	71
Bibliography	73

Introduction

Interferometers are among the most precise measurement devices available and used in a variety of applications such as gravimetry, detection of gravitational waves, atomic clocks and precise rotation measurements [1, 2, 3, 4, 5].

A prime example in optics is the Mach-Zehnder [6] interferometer. Light passing through a beam splitter is separated into two beams, each experiencing a phase evolution. They are then recombined by a second beam splitter. The emerging interference pattern depends on the relative phase between the two beams. The precision of measuring the accrued differential phase of this interferometer is characterised by the phase sensitivity whose classical limit is called the standard-quantum-limit (SQL). The SQL can be beaten enabling more precise measurements. One way of doing this is to feed entangled states into the input ports of the interferometer [7, 8]. An alternative approach is the exchange of the passive beam splitters by active ones. These active beam splitters feature a non-linear response on the incoming light known as parametric down conversion. This new kind of interferometer was theoretically discussed by [9, 10] in the framework of the $SU(1,1)$ -Lie group and is hence denoted as $SU(1,1)$ -interferometer. An optical non-linear $SU(1,1)$ -interferometer has already been experimentally realised by [11].

In this thesis, we will discuss the implementation of such an interferometer in a Bose-Einstein condensate (BEC) of ^{87}Rb . The experimental realisation of BECs [12, 13] was a major breakthrough in the field of atom optics. Using optical confinement for a BEC [14] enables experiments within the hyperfine states and opens up the route to observe the rich dynamics in the spin degree of freedom induced by interactions between the atoms.

In so called spin-changing collisions (SCC) two atoms scatter and change their internal spin state. During this process the energy as well as the sum of the magnetic quantum numbers are conserved. In an ultracold and strongly confined BEC there is only one spatial mode yielding restrictions of the possible scattering channels. A lot of theoretical [15, 16, 17, 18] and experimental [19, 20, 21, 22, 23, 24] research has been done on this subject. The SCC lead to coherent population transfer between the magnetic sub states and are the atomic counterpart to the optical process of parametric down conversion [25].

We use spin-changing collisions to realise an atomic SU(1,1)-interferometer. Our experiments are performed in the electronic ground state $5^2S_{\frac{1}{2}}$ of ^{87}Rb where the $F = 1$ hyperfine spin manifold forms a three level system with the magnetic sub states $|F = 1, m_F = -1, 0, +1\rangle$.

The subjects of this thesis are the dynamics of spin-changing-collisions and the realisation of an active interferometer with these. The content is organised as follows.

In the first chapter we will treat the underlying theory of the SCC, including discussions of the effect of magnetic fields and microwave radiation. The outcome of numerical calculations will be shown and compared to experimental results.

The second chapter is dedicated to the interferometer. We will discuss the underlying theory for the *non-depletion regime* in the framework of the SU(1,1)-group and develop a visualisation in analogue to the well-known Bloch sphere used for the SU(2)-group of rotations. The experimental implementation and latest results of the phase sensitivity in our interferometric measurements will be addressed.

We finish with numerical simulations in the *depleted regime* where the former theory fails, which indicate sensitivity improvement even beyond the SU(1,1) regime.

I. Spin changing collisions

In this chapter we cover the process of spin-changing collisions. We begin with general considerations about the scattering of two atoms with total spin $F = 1$ and the three magnetic substates with $m_F = -1, 0, +1$ as sketched in Fig.I.0.1a. Two particles in the incoming states $|F, \mu\rangle, |F, \nu\rangle$ scatter into the outgoing modes $|F, \alpha\rangle, |F, \beta\rangle$ via an intermediate two particle state $|\mathcal{F}, M_{\mathcal{F}}\rangle$. The collisional process we are interested in is shown in Fig.I.0.1b; two atoms in $|1, 0\rangle$ collide and change their magnetic substates to $|1, -1\rangle$ and $|1, +1\rangle$ or vice versa whereby the total magnetisation is conserved.

We start with a the theoretical description of our system. After introducing the Hamiltonian covering the SCC we discuss the hyperfine splitting in the electric ground state of ^{87}Rb due to a magnetic field – the well known Zeeman effect. The effect of microwave radiation and its important role for the control over the spin changing collisions will be addressed.

Having tackled the underlying theory, a short overview of the current setup used for the experimental implementation is given. At the end of the first chapter, we will present experimental results and a comparison to the theoretical approach.

We will see that the SCC lead to coherent population transfer between the magnetic substates. As pointed out by [25, 22] they are the atomic counterpart to the optical process of parametric down conversion.

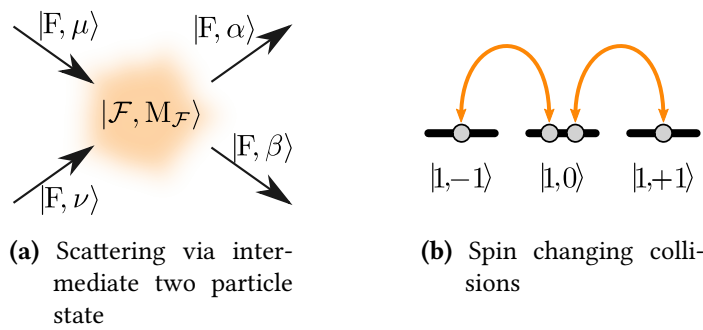


Fig. I.0.1. Schematic scattering process between two atoms. **a)** Two incoming atoms in the states $|F, \mu\rangle, |F, \nu\rangle$ are scattered into the outgoing states $|F, \alpha\rangle, |F, \beta\rangle$ via an intermediate two particle state $|\mathcal{F}, M_{\mathcal{F}}\rangle$. **b)** In the process of spin changing collisions two atoms in the $|1, 0\rangle$ mode collide and go into the $|1, -1\rangle$ and $|1, +1\rangle$ mode or vice versa.

Note that related experimental work has been performed in other experiments [21, 25, 26, 23, 24].

I.1. Theory

In the first part of this chapter we present a theoretical description of the spin changing collisions of a BEC of ^{87}Rb atoms in the $F = 1$ ground state. We start with the Hamiltonian in second quantized form and derive a more suitable form following [16, 19]. Afterwards the effect of magnetic fields and microwave radiation will be discussed.

I.1.1. The SCC Hamiltonian

The following process is considered: two incoming atoms in the states $|F, \mu\rangle, |F, \nu\rangle$ are scattered into the outgoing states $|F, \alpha\rangle, |F, \beta\rangle$ via an intermediate two particle state $|\mathcal{F}, M_{\mathcal{F}}\rangle$ (Fig.I.0.1a). We denote the strength of a particular scattering channel by $\Omega_{\alpha, \beta, \mu, \nu}$. The indices μ, ν stand for the initial modes, α, β for final modes of the two particles involved in the collision. Let $\hat{\Psi}_{\kappa}$ ($\hat{\Psi}_{\kappa}^{\dagger}$) be the atomic field annihilation (creation) operator for the hyperfine mode $\kappa = m_F = -1, 0, +1$. The Hamiltonian in second quantized form then reads [16]

$$\hat{H} = \underbrace{\sum_{\alpha} \int d^3x \hat{\Psi}_{\alpha}^{\dagger} (\hat{T} + V_T) \hat{\Psi}_{\alpha}}_{\text{kinetic and potential energy}} + \underbrace{\sum_{\alpha, \beta, \mu, \nu} \Omega_{\alpha, \beta, \mu, \nu} \int d^3x \hat{\Psi}_{\alpha}^{\dagger} \hat{\Psi}_{\beta}^{\dagger} \hat{\Psi}_{\mu} \hat{\Psi}_{\nu}}_{\text{interaction energy}}. \quad (\text{I.1.1})$$

The sums run over all magnetic substates κ in integer steps. The first term is the sum of the kinetic (\hat{T}) and potential (V_T) energy of all magnetic sublevels. The second term gives the interaction energy of the system. Since we have a dilute gas of ultracold atoms, we assume the dominant process to be s-wave scattering.

The coefficients $\Omega_{\alpha, \beta, \mu, \nu}$ are calculated using a two-body interaction model with a δ potential widely used in one component dilute BEC [16, 19]

$$U(\vec{x}_1, \vec{x}_2) = \delta(\vec{x}_1 - \vec{x}_2) \sum_{\mathcal{F}=0}^2 g_{\mathcal{F}} \sum_{M_{\mathcal{F}}=-\mathcal{F}}^{\mathcal{F}} \hat{\rho}_{\mathcal{F}, M_{\mathcal{F}}} \quad (\text{I.1.2})$$

$$\text{with } g_{\mathcal{F}} = \frac{4\pi\hbar^2 a_{\mathcal{F}}}{M}$$

$$\text{and } \hat{\rho}_{\mathcal{F}, M_{\mathcal{F}}} = |\mathcal{F}, M_{\mathcal{F}}\rangle \langle \mathcal{F}, M_{\mathcal{F}}|.$$

$\hat{\rho}_{\mathcal{F}, M_{\mathcal{F}}}$ is the projection operator onto the intermediate state with total spin \mathcal{F} and magnetic quantum number $M_{\mathcal{F}}$ formed by the two atoms involved in the collisions, each with spin $F = 1$. M is the atomic mass and $a_{\mathcal{F}}$ the s -wave scattering length in the respective channel.

The calculation Equ.I.1.2 is done by expanding the total spin state $|\mathcal{F}, M_{\mathcal{F}}\rangle$ in terms of the single atom basis vectors $|1, -1\rangle$, $|1, 0\rangle$ and $|1, +1\rangle$. Using the notation

$$\begin{aligned} |\mu, \nu\rangle &= |F = 1, m_F = \mu\rangle \otimes |F = 1, m_F = \nu\rangle \\ \langle\alpha, \beta| &= \langle F = 1, m_F = \alpha| \otimes \langle F = 1, m_F = \beta| \end{aligned}$$

one finds

$$|\mathcal{F} = 0, M_{\mathcal{F}} = 0\rangle = \frac{1}{\sqrt{3}} (|-1, +1\rangle - |0, 0\rangle + |+1, -1\rangle) \quad (\text{I.1.3})$$

and similar expressions for $|\mathcal{F} = 1, M_{\mathcal{F}} = -1, 0, +1\rangle$ and $|\mathcal{F} = 2, M_{\mathcal{F}} = -2, \dots, +2\rangle$.

The $|\mathcal{F} = 1, M_{\mathcal{F}} = -1, 0, +1\rangle$ spin wave function is antisymmetric under particle exchange whilst the other two are symmetric. Therefore the $|\mathcal{F} = 1, M_{\mathcal{F}} = -1, 0, +1\rangle$ channel is forbidden since the in- and outgoing states in s -wave scattering have a symmetric spatial wave function and the particles are bosons, meaning that the total wave function has to be symmetric. Another way to write Equ.I.1.2 is then [15, 27]

$$\begin{aligned} U(\vec{x}_1, \vec{x}_2) &= \delta(\vec{x}_1 - \vec{x}_2) (c_0 + c_2 \vec{F}_1 \vec{F}_2) \\ \text{with } c_0 &= \frac{g_0 + 2g_2}{3} \quad c_2 = \frac{g_2 - g_0}{3}, \end{aligned} \quad (\text{I.1.4})$$

where the \vec{F}_i are the spin operators of the two participating particles¹ and the expression for the interaction coefficients reads

$$\Omega_{\alpha, \beta, \mu, \nu} = \langle\alpha, \beta| \otimes \langle\phi_{\alpha}, \phi_{\beta}| U(\vec{x}_1, \vec{x}_2) |\phi_{\mu}, \phi_{\nu}\rangle \otimes |\mu, \nu\rangle. \quad (\text{I.1.5})$$

With the assumption that throughout the whole scattering process the atoms neither can leave the trap nor be excited to an higher spatial mode, the spatial state $|\phi\rangle$ of the single particles remains the same and therefore $|\phi_{\alpha}\rangle = |\phi_{\mu}\rangle$ and $|\phi_{\beta}\rangle = |\phi_{\nu}\rangle$. The spatial integral over the δ -potential yields $\int d^3x |\phi_{\alpha}(\vec{x})|^2 |\phi_{\beta}(\vec{x})|^2$. With this, Equ.I.1.5 simplifies to

$$\Omega_{\alpha, \beta, \mu, \nu} = \sum_{\mathcal{F}=0}^2 g_{\mathcal{F}} \sum_{M_{\mathcal{F}}=-\mathcal{F}}^{\mathcal{F}} \langle\alpha, \beta| \hat{\rho}_{\mathcal{F}, M_{\mathcal{F}}} |\mu, \nu\rangle \cdot \int d^3x |\phi_{\alpha}(\vec{x})|^2 |\phi_{\beta}(\vec{x})|^2. \quad (\text{I.1.6})$$

¹A similar expression for the $f = 2$ hyperfine manifold can be found in [28].

The expression $\langle \alpha, \beta | \hat{\rho}_{\mathcal{F}, M_{\mathcal{F}}} | \mu, \nu \rangle$ shows the connection of the initial ($|\mu, \nu\rangle$) and final ($|\alpha, \beta\rangle$) states via the intermediate two particle state $|\mathcal{F}, M_{\mathcal{F}}\rangle$. $\Omega_{\alpha, \beta, \mu, \nu}$ is then given by the sum over all possible scattering channels, i. e. all possible intermediate states $|\mathcal{F}, M_{\mathcal{F}}\rangle$ multiplied with the factor $g_{\mathcal{F}}$ which characterises the strength of the respective channel.

With this the Hamiltonian in Equ.I.1.1 can be split into two parts [16]

$$\hat{H} = \hat{H}_S + \hat{H}_N. \quad (\text{I.1.7})$$

The first term, \hat{H}_S , is symmetric and remains unchanged for any interchange of the spin component while the second term, \hat{H}_N , is non-symmetric. The two parts read [16]

$$\hat{H}_S = \sum_{\alpha} \int d^3x \hat{\Psi}_{\alpha}^{\dagger} (\hat{T} + \hat{V}_T) \hat{\Psi}_{\alpha} + \frac{c_0}{2} \sum_{\alpha, \beta} \int d^3x \hat{\Psi}_{\alpha}^{\dagger} \hat{\Psi}_{\beta}^{\dagger} \hat{\Psi}_{\alpha} \hat{\Psi}_{\beta} \quad (\text{I.1.8})$$

and

$$\begin{aligned} \hat{H}_N = \frac{c_2}{2} \int d^3x & \left(\hat{\Psi}_{+}^{\dagger} \hat{\Psi}_{+}^{\dagger} \hat{\Psi}_{+} \hat{\Psi}_{+} + \hat{\Psi}_{-}^{\dagger} \hat{\Psi}_{-}^{\dagger} \hat{\Psi}_{-} \hat{\Psi}_{-} \right. \\ & + 2\hat{\Psi}_{+}^{\dagger} \hat{\Psi}_{0}^{\dagger} \hat{\Psi}_{+} \hat{\Psi}_{0} + 2\hat{\Psi}_{-}^{\dagger} \hat{\Psi}_{0}^{\dagger} \hat{\Psi}_{-} \hat{\Psi}_{0} \\ & + 2\hat{\Psi}_{0}^{\dagger} \hat{\Psi}_{0}^{\dagger} \hat{\Psi}_{+} \hat{\Psi}_{-} + 2\hat{\Psi}_{+}^{\dagger} \hat{\Psi}_{-}^{\dagger} \hat{\Psi}_{0} \hat{\Psi}_{0} \\ & \left. - 2\hat{\Psi}_{+}^{\dagger} \hat{\Psi}_{-}^{\dagger} \hat{\Psi}_{+} \hat{\Psi}_{-} \right). \end{aligned} \quad (\text{I.1.9})$$

Approximation of the spatial wave function

For approximately equal scattering lengths of the two entering channels one has $|c_0| \gg |c_2|$. This holds for the $F = 1$ state in ^{87}Rb as can be seen in [29] ($a_0 \approx 101.8 a_B$ and $a_2 \approx 100.4 a_B$, a_B being the Bohr radius). Therefore the symmetric part \hat{H}_S of the Hamiltonian is dominating and the spatial wave function of the individual spin components are similar, i. e.

$$\Phi_{\kappa}(\vec{x}) \approx \Phi(\vec{x}) \quad \kappa = 0, \pm 1. \quad (\text{I.1.10})$$

With the usual creation and annihilation operators satisfying the bosonic commutation relation

$$[\hat{a}_{\kappa}, \hat{a}_{\gamma}] = 0 \quad [\hat{a}_{\kappa}, \hat{a}_{\gamma}^{\dagger}] = \delta_{\kappa\gamma} \quad (\text{I.1.11})$$

the field operators are approximated by

$$\hat{\Psi}_{\kappa} \approx \hat{a}_{\kappa} \Phi(\vec{x}) \quad \kappa = 0, \pm 1. \quad (\text{I.1.12})$$

One method to find an estimate for $\Phi(\vec{x})$ is to use the Gross-Pitaevskii equation (GPE). It is an ansatz to get the spatial wave function of one single particle in a dilute gas of weakly interacting particles where the interactions are assumed to arise from the background of the other particles [30].

$$\left(\underbrace{\hat{T} + \hat{V}}_{\text{kinetic and potential energy}} + \underbrace{c_0 N |\Phi|^2}_{\text{interaction term}} \right) \Phi = \mu \Phi. \quad (\text{I.1.13})$$

The interactions are described by the product of c_0 (since \hat{H}_S is the dominating part in Equ.I.1.7) and the density $N|\Phi|^2$ of the atomic cloud. Thus the GPE is a mean field approach and μ is called the mean field energy or the chemical potential.

With the total atom number operator

$$\hat{N} = \hat{a}_-^\dagger \hat{a}_- + \hat{a}_0^\dagger \hat{a}_0 + \hat{a}_+^\dagger \hat{a}_+, \quad (\text{I.1.14})$$

we can now rewrite the symmetric Hamiltonian Equ.I.1.8 into

$$\hat{H}_S = \sum_{\alpha} \int d^3x \hat{\Psi}_{\alpha}^{\dagger} \left[(\hat{T} + \hat{V}_T) + \frac{c_0}{2} \underbrace{\sum_{\beta} \hat{\Psi}_{\beta}^{\dagger} \hat{\Psi}_{\beta}}_{=|\Phi(\vec{x})|^2 \hat{N}} \right] \hat{\Psi}_{\alpha} = \mu \hat{N} - \lambda_S \hat{N}(\hat{N} - 1), \quad (\text{I.1.15})$$

where we used the GPE in the last step. The non-symmetric part of Equ.I.1.7 becomes

$$\begin{aligned} \hat{H}_N = \lambda_N & \left(\hat{a}_+^\dagger \hat{a}_+^\dagger \hat{a}_+ \hat{a}_+ + \hat{a}_-^\dagger \hat{a}_-^\dagger \hat{a}_- \hat{a}_- \right. \\ & + 2\hat{a}_+^\dagger \hat{a}_0^\dagger \hat{a}_+ \hat{a}_0 + 2\hat{a}_-^\dagger \hat{a}_0^\dagger \hat{a}_- \hat{a}_0 \\ & + 2\hat{a}_0^\dagger \hat{a}_0^\dagger \hat{a}_+ \hat{a}_- + 2\hat{a}_+^\dagger \hat{a}_-^\dagger \hat{a}_0 \hat{a}_0 \\ & \left. - 2\hat{a}_+^\dagger \hat{a}_-^\dagger \hat{a}_+ \hat{a}_- \right). \end{aligned} \quad (\text{I.1.16})$$

In Equ.I.1.15 and Equ.I.1.16 we used the new defined coupling parameters

$$\lambda_{S/N} = \frac{c_0/2}{2} \int d^3x |\Phi(\vec{x})|^4. \quad (\text{I.1.17})$$

The symmetric part of the Hamiltonian depends only on the total number of atoms. Under the assumption that there are no losses during the whole experimental sequence the total atom number is conserved and the spin dynamics are fully determined by the non-symmetric part \hat{H}_N . Therefore we will focus on \hat{H}_N in the following.

For a detailed discussion of the calculation of λ_N see [31]. Here we only want to state that λ_N

decreases with increasing total atom number.

New quantum numbers for the Hamiltonian

A possible set of quantum numbers is (n_+, n_0, n_-) which are the population numbers in the three submodes. For the further proceeding we adopt the notation from [32] and introduce an alternative set of quantum numbers (η, M, N) and their respective operators. The two sets are connected via

$$\hat{\eta} = \hat{n}_- + \hat{n}_+ \quad \Rightarrow \quad \eta = n_- + n_+ \quad (\text{I.1.18})$$

$$\hat{M} = \hat{n}_- - \hat{n}_+ \quad \Rightarrow \quad M = n_- - n_+ \quad (\text{I.1.19})$$

$$\hat{N} = \hat{n}_- + \hat{n}_0 + \hat{n}_+ \quad \Rightarrow \quad N = n_- + n_0 + n_+ \quad (\text{I.1.20})$$

$$\text{with } \hat{n}_i = \hat{a}_i^\dagger \hat{a}_i.$$

η is the sum of the side mode populations, M the magnetization and N the total atom number in the system. These are eigenoperators of a state $|\eta, M, N\rangle$ with the respective quantum numbers. Additionally we define the operators

$$\hat{\eta}_+ = \hat{a}_0 \hat{a}_0 \hat{a}_+^\dagger \hat{a}_-^\dagger \quad \hat{\eta}_- = \hat{a}_0^\dagger \hat{a}_0^\dagger \hat{a}_+ \hat{a}_-, \quad (\text{I.1.21})$$

which represent the scattering of two atoms in the zero mode into two atoms in the side modes ($\hat{\eta}_+$) and vice versa ($\hat{\eta}_-$). The actions of these on a state $|\eta, M, N\rangle$ are

$$\hat{\eta}_+ |\eta, M, N\rangle = \frac{1}{2} \sqrt{(N - \eta - 1)(N - \eta) ((\eta + 2)^2 - M^2)} |\eta + 2, M, N\rangle \quad (\text{I.1.22})$$

$$\hat{\eta}_- |\eta, M, N\rangle = \frac{1}{2} \sqrt{(N - \eta + 2)(N - \eta + 1) ((\eta^2 + M^2))} |\eta - 2, M, N\rangle. \quad (\text{I.1.23})$$

With these new operators \hat{H}_N can be expressed as follows

$$\hat{H}_N = \lambda \left[\hat{M}^2 + (2\hat{N} - 2\hat{\eta} - 1) \hat{\eta} + 2(\hat{\eta}_+ + \hat{\eta}_-) \right] \quad (\text{I.1.24})$$

where we used $\lambda = \lambda_N$.

So far we introduced the system and derived a convenient form of the important part of the Hamiltonian. In the following two sections we will approach our actual experimental situation

and have a closer look at the additional terms in the Hamiltonian which arise from magnetic fields and microwave radiation. These will allow us to control the spin changing collisions.

I.1.2. Magnetic fields

We will now discuss the effect of an external magnetic field on the electronic ground state of ^{87}Rb and look at its consequences for the SCC. The informations given follow mainly the derivation in [33].

Without any excitation ^{87}Rb has one single electron in the outermost s shell. The total electron spin is $S = \frac{1}{2}$ and the orbital angular momentum $L = 0$, resulting in an angular momentum of $J = \frac{1}{2}$. Thus the electronic ground state is $5^2S_{\frac{1}{2}}$. Due to the nuclear spin of $I = \frac{3}{2}$ the ground state has two hyperfine levels with total angular momentum $F = 1$ and $F = 2$ which have a degeneracy of $2F + 1$ in the absence of external fields. The nuclear magnetic moment is $\vec{\mu}_I = -\frac{\mu_B}{h}\vec{I}$ with the nuclear Bohr magneton μ_B . Thus the two hyperfine levels are energetically separated to first order by

$$\hat{H}_{\text{hfs}} = -\vec{\mu}_I \vec{B}_J \approx A_{\text{hfs}} \vec{I} \vec{J} \quad (\text{I.1.25})$$

$$= \frac{1}{2} A_{\text{hfs}} [F(F + 1) - I(I + 1) - J(J + 1)]. \quad (\text{I.1.26})$$

\vec{B}_J is the magnetic field experienced by the nucleus due to the angular momentum \vec{J} of the outer electron and $A_{\text{hfs}} \approx 3.417$ GHz the magnetic dipole constant of the $5^2S_{\frac{1}{2}}$ state of ^{87}Rb . This results in an energy splitting of the two hyperfine states of

$$\Delta E_{F=2, F=1} \approx 6.8 \text{ GHz}. \quad (\text{I.1.27})$$

Figure I.1.1 shows the hyperfine structure of the electronic ground state schematically. For a general introduction to fine and hyperfine structure see [34]. For specific details about ^{87}Rb and a table of constants see [33].

By applying an external magnetic field \vec{B}_{ext} one gets additional energy shifts since the magnetic moment couples with \vec{B}_{ext} . These are given by $\Delta E = -\vec{\mu}_F \vec{B}_{\text{ext}}$. As long as ΔE is small compared to the hyperfine splitting, the angular momentum \vec{J} and the nuclear spin \vec{I} do not decouple and F remains a good quantum number. The degeneracy is broken and the two hyperfine levels split into the $|F = 1, m_F = -1, 0, +1\rangle$ and $|F = 2, m_F = -2, \dots, +2\rangle$ magnetic substates respectively. This is the well known Zeeman effect and schematically shown in Fig.I.1.1. For large external magnetic fields \vec{J} and \vec{I} decouple and the hyperfine splitting can be treated as small perturbation to the strong field eigenstates $|J, m_J; I, m_I\rangle$.

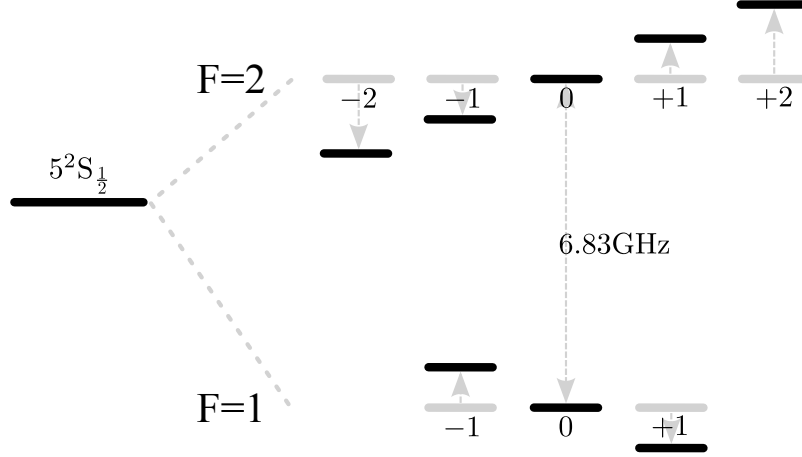


Fig. I.1.1. Electronic ground state of ^{87}Rb and its hyperfine levels in an external magnetic field. The nuclear spin of ^{87}Rb is $I = \frac{3}{2}$ and its electronic ground state $5^2S_{\frac{1}{2}}$ resulting in two hyperfine levels separated by ≈ 6.83 GHz. Applying an external magnetic field breaks the degeneracy of each hyperfine level by shifting the energy of the magnetic substates by $\Delta E = -\vec{\mu}\vec{B}$ resulting in $3 + 5$ distinct levels.

Here we are interested in an intermediate regime where the energy is given by the Breit-Rabi formula which can be used on the $5^2S_{\frac{1}{2}}$ level. It reads

$$E_{F, m_F} = -\frac{\Delta E_{\text{hfs}}}{2(2I+1)} + g_I \mu_B m_F B \pm \frac{\Delta E_{\text{hfs}}}{2} \left(1 + \frac{4}{2I+1} m_F + x^2 \right)^{\frac{1}{2}} \quad (\text{I.1.28})$$

with $m_F = -|m_I \pm m_J|, \dots, +|m_I \pm m_J|$

$$x = \frac{(g_J - g_I) \mu_B B}{\Delta E_{\text{hfs}}}$$

$$\Delta E_{\text{hfs}} = A_{\text{hfs}} \left(I + \frac{1}{2} \right).$$

The $g_{J/I}$ are the Landé factors of the angular momentum and the nuclear spin. Choosing the positive sign yields $m_F = -2, \dots, +2$ corresponding to the $F = 2$ manifold whereas the negative sign gives the result for the $F = 1$ manifold. After Taylor expansion up to second order in the magnetic field B one gets the following expression

$$\begin{aligned}
 E_{F, m_F} &= -\frac{\Delta E_{\text{hfs}}}{8} \pm \frac{\Delta E_{\text{hfs}}}{2} \pm p_{m_F} B \pm q_{m_F} B^2 + \mathcal{O}(B^3) \quad (\text{I.1.29}) \\
 \text{with } p_{m_F} &= \mu_B \left[\frac{1}{4}(g_J - g_I) \pm g_I \right] m_F \\
 q_{m_F} &= \frac{(g_J - g_I)^2}{4\Delta E_{\text{hfs}}} \mu_B^2 \left[1 - \left(\frac{m_F}{2} \right)^2 \right].
 \end{aligned}$$

With the same conditions for the \pm as in Equ.I.1.28. The first two terms give the energy shifts due to the hyperfine splitting relative to the $5^2S_{\frac{1}{2}}$ state in the absence of any external magnetic field for the $F = 1$ and $F = 2$ hyperfine state respectively.

The third term is linear in the magnetic field and is called the linear Zeeman effect. It is important to note that the direction of the energy shift depends on the sign of the magnetic quantum number in the m_F substate. Hence the two different F manifolds experience opposing shifts in their corresponding m_F substates.

The fourth term is quadratic in the magnetic field and called the quadratic Zeeman effect. The direction of the energy shift depends only on the hyperfine level. It is positive for $F = 2$ and negative for $F = 1$ levels. However, the strength of the shift in each magnetic substate depends on the absolute value of the magnetic quantum number. To shorten the equation we introduce the two factors p_{m_F} and q_{m_F} .

With values in [33] one gets for p_{m_F} and q_{m_F}

$$p_{m_F} = \begin{cases} 699.58 \text{ kHz G}^{-1} \cdot m_F & F = 2 \\ 702.37 \text{ kHz G}^{-1} \cdot m_F & F = 1 \end{cases} \quad q_{m_F} = \begin{cases} 287.57 \text{ Hz/G}^2 \cdot 1 & |m_F| = 0 \\ 287.57 \text{ Hz/G}^2 \cdot \frac{3}{4} & |m_F| = 1 \\ 0 & |m_F| = 2 \end{cases} \quad (\text{I.1.30})$$

In Fig.I.1.2 the contributions of the linear and the quadratic Zeeman effect to the overall energy shift are shown.

Let us now consider the influence of the external magnetic field on the process of spin changing collisions in the $F = 1$ manifold. We look at the collision of two atoms each in the $|1, 0\rangle$ state. Due to conservation of the total magnetization either both atoms remain in $|1, 0\rangle$ or one atom ends in $|1, +1\rangle$ state whilst the other goes into $|1, -1\rangle$. Since the first process does not change the spin states it is not of any interest here and we will focus on the second one.

We begin with the linear Zeeman effect. The energy gained by the atom going in the $|1, +1\rangle$ state is taken by the other atom to reach the energetically higher $|1, -1\rangle$ state, which is shifted by

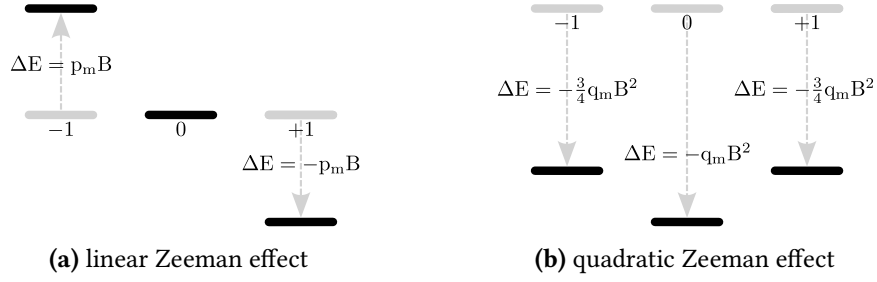


Fig. I.1.2. Linear and quadratic Zeeman effect in $F = 1$. **a)** The direction of the energy shift due to the linear Zeeman effect depends on the sign of the magnetic quantum number m_F . The two magnetic substates $|1, -1\rangle$ and $|1, +1\rangle$ are shifted by the same amount $p_m \approx 702.37 \text{ kHz G}^{-1} \cdot B$ but in opposite direction whilst the energy of $|1, 0\rangle$ remains unchanged. During the spin changing collisions the energy gained by the atom going from $|1, 0\rangle$ to $|1, +1\rangle$ is used to raise the other atom to the $|1, -1\rangle$ state. The total energy is conserved and the linear Zeeman effect does not hinder the SCC. **b)** The quadratic Zeeman effect leads to a shift downwards in the energy of all levels resulting in a net energy difference of $q_z \approx 71.89 \text{ Hz/G}^2 \cdot B^2$ between $|1, 0\rangle$ and $|1, +1\rangle, |1, -1\rangle$. In this case for the spin changing collisions process to work, both atoms have to gain energy to reach the higher states. Therefore the spin changing collisions are suppressed by the quadratic Zeeman effect due to the consequential violation of energy conservation.

the same amount, but in opposite direction as the $|1, +1\rangle$ state (Fig.I.1.2a). If only the linear Zeeman effect were present we had therefore conservation of magnetization as well as conservation of energy.

This is no longer the case if we take into account the quadratic Zeeman effect. All sublevels in the $F=1$ manifold shift in the same direction such that the $|1, \pm 1\rangle$ states are equal in energy but lie above the $|1, 0\rangle$ state (neglecting the linear Zeeman effect since it plays no role for the process, Fig.I.1.2b). Two atoms initially in $|1, 0\rangle$ would need to gain energy to reach the sublevels in the $F=1$ manifold and therefore the quadratic Zeeman effect hinders the process of spin changing collisions due to violation of energy conservation. The energy difference between two atoms in the sublevels and two atoms in $|1, 0\rangle$ is

$$\Delta E = 2 \cdot (q_{m_F=0} - q_{m_F=1})B^2 = 2 \cdot 71.89 \text{ Hz/G}^2 B^2 = 2 \cdot q_z B^2 \quad (\text{I.1.31})$$

where we defined $q_z := 71.89 \text{ Hz/G}^2$. We want to finish this section with the extension of the Hamiltonian Equ.I.1.24 by two new terms due an external magnetic field. The linear Zeeman effect changes the energy proportional to the total magnetization $\hat{M} = \hat{n}_- - \hat{n}_+$ whereas the quadratic Zeeman effect contributes with a term proportional to the sum of the atoms in the substates, $\hat{\eta} = \hat{n}_- + \hat{n}_+$, if we assume the $|1, 0\rangle$ state to lie at the zero energy level. With these the Hamiltonian Equ.I.1.24 reads

$$\hat{H}_N = \lambda \left[\hat{M}^2 + (2\hat{N} - 2\hat{\eta} - 1) \hat{\eta} + 2(\hat{\eta}_+ + \hat{\eta}_-) \right] + p_{m_F=1} B \hat{M} + q_z B^2 \hat{\eta} \quad (\text{I.1.32})$$

In the next section we will look at level shifts caused by microwave radiation and see how it can be used to overcome the lack of energy due to the quadratic Zeeman effect.

I.1.3. Microwave dressing

In this section we want to introduce the effect of microwave radiation on the atoms. We will follow mainly [35, 36] and a comprehensive treatment of the theory can be found there.

Let us start with a general discussion of an atomic two level system under the influence of electromagnetic radiation. In the dipole approximation the interaction between atomic system and radiation field can be described by

$$\hat{H}_{\text{int}} = -\vec{d}\vec{E} \quad (\text{I.1.33})$$

where \vec{d} is the atomic dipole operator and \vec{E} the electric field, which we assume to be single mode in the frequency.

We consider the ground state together with $n+1$ photons of the microwave field, $|g, n+1\rangle$, and the excited state with one photon less, $|e, n\rangle$ (Fig.I.1.3). The difference in energy of these newly introduced states depends on the detuning $\delta = \omega - \omega_0$ of the radiation with frequency ω relative to the resonance frequency $\omega_0 = (E_{|e\rangle} - E_{|g\rangle})/\hbar$ of the original two level system. A

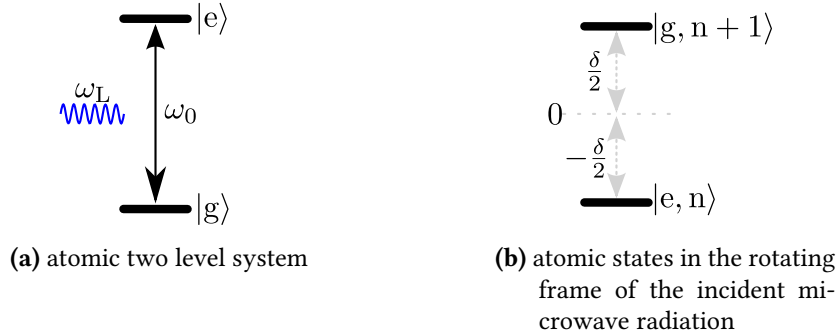


Fig. I.1.3. Atomic two level system with incident microwave radiation. **a)** In the bare state picture the excited state lies energetically above the ground state and the incident microwave radiation (ω_L) and atomic system are treated separately. The energy difference between the two atomic states is the resonance frequency ω_0 . **b)** In the dressed state picture the atomic levels and microwave photons are coupled to the states $|e, n\rangle$ and $|g, n+1\rangle$, building a ladder of state pairs for the different photon numbers n . In the rotating frame of the incident microwave the energy difference of the states in one specific n -manifold is given by the detuning $\delta = \omega_L - \omega_0$. Shown here is the case for blue detuning where $\delta > 0$.

positive value of δ is also referred to as blue detuned since the wavelength of the photons of the radiation field is smaller than the two level resonance wavelength. The opposite case is called red detuned. Applying the rotating wave approximation [35] the Hamiltonian of this system reads

$$\hat{H} = \omega \hat{a}^\dagger \hat{a} + \frac{1}{2} \omega_0 \sigma_z + g (\sigma_+ \hat{a} + \hat{a}^\dagger \sigma_-) \quad (\text{I.1.34})$$

where \hat{a} and \hat{a}^\dagger are the annihilation and creation operator for photons of the electromagnetic field and $\sigma_{\pm, z}$ act on the atomic states as follows

$$\sigma_+ = |e\rangle \langle g| \quad \sigma_- = |g\rangle \langle e| \quad \sigma_z = |e\rangle \langle e| - |g\rangle \langle g|. \quad (\text{I.1.35})$$

The coupling constant g can be calculated with

$$g = \frac{\langle e, n | \hat{H}_{\text{int}} | g, n+1 \rangle}{\sqrt{n+1}} = \frac{\langle g, n+1 | \hat{H}_{\text{int}} | e, n \rangle}{\sqrt{n+1}}. \quad (\text{I.1.36})$$

We choose the basis

$$|g, n+1\rangle \mapsto \begin{pmatrix} 1 \\ 0 \end{pmatrix} \quad |e, n\rangle \mapsto \begin{pmatrix} 0 \\ 1 \end{pmatrix} \quad (\text{I.1.37})$$

with which the Hamiltonian in the specific n photon manifold can be written in the form

$$\hat{H} = \frac{1}{2} \begin{pmatrix} \delta & \Omega \\ \Omega & -\delta \end{pmatrix} + \omega \left(n + \frac{1}{2} \right) \mathbb{1} \quad (\text{I.1.38})$$

where $\Omega = g\sqrt{n+1} = \langle e, n | \hat{H}_{\text{int}} | g, n+1 \rangle$ is the resonant Rabi frequency. We see that for large photon numbers n the Rabi frequency Ω is proportional to the square root of the photon number, i. e. proportional to the square root of the intensity of the radiation field. The eigenenergies are calculated to be

$$\epsilon_{n, \pm} = \omega \left(n + \frac{1}{2} \right) \pm \frac{1}{2} \sqrt{\delta^2 + \Omega^2} \quad (\text{I.1.39})$$

and the corresponding eigenstates are

$$|+\rangle = \sin(\theta) |g, n+1\rangle + \cos(\theta) |e, n\rangle \quad (\text{I.1.40})$$

$$|-\rangle = \cos(\theta) |g, n+1\rangle - \sin(\theta) |e, n\rangle \quad (\text{I.1.41})$$

$$\text{with} \quad \tan(2\theta) = -\frac{\Omega}{\delta}.$$

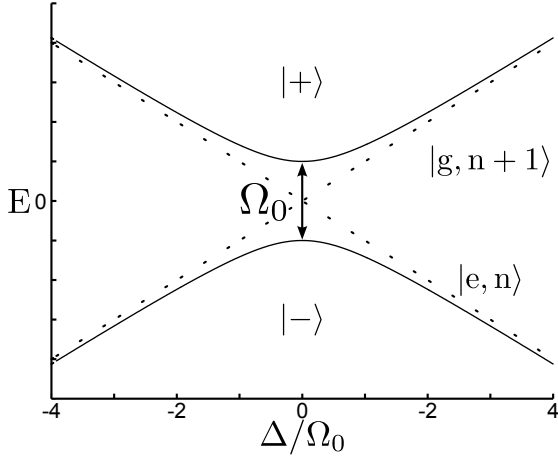


Fig. I.1.4 The energies of dressed states ($|\pm\rangle$, solid lines) depend on the detuning δ between microwave and resonance frequency. Whereas the bare states are energetically degenerate for $\delta = 0$, the dressed states have an energy difference of Ω_0 and approach the bare states (dotted lines) for large detuning[27]. Shown here are the energies for a dressed state with n photons.

These are the so called dressed states¹ and they have to be used for a correct description of the two level system together with the radiation field. A comparison of the energies between dressed and bare states is shown in Fig.I.1.4. We are interested in large values of the detuning and find for $|\delta| \gg \Omega$

$$|+\rangle \approx \begin{cases} |e, n\rangle & \delta \ll 0 \\ |g, n+1\rangle & \delta \gg 0 \end{cases} \quad \text{and} \quad |-\rangle \approx \begin{cases} |g, n+1\rangle & \delta \ll 0 \\ |e, n\rangle & \delta \gg 0 \end{cases}. \quad (\text{I.1.42})$$

If the detuning δ is large compared to the resonant Rabi frequency Ω we can do a Taylor expansion of the eigenenergies Equ.I.1.39 and get

$$\epsilon_{\pm} \approx \pm \left(\frac{\delta}{2} + \frac{\Omega^2}{4\delta} \right) \quad \Rightarrow \quad \Delta E_{\pm} \approx \delta + \frac{\Omega^2}{2\delta}. \quad (\text{I.1.43})$$

From this we see that for large positive (blue) detuning the dressed state $|+\rangle$ is shifted energetically upwards with respect to the undressed bare ground state $|g, n+1\rangle$ by

$$\Delta E_{\text{shift}} = +\frac{\Omega}{4\delta} \quad (\text{I.1.44})$$

whilst the $|-\rangle$ is shifted downwards with respect to the undressed bare excited state $|e, n\rangle$ by the same amount and vice versa for negative detuning.

The two level system is useful to gain insight into the principle of microwave dressing. How-

¹There is a pair of dressed states in each n -photon manifold.

ever, the actual experimental situation is more complicated. We saw in the previous chapter that the two hyperfine manifolds form a system with $3 + 5$ substates if an external magnetic field is applied (Fig.I.1.1). This leads to a variety of possible transitions with different polarisations [31]. The geometry of our microwave antenna generates a mixture of all polarizations with different radiation powers. In principle, none of the bare states remains unchanged and we get a set of dressed states with altered energy levels. From Equ.I.1.42 and Equ.I.1.44 we see that for sufficiently large detuning the dressed states are basically the bare states. We use the transition $|1, 0\rangle \leftrightarrow |2, 0\rangle$ and shine in with blue detuned microwaves to get an upward shift in the energy of the $|1, 0\rangle$ state. For a given magnetic field strength the detuning has to be chosen in such a way that all other transitions are far detuned and the other produced dressed states do not differ from the original bare states.

As a side remark, the concept of dressed states can also be used to explain the principle of optical dipole traps. Equation I.1.44 shows that the energy of the dressed states depends not only on the detuning, but also on the resonant Rabi-frequency which itself depends on the intensity of the used radiation. As a direct consequence, the atoms will experience a so called dipole force if the intensity varies spatially.

A red detuned laser beam can be used to trap atoms in the $|+\rangle$ state while a blue detuned beam traps the atoms in the $|-\rangle$ state. This concept can also be extended to standing light waves, where for a red detuned laser the intensity maxima trap the $|+\rangle$ state, while the intensity nodes repel it, and vice versa for the $|-\rangle$ state.

I.1.4. Effective Hamiltonian for the SCC

So far we looked at the spinor dynamics in the $F=1$ hyperfine manifold of a BEC consisting of ^{87}Rb . The starting point of the discussion was the Hamiltonian Equ.I.1.1 which can be brought into a more convenient form by introducing the quantum numbers (η, M, N) , where η is the sum of the populations in the side modes, M the magnetisation and N the total atom number in the system. We discussed the effect of magnetic fields and found that the linear Zeeman effect cancels out while the quadratic Zeeman effect hinders the process of spin changing collisions due to violation of energy conservation.

By shining in suitable microwave radiation, the energy of the $|1, 0\rangle$ state can be shifted upwards by $\Delta E = +\frac{\Omega^2}{4\delta}$. For suitable Rabi-frequency Ω , which can be adjusted by the microwave power, and detuning δ the dressing compensates for the energy shift due to the quadratic Zeeman effect (Fig.I.1.5). The overall relative energy shift between the $|1, \pm 1\rangle$ and $|1, 0\rangle$ states is then given by

$$\Delta E = 71.89 \text{ Hz/G}^2 \cdot B^2 - \frac{\Omega^2}{4\delta} := q. \quad (\text{I.1.45})$$

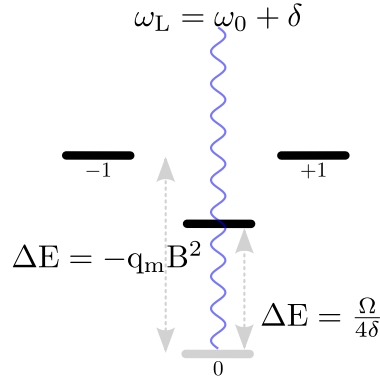


Fig. I.1.5. Relevant energy shifts for SCC in $F = 1$. The quadratic Zeeman effect suppresses the SCC since both atoms in the initial state ($|1, 0\rangle$) need to gain energy to reach the upper levels ($|1, -1\rangle$, $|1, +1\rangle$). The energy of the $|1, 0\rangle$ mode is shifted upwards by dressing with blue detuned microwaves using the transition $|2, 0\rangle \leftrightarrow |1, 0\rangle$. Control over the microwave radiation and its detuning allows to match the energy and thereby switch the spin changing collisions on and off. The $|2, 0\rangle$ state is not shown here.

This means that we are able to switch the spin changing collisions on and off by control of the microwave radiation and magnetic field. The energy shift due to the dressing adds a new term to the Hamiltonian Equ.I.1.32, which becomes

$$\hat{H}_N = \lambda \left[\hat{M}^2 + (2\hat{N} - 2\hat{\eta} - 1) \hat{\eta} + 2(\hat{\eta}_+ + \hat{\eta}_-) \right] + p\hat{M} + q\hat{\eta} \quad (\text{I.1.46})$$

with $p = p_{m_{F=1}} B = 702.37 \text{ MHz G}^{-1} B$.

We separate now the evolution due to the magnetisation M and the evolution due to the SCC and η and write

$$\hat{H}_N = \hat{H}_M + \hat{H}_{SCC}. \quad (\text{I.1.47})$$

(In the absence of loss) the time evolution due to the term $\hat{H}_M = \lambda\hat{M}^2 + p\hat{M}$ gives just an overall phase factor since the total magnetisation is conserved. Therefore the complete dynamics are determined by the effective Hamiltonian

$$\hat{H}_{\text{SCC}} = \lambda \left[(2\hat{N} - 2\hat{\eta} - 1) \hat{\eta} + 2 (\hat{\eta}_+ + \hat{\eta}_-) \right] + q\hat{\eta} \quad (\text{I.1.48})$$

$$\text{with } q = 71.89 \text{ Hz/G}^2 \text{B}^2 - \frac{\Omega^2}{4\delta}$$

$$\lambda = \frac{c_2}{2} \int d^3x |\Phi(\vec{x})|^4 \quad c_2 = \frac{4\pi\hbar^2}{M} \frac{a_2 - a_0}{3}$$

as long as M is constant¹. We will use this result frequently throughout the rest of this work. All numerical calculations presented in the further chapters were performed by implementing Equ.I.1.48 – or further simplifications of it – for a number state basis given by $|\eta, M, N\rangle$. Rearranging gives the Hamiltonian

$$\hat{H}_{\text{SCC}} = \lambda 2 (\hat{\eta}_+ + \hat{\eta}_-) + \lambda \left(2\hat{n}_0 - 1 + \frac{q}{\lambda} \right) \hat{\eta}. \quad (\text{I.1.49})$$

The first term describes the process which produces the atom pairs in the side modes. This process is analogue to the optical parametric down conversion [25, 37] in parametric amplifiers. We will use this in Ch.II to realise the non-linear interferometer.

The second term gives a dephasing, increasing in speed with η , which leads to a slowing down of the pair production. One can optimise the pair production using spin changing collisions by adjusting q in such a way that the dephasing term remains small as long as possible, that is

$$2n_0 - 1 + \frac{q}{\lambda} \approx 0. \quad (\text{I.1.50})$$

Since $\lambda < 0$ is fixed and n_0 decreases with ongoing SCC (depletion of the $|1, 0\rangle$ state) we need to choose

$$q_{\text{optimal}} \gtrsim 0 \quad (\text{I.1.51})$$

such that the term $2n_0 - 1 + \frac{q}{\lambda}$ sweeps over 0 with decreasing n_0 .

Figure I.1.6 shows how the relative population of the side modes evolves in time for different values of the ratio $\frac{q}{\lambda}$ (coloured lines) and for different initial conditions (**a** to **d**). The numerical simulations were performed with a total number of atoms $N = 500$ and $\lambda = -0.0015$ Hz.

The SCC-evolution with initially empty side modes ($\eta_0 = 0$, $M_0 = 0$) is shown in Fig.I.1.6a. As expected from Equ.I.1.50 the pair production in the side modes is enhanced for $\frac{q}{\lambda} < 0$. For

¹This condition is no longer satisfied if there are atom losses in the system or with Rabi-coupling between the different modes.

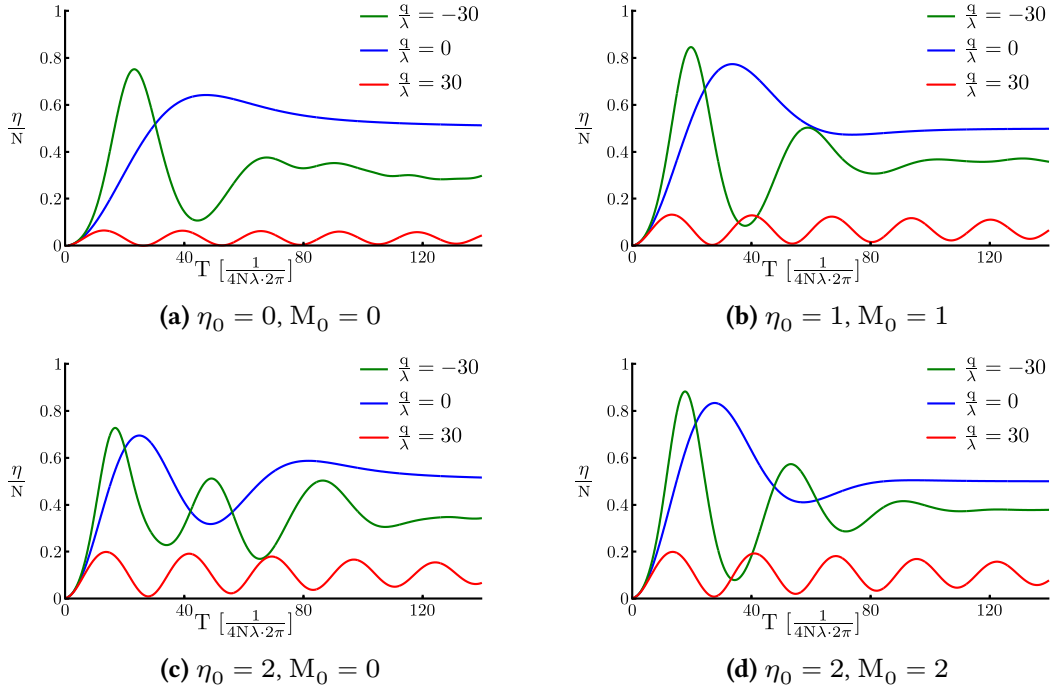


Fig. I.1.6. Theoretical evolution of the relative population of the side modes for various parameters. The numerical calculations were performed with a total of $N = 500$ atoms and $\lambda = -0.0015$ Hz. **a)** SCC-evolution without initial seed of the side modes $\eta_0 = 0, M_0 = 0$. **b)** asymmetric initial seed with $\eta_0 = 1, M_0 = 1$. **c)** symmetric initial seed with $\eta_0 = 2, M_0 = 0$. **d)** asymmetric initial seed with $\eta_0 = 2, M_0 = 2$. The time evolution for $\frac{a}{\lambda} = -30$ (green) has a larger maximal occupation than those for $\frac{a}{\lambda} = +30$ (red) and $\frac{a}{\lambda} = 0$ (blue). With initially seeded side modes the spin changing collisions are faster. The shape of the curves depends strongly on the initial distribution and number of atoms in the side modes (**c**, **d**). All graphs show the non-linear growth of the side mode population for suitable values of $\frac{a}{\lambda}$.

$\frac{a}{\lambda} = 0$ the evolution shows a plateau after the first peak, while $\frac{a}{\lambda} > 0$ gives oscillations with a small amplitude.

In the case of initially seeded side modes (**b**, **c**, **d**) the SCC occur faster and the shape of the evolution changes. Asymmetric seed leads to a general increase in the maxima for all three values of $\frac{a}{\lambda}$ (Fig.I.1.6b with $\eta_0 = 1, M_0 = 1$ and Fig.I.1.6b with $\eta_0 = 2, M_0 = 2$). Symmetric seed increases the maximum for $\frac{a}{\lambda} = 0$ and $\frac{a}{\lambda} = +30$ but lowers it for $\frac{a}{\lambda} = -30$.

The shapes of the curves in the asymmetric cases are more similar to the unseeded ones than the curves with symmetric initial seed. A qualitative explanation could be that for $\eta_0 \neq 0, M_0 = 0$ the atoms in $|1, +1\rangle$ and $|1, -1\rangle$ can initiate the scattering back into $|1, 0\rangle$ and therefore the first maximum has to be decreased. This can not happen if only one of the side modes is populated at the beginning since the total magnetisation has to be conserved.

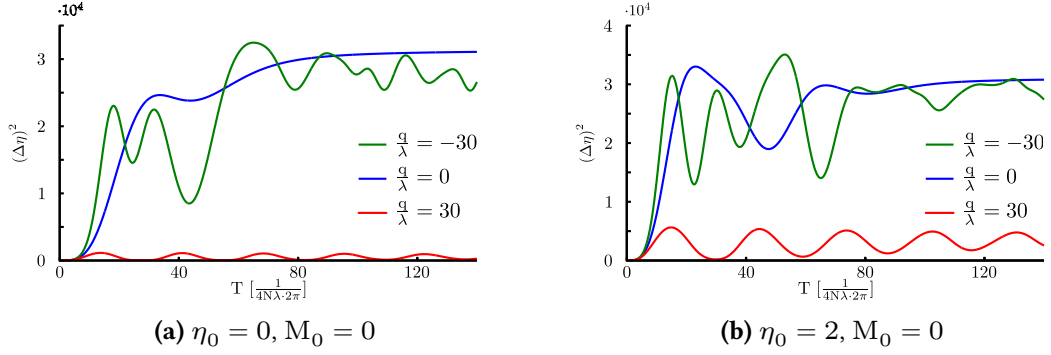


Fig. I.1.7. Theoretical evolution of variance of side mode population during SCC for the same initial conditions as in Fig.I.1.6a ($\eta_0 = 0, M_0 = 0$) and Fig.I.1.6c ($\eta_0 = 2, M_0 = 0$). For $\frac{g}{\lambda} = 0$ (blue) and $\frac{g}{\lambda} = +30$ (red) the variance shows a similar behaviour as the mean value of η indicating that $(\Delta\eta)^2$ increases with increasing η . In the case of $\frac{g}{\lambda} = -30$ (green) the variance also increases initially but shows a local minimum at the position of the first maximum of η . Hence, the fluctuations in the side mode population decrease again when η approaches the local maximum.

We want to emphasize that the shown graphs are calculated for initially 0, 1 and 2 atoms in the side modes with a total number of $N = 500$ atoms and we see that already a small seed has a huge effect on the SCC-evolution. However, all graphs show the non-linear growth of the side mode population for suitable values of $\frac{g}{\lambda}$.

As mentioned before the magnetisation $M = n_- - n_+$ is conserved and therefore the variance of the side mode population difference vanishes. In contrast to this shows the sum of the side mode populations $\eta = n_- + n_+$ huge fluctuations which evolve in time. The variance $(\Delta\eta)^2$ for the initial cases $\eta_0 = 0, M_0 = 0$ and $\eta_0 = 2, M_0 = 0$ is plotted in Fig.I.1.7. The corresponding evolution of η are shown in Fig.I.1.6a and Fig.I.1.6c. Note that in the case of $\frac{g}{\lambda} = -30$ (green) the variance $(\Delta\eta)^2$ initially increases with increasing η but has a local minimum at the first maximum of η . Hence, the fluctuations in the side mode population decrease again when η approaches the local maximum.

I.2. Experiment

Our experiments are performed in the ground state hyperfine manifold $5^2S_{1/2}$ of ^{87}Rb with total spin $F = 1$ and $F = 2$. Before the experimental sequence for spin dynamics, we prepare an array of Bose-Einstein condensates roughly explained below. For more details see [38, 39].

We use the D_2 line ($5^2S_{1/2} \Rightarrow 5^2P_{1/2}$) at ≈ 780 nm and its cycling transition [33] to initially capture atoms in a three dimensional magneto-optical trap (MOT). The atoms are then cooled further via evaporative cooling in a magnetic time-orbiting potential (TOP) trap [40] close to the critical temperature for Bose-Einstein condensation. We pump all atoms in the $|1, -1\rangle$ state, which is a low-field seeker and can be magnetically trapped. The atomic cloud is transferred into a far-detuned optical dipole trap, where Bose-Einstein condensation is reached through further evaporative cooling. Finally, a 1D lattice is ramped up. The lattice is formed by two laser beams at ≈ 820 nm crossed under an angle of $\approx 9^\circ$. The radial confinement is ensured by a dipole trap at ≈ 1030 nm in direction of the standing wave lattice.

This procedure yields approximately 30 independent ^{87}Rb -BECs in the $|1, -1\rangle$ state separated by $\approx 5.5 \mu\text{m}$. The preparation leads to atom numbers of about 500 in the central wells which are decreasing to the edges of the lattice. A homogeneous magnetic offset field ensures that the magnetic substates are not degenerate and the atoms remain in $|1, -1\rangle$.

The actual experimental sequences for spinor experiments, which are employing resonant microwave or radio frequency radiation, will be explained in the corresponding section. Each measurement has to be repeated several times in order to obtain enough statistics. The data from the

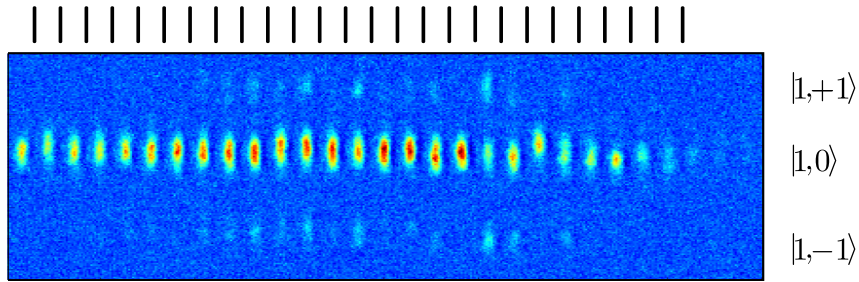


Fig. I.2.1. Example of an experimental image, showing the wells in the 1D lattice with a spatial distance of about $5.5 \mu\text{m}$. Each lattice site contains an independent BEC. The separation of the atoms in the $|1, +1\rangle$ (top), $|1, 0\rangle$ (middle) and $|1, -1\rangle$ (bottom) states is due to the final Stern-Gerlach-pulse. The image was taken via absorption imaging after an SCC-evolution in $F = 1$ for 260 ms. The total atom number in each of the central wells is approximately 500. In a specific well the same number of atoms in the states $|1, +1\rangle$ and $|1, -1\rangle$ is found revealing the pair production and conservation of magnetisation during the SCC. The side mode population fluctuates from well to well confirming the theoretical expectation of a large variance in η . The black lines represent the lattice.

different lattice sites can in principle be averaged since they are independent from each other.

However, the gradient of the microwave power over the spatial extent of the lattice and the varying atom number lead to different experimental conditions in the single wells. As mentioned before the value of λ depends on the total atom number N . This has a direct effect on the speed of the SCC. The microwave power influences the Rabi-frequency affecting the energy shift (Equ.I.1.45). This has to be taken into account in the analysis of the data by proper post selection on a subset of lattice sites and atom number.

After the actual experimental sequence a magnetic Stern-Gerlach-pulse separates the magnetic substates spatially for detection which is implemented via resonant absorption imaging. For further details on the detection scheme and the extraction of the atom numbers from the images see [41]. An example of an experimental image can be seen in Fig.I.2.1.

I.2.1. Atom number distribution in the course of SCC

In order to perform the spin changing collision experiments, the atoms are at first transferred from the $|1, -1\rangle$ to the $|1, 0\rangle$ state with a resonant radio frequency π -pulse. To ensure an efficient transfer to the state $|1, 0\rangle$, this is done at a magnetic field of $B = 9\text{G}$ where the quadratic Zeeman effect leads to a detuning of the transition $|1, 0\rangle \leftrightarrow |1, +1\rangle$. Afterwards the magnetic field is ramped down to the final value used in the experiment and a Stern-Gerlach pulse perpendicular to the lattice axis is applied to remove the remaining atoms in the magnetic sensitive substates $|1, -1\rangle$ and $|1, +1\rangle$.

As discussed in Sec.I.1.4, the finite value of the magnetic field suppresses the SCC due to the quadratic Zeeman effect. For obtaining spin-changing collisions, we switch on the microwave radiation for a certain time as described before and subsequently detect the atom numbers in the three substates.

The figures I.2.2 **a) - d)** show the experimental probability distributions of the atom numbers in the side modes in the course of an SCC-evolution for four different hold times. Figure I.2.2e shows the complete time evolution of the experimental probability distribution. The red line represents the mean atom number in the side modes.

At $t = 0$ ms the side modes are empty and the distribution has a peak at $\eta = n_+ + n_- = 0$. The broadening and the detection of negative atom numbers is due to finite detection noise of our absorption imaging. The mean population of the side modes grows with increasing evolution time until $t \approx 400$ ms. Also, the probability distribution changes significantly. It resembles the one of a thermal state [17] with Gaussian detection noise for small evolution times (**b**) and broadens at the maximum (**c**). Further increase of the evolution time leads to a back oscillation

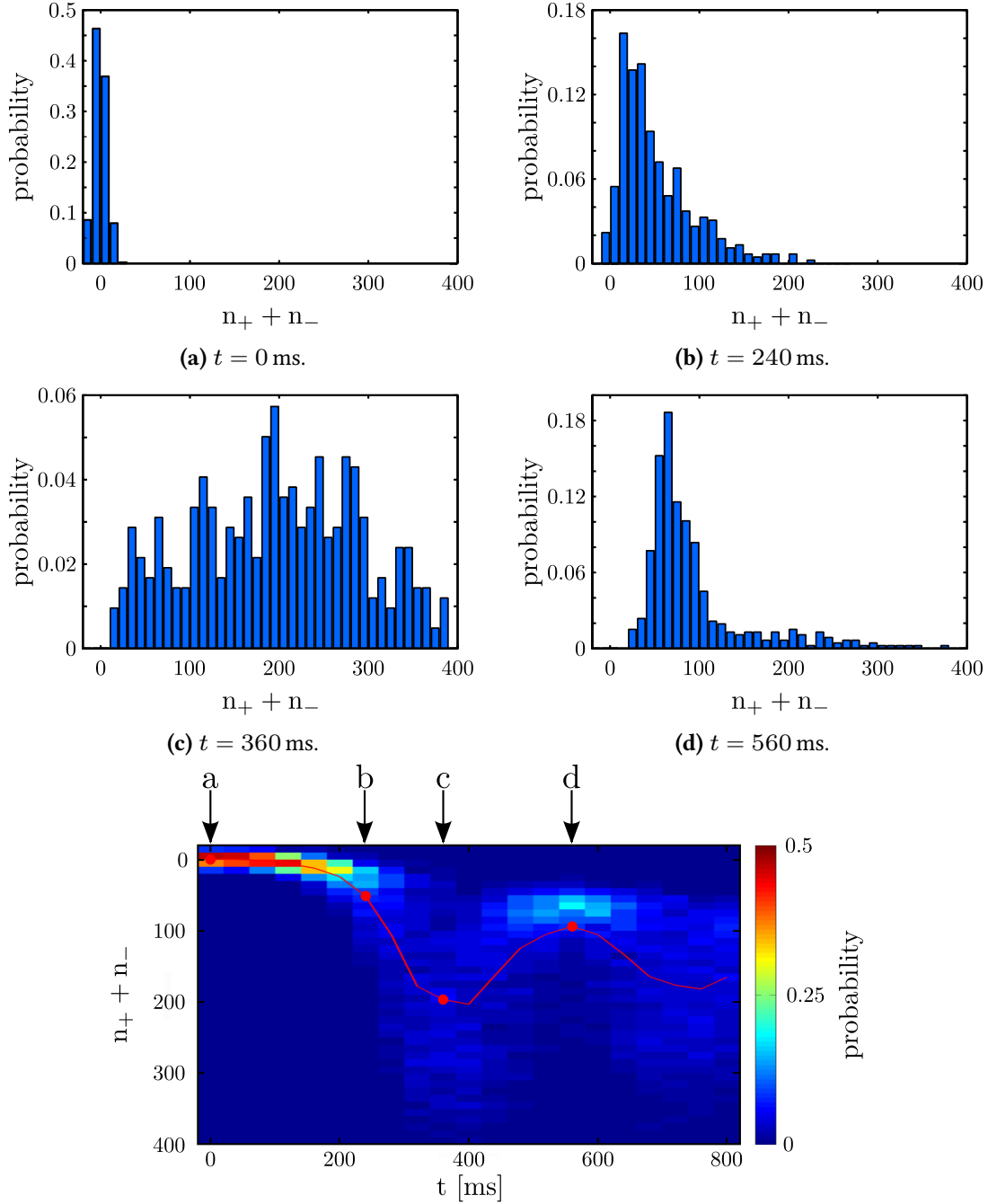


Fig. I.2.2. Atom number distribution in side modes during SCC-evolution. **a)** The side modes are initially empty and the distribution has a peak at $\eta = n_+ + n_- = 0$ which is broadened due to detection noise. **b), c)** the probability “flows” to larger η and the distribution broadens leading to fluctuations of the side mode population. **d)** after the first maximum in the evolution the SCC are partially reversed and a minimum in η occurs again. The probability distribution narrows again. **e)** Histograms for all evolution times measured in this experimental run. The colour codes the experimental probability and the red line shows the expectation value of η . One observes oscillating behaviour in the shape of the distribution leading to increase and decrease of the variance $(\Delta\eta)^2$.

of the mean population and the probability distribution narrows again.

The oscillations of η are in qualitative agreement with the theoretical expectations (Fig.I.1.6). Since the total atom number in the experiment was about $N_{\text{tot}} \approx 450$ the first maximum shows a transfer to the side modes of less than 50% which is inconsistent with the theoretical curves shown. This might be caused by the averaging over different wells and total atom numbers. Nevertheless this has to be done in order to have enough statistics for the histograms. Other reasons of the discrepancy may be the atom loss during the evolution or technical fluctuations, leading to dephasing.

The measurements were performed at $B = 0.91\text{G}$. The Rabi frequency of the microwave transition used for the dressing was $\Omega \approx 5.5\text{kHz}$ and the microwave detuning $\delta \approx 197\text{kHz}$. Varying the SCC-evolution time from $t = 0 \dots 800\text{ms}$ in steps of $\Delta t = 40\text{ms}$ and post selecting the eight central wells gave a about 460 data points at each evolution time.

I.2.2. Conservation of magnetisation during spin changing collisions

The spin changing collisions produce correlated atom pairs. For this pairwise production, the same number of atoms is expected in both states. The consequence is that the magnetisation $M = n_- - n_+$ is conserved and its variance vanishes.

The red data points in Fig.I.2.3 show the variance of the magnetisation versus the mean population produced in the side modes ($\langle \eta \rangle = \langle n_+ + n_- \rangle$) for an experimental time evolution of spin changing collisions similar to that discussed in the previous section. The red line is a linear fit with a slope of 0.1 ± 0.1 and an intersection with the y-axis at 63 ± 7 . This offset is due to detection noise. The constant value of the variance reveals its strong squeezing despite the broadening in the distribution of the side mode population (Fig.I.2.2). This indicates that the atoms in the side modes are produced in pairs.

Up to the first maximum a larger value of $\langle \eta \rangle$ corresponds to a longer evolution time. However, with increasing evolution time atom loss corrupts the conservation of magnetisation and therefore the variance increases. To account for this, the evolution time was post selected to be below 300 ms in the data shown.

The blue points show the same analysis for a coherent state. In this measurement the atoms were initially kept in the $|1, -1\rangle$ state and no Stern-Gerlach cleaning pulse was applied. A first resonant microwave $\frac{\pi}{2}$ -pulse between $|1, -1\rangle \leftrightarrow |2, 0\rangle$ and a subsequent resonant π -pulse between $|2, 0\rangle \leftrightarrow |1, +1\rangle$ produced a coherent state in the two level system formed by the states $|1, -1\rangle$ and $|1, +1\rangle$. A theoretical calculation for this coherent state gives

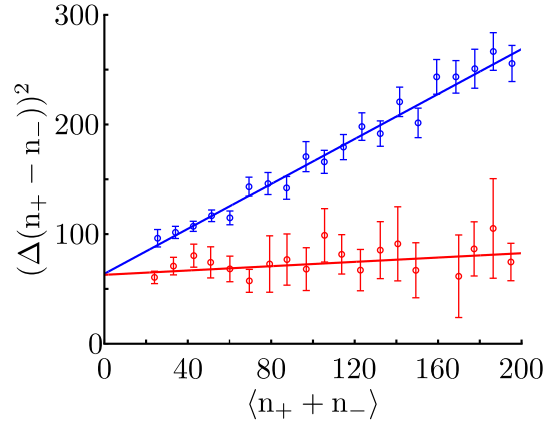


Fig. I.2.3. Suppression of relative fluctuations with spin-changing collisions. The red data points show the variance of the side mode population difference versus the mean of its sum for states produced by spin-changing collisions. The fitted line has a slope of 0.1 ± 0.1 , revealing the strong squeezing in the variance of the magnetisation despite the observed broadening in the distribution of the side mode population (Fig.I.2.2). The offset (63 ± 7) is mainly due to photon shot noise in our detection system.

The blue data points show the same for a coherent state in the two level system formed by $|1, -1\rangle$ and $|1, +1\rangle$ produced by linear coupling. The fitted line has a slope of 1.1 ± 0.1 , which is in good agreement with the expected theoretical value of 1. The red data points show the same for spin changing collisions.

$$(\Delta(n_- - n_+))^2 = \langle n_- + n_+ \rangle = \langle \eta \rangle. \quad (\text{I.2.1})$$

The linear fit to the experimental data has a slope of 1.1 ± 0.1 which is in good agreement with the theory. Its offset of 64 ± 6 coincides with the one of the SCC measurement as expected.

In both cases the errors of the variances were estimated by resampling the data sets (Jackknife method, [42]). For this resampling analysis the data sets for each atom number were divided into sub ensembles. In each sub ensemble another data point was omitted yielding n samples each with $n - 1$ data points. Let $(\Delta M_{S_i})^2$ be the variance of the magnetisation for the i^{th} sample S_i . The variance of $(\Delta M)^2$ for the entire data set was estimated with the formula

$$\text{var}((\Delta M)^2) = \frac{n-1}{n} \sum_{i=1}^n \left((\Delta M_{S_i})^2 - (\Delta M)^2 \right)^2 \quad (\text{I.2.2})$$

The errors were then calculated via

$$\Delta((\Delta M)^2) = \sqrt{\frac{\text{var}((\Delta M)^2)}{n-1}} \quad (\text{I.2.3})$$

This procedure was used in the entire thesis to calculate the errors of the variances.

I.2.3. SCC-evolution in F=2

The SCC-evolution in the $F = 2$ hyperfine manifold is comparable to the one in $F = 1$, but additional scattering channels have to be considered in the theoretical treatment and the scattering lengths are different. A detailed discussion of the theory can be found in [28]. To perform the experiment in $F = 2$, the atoms condensed in $|1, -1\rangle$ were transferred via a resonant MW- π -pulse to the state $|2, 0\rangle$. The same microwave transition as for the SCC in $F = 1$ was used for the dressing.

The following measurement parameters were used:

- magnetic field: $B = 1.45\text{G}$
- Rabi-frequency: $\Omega \approx 5.4\text{ kHz}$
- detuning δ : $32.5\text{ kHz} \dots 40.6\text{ kHz}$ in steps of $\Delta\delta = 0.3\text{ kHz}$
- SCC-evolution time t : $1\text{ ms} \dots 116\text{ ms}$ in steps of $\Delta t = 5\text{ ms}$

The total atom number was post selected in the range $N_{\text{tot}} = 200 \dots 600$. Figure I.2.4a shows the mean atom number in the side modes depending on the microwave detuning δ and the evolution time t . Comparing the time scales of the SCC-evolution in $F = 1$ (Fig.I.2.2e) and $F = 2$ directly reveals the greater speed of the latter one, due to the larger coupling constant.

We observe three different detuning regions. For $\delta \lesssim 33\text{ kHz}$ the side modes remain almost empty throughout the whole evolution. In the range of $33\text{ kHz} \lesssim \delta \lesssim 34\text{ kHz}$ the side mode population reaches a maximum and levels out at a nearly constant value. For greater detuning δ the side mode population performs damped oscillations. Increasing δ leads to a decrease of the maxima observed.

The three cases correspond to the red ($\frac{q}{\lambda} > 0$), blue ($\frac{q}{\lambda} \approx 0$) and green ($\frac{q}{\lambda} < 0$) curves in Fig.I.1.6, respectively.

The outcome of a numerical simulation with the same magnetic field and an atom number of $N = 400$ is shown in Fig.I.2.4b for the same detuning range. The parameters λ and Ω are adjusted to fit to the experimental data. This results in $\lambda \approx 40\text{ mHz}$ which is comparable to the value found in [31]. However, the obtained theoretical $\Omega \approx 4.45\text{ kHz}$ does not agree with independent

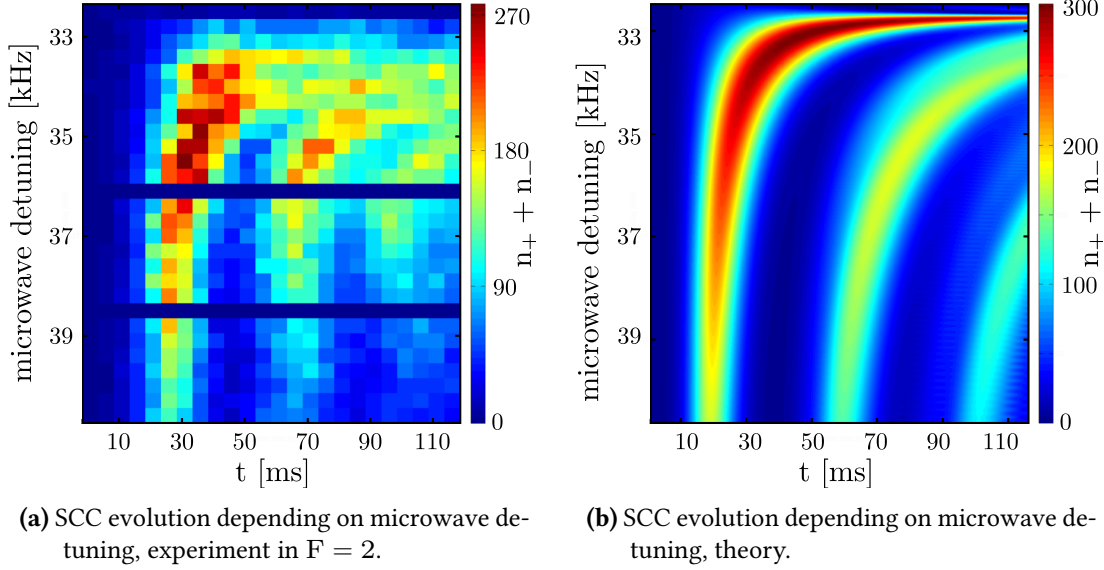


Fig. I.2.4. SCC evolution depending on microwave detuning in $F = 2$. The colour codes the total population in the side modes. **a)** Shown is the dependence of the SCC-evolution on the microwave detuning δ . For each detuning an SCC-evolution was measured with time steps of $\Delta t = 5$ ms. The two blue horizontal lines are due to a programming mistake in the measurement script. **b)** For the theoretical picture a total atom number of $N = \bar{N}_{\text{exp}} = 400$ and the experimental values of the magnetic field, evolution time and detuning δ were used. The values for the Rabi frequency Ω (≈ 4.45 kHz) and λ (≈ 40 mHz) were adjusted to be consistent with the experimental result.

measurements on Ω by resonant Rabi flopping. The different values of Ω are probably due to dressing of the $|2, -1\rangle$ and $|2, +1\rangle$ states instead of only the $|2, 0\rangle$ state as assumed in the theory¹. The discrepancy between experiment (Fig.I.2.4a) and theory (Fig.I.2.4b) is due to similar reasons as in the $F = 1$ case such as atom loss and dephasing (Sec.I.2.1). Due to dipole relaxation the atom loss is larger in $F = 2$ and has therefore a stronger effect. The measured $1/e$ lifetime of the total atom number in $F = 2$ (≈ 200 ms) is significantly shorter than the one in $F = 1$ (≈ 15 s).

As previously mentioned, λ depends on the total atom number which changes in time. Therefore the speed of the SCC changes during the progress. This is not taken into account in the theory.

¹See the discussion about the different polarisations of the microwave radiation in Sec.I.1.3.

II. SU(1,1)-interferometer

Interferometry is the basis for precision measurements of all kind such as gravimetry, detection of gravitational waves, atomic clocks and precise rotation measurements [1, 43, 3, 4]. The underlying principle is to use the phenomena of constructive and destructive interference of overlapping waves.

A well known example is the Mach-Zehnder interferometer which is schematically shown in Fig.II.0.1. In an optical interferometer of this kind an incoming light beam is split into two arms by a first beam splitter BS_1 . After following through the different paths, both light beams are overlapped again by a second beam splitter BS_2 and the outgoing light beams are analysed. The signals after BS_2 show a sinusoidal dependence on the phase difference ϕ accumulated by the light beams in the two different arms inside the interferometer.

The same principle is used in atom optics to realise interferometers. The counterpart to the optical beam splitter is realised by a pulse of resonant electromagnetic radiation (Rabi-coupling) acting on an atomic two level system. This leads to the redistribution of the atom number population between the levels. The energy difference causes an evolution of the relative phase between the two states analogue to the optical paths mentioned above. A second pulse corresponds to the second beam splitter. The final atom number distribution between the two levels depends on the relative phase. Due to the analogue concept we will further refer to the pulses as beam splitters.

The phase sensitivity $\Delta\phi$ is the parameter which characterises the quality of an interferometer. For classical interferometers the best attainable limit of the phase sensitivity is called the standard quantum limit (SQL)[9, 8] and reads

$$\Delta\phi_{\text{SQL}} = \frac{1}{\sqrt{N}} \quad (\text{II.0.1})$$

where N is the number of particles inside the interferometer. By using quantum resources one can surpass the SQL and approach the Heisenberg limit

$$\Delta\phi_{\text{HL}} = \frac{1}{N}. \quad (\text{II.0.2})$$

One way of doing this is by feeding entangled quantum states into the input ports of the first beam splitter [7, 9, 8, 44, 43].

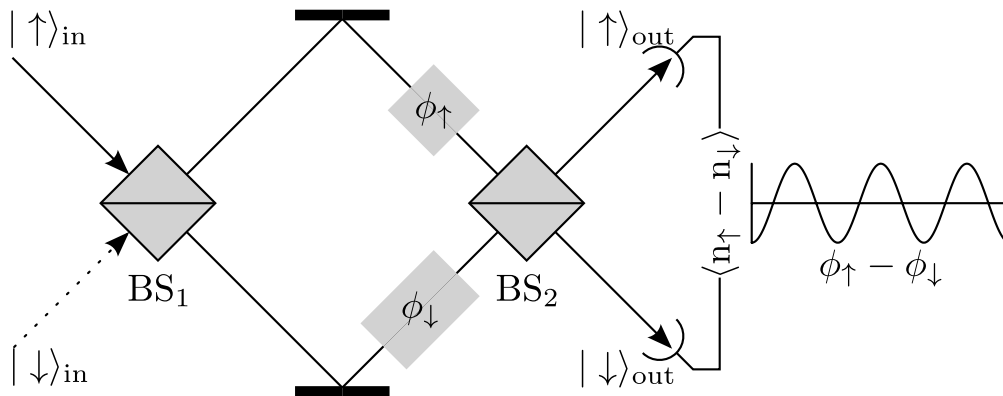


Fig. II.0.1. Mach-Zehnder interferometer. In the standard scheme one incoming beam ($|\uparrow\rangle_{\text{in}}$) passes a first beam splitter BS_1 . After some phase evolution ($\phi_\uparrow, \phi_\downarrow$) the two paths are recombined by a second beam splitter BS_2 . The difference between the two outgoing signals shows a sinusoidal dependence on the phase difference. In atomic optics the beam splitters are realised by resonant Rabi coupling between the modes of an atomic two level system. The well known Ramsey sequence [45] is realised in such a system.

In the following we will have a look at a different interferometric concept with three instead of two atomic states. The former passive beam splitters will be replaced by parametric amplifiers.

In optics this is done with non linear crystals and has been realised recently by [11]. By shining a strong laser beam of frequency f_{Laser} into such a non linear crystal one can produce two beams of entangled photon pairs with half the frequency of the laser $f_{\text{photon}} = f_{\text{laser}}/2$ by a process called parametric down conversion. The strong incoming laser beam is named the pump mode, the two produced beams are the signal and idler mode. For this process to happen one has to satisfy the phase matching condition between pump mode and crystal.

The process of spin changing collisions discussed in Ch.I is the atomic equivalent to the optical parametric down conversion and we can use the SCC to build such an interferometer in atomic optics.

In this chapter we will give a short revision of the theoretical description of the Mach Zehnder interferometer in the framework of the rotation group $\text{SU}(2)$. Afterwards, the introduction of the $\text{SU}(1,1)$ -group allows us to follow a quite similar approach to the new kind of interferometer which uses the process of parametric down conversion. The insight gained so far will make it possible to discuss experimental results in the *non depletion* regime. We then extend the theory to the *depleted* regime and introduce the concept of the *Fisher information* F_I for analysing the

phase sensitivity $\Delta\phi$.

II.1. Mach-Zehnder interferometer in $SU(2)$ -group representation

Let us begin this chapter with a short look at the underlying theory of a Mach-Zehnder interferometer. Although this is widely known, we will shortly repeat the main aspects since we will use a quite similar approach to the interferometer with the SCC later on. A more detailed treatment can be found in [9, 46].

We consider a Mach-Zehnder interferometer as sketched in Fig.II.0.1. The two incoming ports $|\uparrow\rangle$ and $|\downarrow\rangle$ form a two level system for each particle entering the interferometer. A general state of this system can be characterised by a complex number $\alpha_{\theta,\phi}$ and written in the form

$$|\alpha_{\theta,\phi}\rangle = \cos\frac{\theta}{2}|\uparrow\rangle + e^{i\phi}\sin\frac{\theta}{2}|\downarrow\rangle. \quad (\text{II.1.1})$$

Here $\cos^2\frac{\theta}{2}$ and $\sin^2\frac{\theta}{2}$ are the probabilities to find one particle in the $|\uparrow\rangle$ respectively $|\downarrow\rangle$ state. That is, if in total $N = n_{\uparrow} + n_{\downarrow}$ particles enter the interferometer we will find a mean difference of the population between the two levels of $n_{\uparrow} - n_{\downarrow} = N \cos\theta$ before the first beam splitter. It has to be mentioned that this is only true as long as the single particles are completely uncorrelated and the N -particle state can be written as a product of the N single-particle states Equ.II.1.1. The whole N -particle system can be expressed on the surface of a so called generalised Bloch sphere[47] with radius $N/2$, where θ is the polar and ϕ the azimuthal angle (Fig.II.1.1a).

The states $|\alpha_{\theta,\phi}\rangle$ are called coherent spin states (CSS). They form a basis but are not orthogonal to each other [48].

We now connect the action of the two beam splitters and the phase evolution in between with the $SU(2)$ -group of rotations. The $SU(2)$ -group is defined by its commutation relations

$$[\hat{J}_x, \hat{J}_y] = i\hat{J}_z, \quad [\hat{J}_y, \hat{J}_z] = i\hat{J}_x, \quad [\hat{J}_z, \hat{J}_x] = i\hat{J}_y \quad (\text{II.1.2})$$

which are fulfilled by the angular momentum operators

$$\hat{J}_x = \frac{1}{2}(\hat{a}_{\uparrow}^{\dagger}\hat{a}_{\downarrow} + \hat{a}_{\downarrow}^{\dagger}\hat{a}_{\uparrow}), \quad \hat{J}_y = -\frac{i}{2}(\hat{a}_{\uparrow}^{\dagger}\hat{a}_{\downarrow} - \hat{a}_{\downarrow}^{\dagger}\hat{a}_{\uparrow}), \quad \hat{J}_z = \frac{1}{2}(\hat{a}_{\uparrow}^{\dagger}\hat{a}_{\uparrow} - \hat{a}_{\downarrow}^{\dagger}\hat{a}_{\downarrow}) \quad (\text{II.1.3})$$

with the creation and annihilation operators for the $|\uparrow\rangle$ and $|\downarrow\rangle$ states $\hat{a}_{\uparrow}, \hat{a}_{\downarrow}, \hat{a}_{\uparrow}^{\dagger}$ and $\hat{a}_{\downarrow}^{\dagger}$ satisfying

the bosonic commutation relations. The operator

$$\hat{N} = \hat{a}_\uparrow^\dagger \hat{a}_\uparrow + \hat{a}_\downarrow^\dagger \hat{a}_\downarrow \quad (\text{II.1.4})$$

is the sum of the particles in the $|\uparrow\rangle$ and $|\downarrow\rangle$ state which commutes with all operators in Equ.II.1.3 and therefore it is constant in time for Hamiltonians build out of such angular momentum operators.

Lastly we introduce the raising and lowering operator

$$\hat{J}_+ = \hat{J}_x + i\hat{J}_y = \hat{a}_\uparrow^\dagger \hat{a}_\downarrow, \quad \hat{J}_- = \hat{J}_x - i\hat{J}_y = \hat{a}_\downarrow^\dagger \hat{a}_\uparrow \quad (\text{II.1.5})$$

which can be used to construct any coherent spin state with $\alpha = -\frac{\theta}{2}e^{-i\phi}$ via the displacement operator [27, 49]

$$|\alpha_{\theta,\phi}\rangle = \underbrace{e^{\alpha\hat{J}_+ - \alpha^*\hat{J}_-}}_{\text{displacement operator}} |\uparrow\rangle. \quad (\text{II.1.6})$$

As mentioned before the state $|\alpha_{\theta,\phi}\rangle$ can be represented on a generalised Bloch sphere. The coordinates of its expectation value are calculated with the newly defined operators and read

$$\vec{\alpha}_{\theta,\phi} = \begin{pmatrix} \langle\alpha|\hat{J}_x|\alpha\rangle \\ \langle\alpha|\hat{J}_y|\alpha\rangle \\ \langle\alpha|\hat{J}_z|\alpha\rangle \end{pmatrix} = \frac{N}{2} \begin{pmatrix} \sin\theta\cos\phi \\ \sin\theta\sin\phi \\ \cos\theta \end{pmatrix}. \quad (\text{II.1.7})$$

Note that $2\langle\hat{J}_z\rangle$ is the population difference previously mentioned. This is the experimentally accessible quantity since it can be attained from counting the number of particles in the two modes.

Lets consider a general state described by the density matrix $\hat{\rho}$. The Husimi or Q distribution measures the overlap of this state with a coherent state $|\alpha_{\theta,\phi}\rangle$ [27]. It is calculated by

$$Q(\alpha_{\theta,\phi}) = \langle\alpha_{\theta,\phi}|\hat{\rho}|\alpha_{\theta,\phi}\rangle \quad (\text{II.1.8})$$

and can be used to visualise the probability contributions of all coherent states to the particular state described by ρ . Figure II.1.1 shows the distributions of a CSS and a number state plotted on generalised Bloch sphere. Although the width of the number state in z-direction is zero, we see it with a finite width. The reason is that $Q(\alpha_{\theta,\phi}) \geq 0$ and does not reveal any kind of phase factor in front of the contributing CSS.

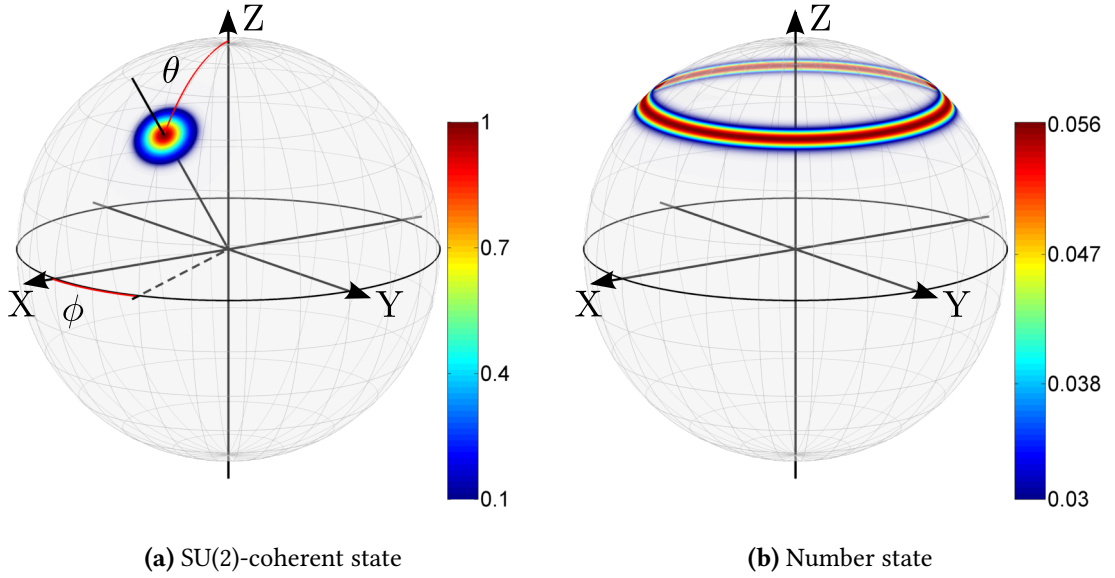


Fig. II.1.1. **a)** $SU(2)$ -coherent state and **b)** number state for $N = 400$ atoms in Husimi representation on a generalised Bloch sphere. The colour shows the overlap with the coherent states at the respective positions on the Bloch sphere. The coherent state $|\alpha_{\theta, \phi}\rangle$ has a narrow distribution in the relative phase peaked at the coordinates (θ, ϕ) . In contrast to this, the phase of the number state is completely undetermined. However, one has to keep in mind that a number state has no fluctuations in z -direction, which is masked in the Husimi representation due to the convolution with coherent states. Increasing N leads to a narrowing of the distributions [50].

We are interested in how the expectation values $\langle \hat{J}_{\kappa} \rangle$, with $\kappa = x, y, z$, change under the transformation

$$\begin{pmatrix} \hat{J}_x \\ \hat{J}_y \\ \hat{J}_z \end{pmatrix}_{\text{out}} = \hat{U}_{\kappa}^{\dagger} \begin{pmatrix} \hat{J}_x \\ \hat{J}_y \\ \hat{J}_z \end{pmatrix}_{\text{in}} \hat{U}_{\kappa} \quad \text{with } \hat{U}_{\kappa} = e^{-i\hat{J}_{\kappa}\gamma}. \quad (\text{II.1.9})$$

To see this we look at first at the transformations of the \hat{a}_{\uparrow} and \hat{a}_{\downarrow} which can be expressed in matrix notation in the following way

$$\begin{pmatrix} \hat{a}_{\uparrow} \\ \hat{a}_{\downarrow} \end{pmatrix}_{\text{out}} = S_{\kappa} \begin{pmatrix} \hat{a}_{\uparrow} \\ \hat{a}_{\downarrow} \end{pmatrix}_{\text{in}}. \quad (\text{II.1.10})$$

To obtain the matrices S_{κ} one calculates $\hat{a}_{\text{out}} = \hat{U}_{\kappa}^{\dagger} \hat{a}_{\text{in}} \hat{U}_{\kappa}$ and compares the result to $(\hat{a}_{\uparrow}, \hat{a}_{\downarrow})_{\text{in}}$. The matrices read

$$\begin{aligned}
 S_x(\gamma) &= \begin{pmatrix} \cos(\frac{\gamma}{2}) & -i \sin(\frac{\gamma}{2}) \\ -i \sin(\frac{\gamma}{2}) & \cos(\frac{\gamma}{2}) \end{pmatrix} & S_y(\gamma) &= \begin{pmatrix} \cos(\frac{\gamma}{2}) & \sin(\frac{\gamma}{2}) \\ \sin(\frac{\gamma}{2}) & \cos(\frac{\gamma}{2}) \end{pmatrix} \\
 S_z(\gamma) &= \begin{pmatrix} e^{-i\frac{\gamma}{2}} & 0 \\ 0 & e^{i\frac{\gamma}{2}} \end{pmatrix}.
 \end{aligned} \tag{II.1.11}$$

With these one can calculate the transformed $\hat{J}_{\kappa, \text{out}}$ (Equ.II.1.9) and their expectation values. As an example we look at the effect of \hat{U}_x and get

$$\begin{aligned}
 \begin{pmatrix} \langle \hat{J}_x \rangle \\ \langle \hat{J}_y \rangle \\ \langle \hat{J}_z \rangle \end{pmatrix}_{\text{out}} &= \begin{pmatrix} 1 & 0 & 0 \\ 0 & \cos(\gamma) & -\sin(\gamma) \\ 0 & \sin(\gamma) & \cos(\gamma) \end{pmatrix} \begin{pmatrix} \langle \hat{J}_x \rangle \\ \langle \hat{J}_y \rangle \\ \langle \hat{J}_z \rangle \end{pmatrix}_{\text{in}} \\
 \Leftrightarrow \begin{pmatrix} \hat{J}_x \\ \hat{J}_y \\ \hat{J}_z \end{pmatrix}_{\text{out}} &= e^{i\hat{J}_x \gamma} \begin{pmatrix} \hat{J}_x \\ \hat{J}_y \\ \hat{J}_z \end{pmatrix}_{\text{in}} e^{-i\hat{J}_x \gamma}
 \end{aligned} \tag{II.1.12}$$

which is just a rotation about the axis defined by $\langle \hat{J}_x \rangle$. Analogous expressions are found for the other two operators and we see that the \hat{J}_{κ} rotate the state around the corresponding κ -axis in the Bloch sphere picture.

How this is connected to the interferometer will be discussed in the following. A beam splitter redistributes the particles between the two levels. This can be written in the form

$$\begin{aligned}
 \hat{H}_{\text{BS}} &= \frac{\Omega}{2} (e^{-i\varphi} \hat{a}_{\uparrow}^{\dagger} \hat{a}_{\downarrow} + e^{i\varphi} \hat{a}_{\downarrow}^{\dagger} \hat{a}_{\uparrow}) = \frac{\Omega}{2} (e^{-i\varphi} \hat{J}_+ + e^{i\varphi} \hat{J}_-) \\
 &= \Omega (\cos(\varphi) \hat{J}_x + \sin(\varphi) \hat{J}_y)
 \end{aligned} \tag{II.1.13}$$

and the time evolution operator for the beam splitter is $\hat{U} = e^{-i\hat{H}_{\text{BS}} t}$. The operators \hat{a}_{\uparrow} and \hat{a}_{\downarrow} transform like

$$\begin{pmatrix} \hat{a}_{\uparrow} \\ \hat{a}_{\downarrow} \end{pmatrix}_{\text{out}} = \underbrace{\begin{pmatrix} \cos(\frac{\gamma}{2}) & -ie^{-i\varphi} \sin(\frac{\gamma}{2}) \\ -ie^{i\varphi} \sin(\frac{\gamma}{2}) & \cos(\frac{\gamma}{2}) \end{pmatrix}}_{\text{T}_{\text{BS}}} \begin{pmatrix} \hat{a}_{\uparrow} \\ \hat{a}_{\downarrow} \end{pmatrix}_{\text{in}} \tag{II.1.14}$$

with $\gamma = \Omega t$. The matrix can be factorized into

$$T_{\text{BS}} = \begin{pmatrix} e^{-i\frac{\varphi}{2}} & 0 \\ 0 & e^{+i\frac{\varphi}{2}} \end{pmatrix} \begin{pmatrix} \cos\left(\frac{\gamma}{2}\right) & -i\sin\left(\frac{\gamma}{2}\right) \\ -i\sin\left(\frac{\gamma}{2}\right) & \cos\left(\frac{\gamma}{2}\right) \end{pmatrix} \begin{pmatrix} e^{+i\frac{\varphi}{2}} & 0 \\ 0 & e^{-i\frac{\varphi}{2}} \end{pmatrix} \quad (\text{II.1.15})$$

which is a sequence of three rotations. The first one is around the z-axis by an angle $-\varphi$, followed by a rotation around the x-axis by an angle γ and the last one around the z-axis again but with the angle $+\varphi$. Therefore a beam splitter performs rotations of the state on the Bloch sphere around an axis which is defined by φ and lies in the x-y-plane. The time evolution operator becomes \hat{U}_x for $\varphi = 0$ and \hat{U}_y for $\varphi = \frac{\pi}{2}$.

A comparison of Equ.II.1.13 and Equ.II.1.6 shows that $\hat{U} = e^{-i\hat{H}_{\text{BS}}t}$ generates the coherent spin state $|\alpha_{\theta,\phi}\rangle$ when acting on $|\alpha_{0,0}\rangle = |\uparrow\rangle$ with $\theta = \Omega t, \phi = \varphi - \frac{\pi}{2}$. This is a CSS achieved from the state $|\uparrow\rangle$ by a rotation with the angle θ around an axis in the x-y-plane.

Let $\omega_0 = \omega_{\uparrow} - \omega_{\downarrow}$ be the energy difference between the two states during the phase evolution. The Hamiltonian reads

$$\hat{H}_{\phi} = \omega_{\uparrow}\hat{a}_{\uparrow}^{\dagger}\hat{a}_{\uparrow} + \omega_{\downarrow}\hat{a}_{\downarrow}^{\dagger}\hat{a}_{\downarrow} = \frac{\omega_0}{2} (\hat{a}_{\uparrow}^{\dagger}\hat{a}_{\uparrow} - \hat{a}_{\downarrow}^{\dagger}\hat{a}_{\downarrow}) = \omega_0\hat{J}_z \quad (\text{II.1.16})$$

and we see that the phase evolution corresponds to a rotation around the z-axis.

As was mentioned before the total particle number operator \hat{N} commutes with the \hat{J}_{κ} and its expectation value is not altered by the time evolution operators build with the Hamiltonians \hat{H}_{BS} and \hat{H}_{ϕ} . Therefore the total particle number is conserved which is of course expected for the Mach-Zehnder interferometer.

A standard interferometric sequence is shown on the Bloch sphere in Fig.II.1.2 and reads

$$|\alpha\rangle_{\text{final}} = e^{-i\hat{J}_x\frac{\pi}{2}} e^{-i\hat{J}_z\phi} e^{-i\hat{J}_x\frac{\pi}{2}} |\alpha_{0,0}\rangle_{\text{initial}}. \quad (\text{II.1.17})$$

We start with all N particles in the $|\alpha_{0,0}\rangle = |\uparrow\rangle$ state which is the same as saying that all particles enter the interferometer through one port. The first beam splitter rotates the state around the x-axis by $\frac{\pi}{2}$ into an equal superposition of $|\uparrow\rangle$ and $|\downarrow\rangle$ which corresponds to $|\alpha_{\frac{\pi}{2},0}\rangle$. During the phase evolution the state is rotated around the z-axis by ϕ and becomes $|\alpha_{\frac{\pi}{2},\phi}\rangle$. The second beam splitter rotates it again by $\frac{\pi}{2}$ around the x-axis¹. The final state depends on the phase ϕ . For $\phi = 0$ it is $|\alpha_{\pi,0}\rangle = |\downarrow\rangle$, for $\phi = \pi$ the initial state $|\alpha_{0,0}\rangle = |\uparrow\rangle$ is recovered. The operator \hat{J}_z transforms as [9]

¹This is equivalent to the statement that the phase evolution does not affect the state but leads to a phase factor $e^{\pm i\frac{\varphi}{2}}$ in front of the \hat{a}_{\uparrow} and \hat{a}_{\downarrow} . In this picture the rotation axis of the second beam splitter changes, which yields the same result

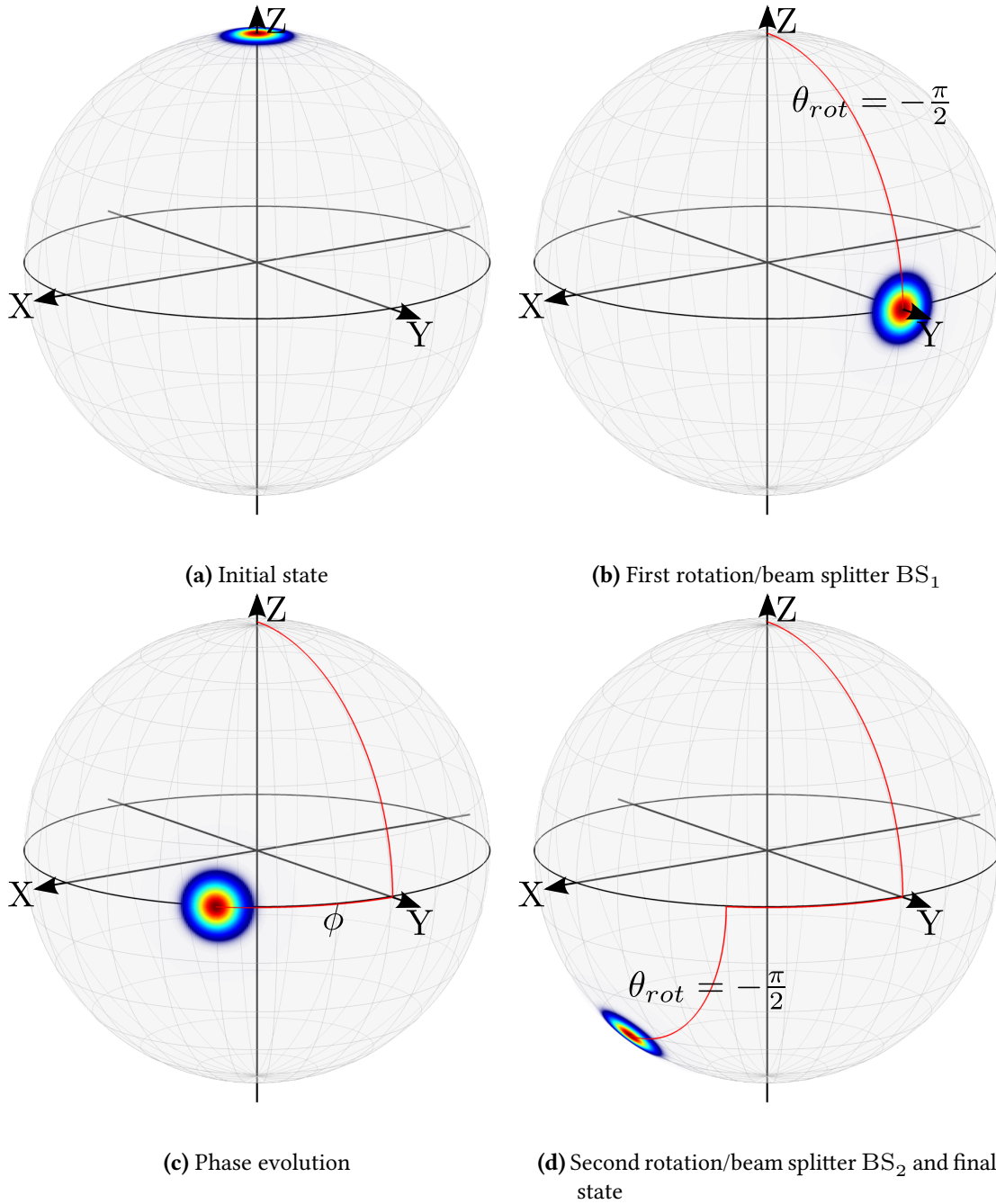


Fig. II.1.2. Mach-Zehnder interferometer sequence on the Bloch sphere. Starting with all atoms in $|\uparrow\rangle$ (a) the first rotation around the x-axis by $\theta = -\frac{\pi}{2}$ brings the system in an equal superposition of $|\uparrow\rangle$ and $|\downarrow\rangle$ (b). After a phase evolution (here $\phi = -\frac{\pi}{4}$, c) a second rotation around the x-axis is done and the projection on the z-axis (half of the population imbalance between $|\uparrow\rangle$ and $|\downarrow\rangle$) is measured. The red line shows the evolution of $(\langle\hat{J}_x\rangle, \langle\hat{J}_y\rangle, \langle\hat{J}_z\rangle)$ during the sequence.

$$\hat{J}_{z,\text{out}} = \sin(\phi)\hat{J}_{x,\text{in}} - \cos(\phi)\hat{J}_{z,\text{in}} \quad (\text{II.1.18})$$

With this we can calculate $\langle \hat{J}_z \rangle$ and its variance $(\Delta \langle \hat{J}_z \rangle)^2 = \langle \hat{J}_z^2 \rangle - \langle \hat{J}_z \rangle^2$ between the two modes at the output of the interferometer. They read

$$\langle \hat{J}_z \rangle(\phi) = -\frac{N}{2} \cos(\phi) \quad (\Delta \langle \hat{J}_z \rangle)^2 = \frac{N}{4} \sin^2(\phi). \quad (\text{II.1.19})$$

Using error propagation the equation for the phase sensitivity is

$$(\Delta \phi)^2 = \frac{(\Delta \langle \hat{J}_z \rangle)^2}{\left(\frac{\partial \langle \hat{J}_z \rangle}{\partial \phi}\right)^2} = \frac{1}{N} \quad (\text{II.1.20})$$

which is the standard quantum or shot noise limit. It can be surpassed by feeding entangled states into the input ports or additional operations inside the interferometer as long as external perturbations and detection noise are small.

In this section we introduced the group representation of a Mach-Zehnder interferometer and had a look at how the beam splitter and phase evolution can be visualized on the Bloch sphere.

II.2. Introduction to $SU(1,1)$

As we have seen the Mach-Zehnder interferometer can be described by using the $SU(2)$ -group. If we replace the passive beam splitter by parametric amplifiers (active beam splitter), this description is no longer valid and we obtain an active $SU(1,1)$ -interferometer [9].

It is described by a three mode system with the modes $|0\rangle$, $|\uparrow\rangle$ and $|\downarrow\rangle$. They are called the pump, signal and idler mode respectively. A parametric amplifier redistributes the particles from the $|0\rangle$ to $|\uparrow\rangle$ and $|\downarrow\rangle$ and vice versa. As described in Ch.I the SCC lead to a redistribution of the atoms between the $|1, 0\rangle$ state and the side modes $|1, -1\rangle$, $|1, +1\rangle$ with a non-linear growth of the side mode population. Thus the SCC correspond to a parametric amplifier in the atom optics and we identify the $|1, 0\rangle$, $|1, -1\rangle$ and $|1, +1\rangle$ with the pump, signal and idler mode respectively.

In this section we introduce the $SU(1,1)$ -group, its operators and a possible way to visualize them. We follow [9, 51], but the $SU(1,1)$ -group and its representation is widely discussed, for instance in [52, 53].

One way to write the defining commutation relations of the $SU(1,1)$ -group is

$$[\hat{K}_x, \hat{K}_y] = -i\hat{K}_z \quad [\hat{K}_y, \hat{K}_z] = i\hat{K}_x \quad [\hat{K}_z, \hat{K}_x] = i\hat{K}_y \quad (\text{II.2.1})$$

with the operators

$$\hat{K}_x = \frac{1}{2} (\hat{a}_\uparrow^\dagger \hat{a}_\downarrow^\dagger + \hat{a}_\uparrow \hat{a}_\downarrow) \quad \hat{K}_y = -\frac{i}{2} (\hat{a}_\uparrow^\dagger \hat{a}_\downarrow^\dagger - \hat{a}_\uparrow \hat{a}_\downarrow) \quad \hat{K}_z = \frac{1}{2} (\hat{a}_\uparrow^\dagger \hat{a}_\uparrow + \hat{a}_\downarrow \hat{a}_\downarrow^\dagger) \quad (\text{II.2.2})$$

where the \hat{a}_\uparrow and \hat{a}_\downarrow fulfil the bosonic commutation relations and represent the signal and idler modes of the SU(1,1)-interferometer. We further define in analogy to Ch.I the operators

$$\hat{\eta} = \hat{a}_\uparrow^\dagger \hat{a}_\uparrow + \hat{a}_\downarrow^\dagger \hat{a}_\downarrow \quad \hat{M} = \hat{a}_\uparrow^\dagger \hat{a}_\uparrow - \hat{a}_\downarrow^\dagger \hat{a}_\downarrow \quad (\text{II.2.3})$$

which are the sum and difference of the population in the $|\uparrow\rangle$ and $|\downarrow\rangle$ states. As in Equ.I.1.18 we call \hat{M} the magnetisation. The \hat{K}_z operator can be written in the form

$$\hat{K}_z = \frac{1}{2} (\hat{a}_\uparrow^\dagger \hat{a}_\uparrow + \hat{a}_\downarrow^\dagger \hat{a}_\downarrow + \frac{1}{2}) = \frac{1}{2} (\hat{\eta} + \frac{1}{2}) \quad (\text{II.2.4})$$

and since it does not commute with the other two operators \hat{K}_x and \hat{K}_y , neither does η . Therefore the sum of the population in the two modes is not conserved for Hamiltonians build out of these operators. However, the particle number difference \hat{M} does commute with these operators and is a conserved quantity. This is contrary to the case of the SU(2)-group where it is just the other way around.

Further we define the raising and lowering operators

$$\hat{K}_+ = \hat{K}_x + i\hat{K}_y = \hat{a}_\uparrow^\dagger \hat{a}_\downarrow^\dagger \quad \hat{K}_- = \hat{K}_x - i\hat{K}_y = \hat{a}_\uparrow \hat{a}_\downarrow \quad (\text{II.2.5})$$

which act on the number states $|M, \eta\rangle$ in the following way

$$\begin{aligned} \hat{K}_+ |M, \eta\rangle &= \sqrt{\left(\frac{\eta}{2} + 1\right)^2 - \left(\frac{M}{2}\right)^2} |M, \eta + 2\rangle \\ \hat{K}_- |M, \eta\rangle &= \sqrt{\left(\frac{\eta}{2}\right)^2 - \left(\frac{M}{2}\right)^2} |M, \eta - 2\rangle. \end{aligned} \quad (\text{II.2.6})$$

Note that the number states are eigenstates of the operators \hat{J}_z and \hat{K}_z with

$$\begin{aligned}\hat{J}_z |M, \eta\rangle &= \frac{M}{2} |M, \eta\rangle \\ \hat{K}_z |M, \eta\rangle &= \frac{1}{2} (\eta + 1) |M, \eta\rangle.\end{aligned}\tag{II.2.7}$$

II.2.1. Action of K_x, K_y, K_z

In the same way as we used the \hat{J}_κ for the $SU(2)$ -Mach-Zehnder interferometer we will describe the single components of the ideal $SU(1,1)$ -interferometer in terms of the previously introduced operators \hat{K}_κ . Analogue to the procedure before we are interested in the transformation of the \hat{K}_κ operators and their expectation values

$$\begin{pmatrix} \hat{K}_x \\ \hat{K}_y \\ \hat{K}_z \end{pmatrix}_{\text{out}} = \hat{U}_\kappa^\dagger \begin{pmatrix} \hat{K}_x \\ \hat{K}_y \\ \hat{K}_z \end{pmatrix}_{\text{in}} \hat{U}_\kappa \quad \text{with } \hat{U}_\kappa = e^{-i\hat{K}_\kappa \gamma}.\tag{II.2.8}$$

The transformation of the bosonic operators \hat{a}_\uparrow and \hat{a}_\downarrow reads in matrix form

$$\begin{pmatrix} \hat{a}_\uparrow \\ \hat{a}_\downarrow \end{pmatrix}_{\text{out}} = T_\kappa \begin{pmatrix} \hat{a}_\uparrow \\ \hat{a}_\downarrow \end{pmatrix}_{\text{in}}\tag{II.2.9}$$

and we find for $\hat{U}_x = e^{-i\hat{K}_x \beta}$ and $\hat{U}_y = e^{-i\hat{K}_y \beta}$ the matrices

$$T_x = \begin{pmatrix} \cosh\left(\frac{\beta}{2}\right) & -i \sinh\left(\frac{\beta}{2}\right) \\ i \sinh\left(\frac{\beta}{2}\right) & \cosh\left(\frac{\beta}{2}\right) \end{pmatrix}, \quad T_y = \begin{pmatrix} \cosh\left(\frac{\beta}{2}\right) & -\sinh\left(\frac{\beta}{2}\right) \\ -\sinh\left(\frac{\beta}{2}\right) & \cosh\left(\frac{\beta}{2}\right) \end{pmatrix}\tag{II.2.10}$$

and for $\hat{U}_z = e^{-i\hat{K}_z \phi}$

$$T_z = \begin{pmatrix} e^{-i\frac{\phi}{2}} & 0 \\ 0 & e^{i\frac{\phi}{2}} \end{pmatrix}.\tag{II.2.11}$$

As expected, these differ from the transformation matrices for the $SU(2)$ -group in Equ.II.1.11. The outgoing operators \hat{a}_\uparrow and $\hat{a}_\downarrow^\dagger$ are now composed from the corresponding lowering *and* raising operators. The trigonometric functions are replaced by their hyperbolic counterparts. Also worth mentioning is that the transformation by \hat{U}_z leads to a negative (positive) sign in the phase factor for both lowering (raising) operators. With these results the outgoing expectation values for a transformation with \hat{U}_x read [9]

$$\begin{aligned}
 \begin{pmatrix} \langle \hat{K}_x \rangle \\ \langle \hat{K}_y \rangle \\ \langle \hat{K}_z \rangle \end{pmatrix}_{\text{out}} &= \begin{pmatrix} 1 & 0 & 0 \\ 0 & \cosh(\beta) & \sinh(\beta) \\ 0 & \sinh(\beta) & \cosh(\beta) \end{pmatrix} \begin{pmatrix} \langle \hat{K}_x \rangle \\ \langle \hat{K}_y \rangle \\ \langle \hat{K}_z \rangle \end{pmatrix}_{\text{in}} \\
 \Leftrightarrow \begin{pmatrix} \hat{K}_x \\ \hat{K}_y \\ \hat{K}_z \end{pmatrix}_{\text{out}} &= e^{i\hat{K}_x\beta} \begin{pmatrix} \hat{K}_x \\ \hat{K}_y \\ \hat{K}_z \end{pmatrix}_{\text{in}} e^{-i\hat{K}_x\beta}.
 \end{aligned} \tag{II.2.12}$$

This is equivalent to a Lorentz boost along the y-axis. The \hat{U}_y results in a similar expression whilst the \hat{U}_z gives a rotation around the z-axis.

$$\begin{aligned}
 \begin{pmatrix} \langle \hat{K}_x \rangle \\ \langle \hat{K}_y \rangle \\ \langle \hat{K}_z \rangle \end{pmatrix}_{\text{out}} &= \begin{pmatrix} \cos(\phi) & -\sin(\phi) & 0 \\ \sin(\phi) & \cos(\phi) & 0 \\ 0 & 0 & 0 \end{pmatrix} \begin{pmatrix} \langle \hat{K}_x \rangle \\ \langle \hat{K}_y \rangle \\ \langle \hat{K}_z \rangle \end{pmatrix}_{\text{in}} \\
 \Leftrightarrow \begin{pmatrix} \hat{K}_x \\ \hat{K}_y \\ \hat{K}_z \end{pmatrix}_{\text{out}} &= e^{i\hat{K}_z\phi} \begin{pmatrix} \hat{K}_x \\ \hat{K}_y \\ \hat{K}_z \end{pmatrix}_{\text{in}} e^{-i\hat{K}_z\phi}
 \end{aligned} \tag{II.2.13}$$

A boost along any direction in the x-y-plane is achieved in a similar way as rotations around any axis were realised for the $SU(2)$ -group (Equ.II.1.15). The matrix reads

$$\begin{aligned}
 T_{\text{boost}} &= \begin{pmatrix} e^{-i\frac{\varphi}{2}} & 0 \\ 0 & e^{+i\frac{\varphi}{2}} \end{pmatrix} \begin{pmatrix} \cosh\left(\frac{\beta}{2}\right) & -i\sinh\left(\frac{\beta}{2}\right) \\ i\sinh\left(\frac{\beta}{2}\right) & \cosh\left(\frac{\beta}{2}\right) \end{pmatrix} \begin{pmatrix} e^{+i\frac{\varphi}{2}} & 0 \\ 0 & e^{-i\frac{\varphi}{2}} \end{pmatrix} \\
 &= \begin{pmatrix} \cosh\left(\frac{\beta}{2}\right) & -ie^{-i\varphi}\sinh\left(\frac{\beta}{2}\right) \\ ie^{i\varphi}\sinh\left(\frac{\beta}{2}\right) & \cosh\left(\frac{\beta}{2}\right) \end{pmatrix}
 \end{aligned} \tag{II.2.14}$$

The Hamiltonian which leads to this transformation matrix is

$$\begin{aligned}
 \hat{H}_{\text{boost}}(\lambda, \varphi) &= \frac{\lambda}{2} (e^{-i\varphi} \hat{a}_\uparrow^\dagger \hat{a}_\downarrow^\dagger + e^{i\varphi} \hat{a}_\uparrow \hat{a}_\downarrow) = \frac{\lambda}{2} (e^{-i\varphi} \hat{K}_+ + e^{i\varphi} \hat{K}_-) \\
 &= \lambda (\cos(\varphi) \hat{K}_x + \sin(\varphi) \hat{K}_y)
 \end{aligned} \tag{II.2.15}$$

with $\beta = \lambda t$ and $\hat{U}_{\text{boost}} = e^{-i\hat{H}_{\text{boost}}t}$.

II.2.2. Coherent states of $SU(1,1)$ -group and visualisation on an hyperbolic surface

The Bloch sphere provides a nice representation of the $SU(2)$ -Mach-Zehnder interferometer in terms of rotations of coherent spin states on the sphere. In this section we want to look at the coherent states of the $SU(1,1)$ -group and introduce a similar way to visualise the boosts and rotations of the $SU(1,1)$ -group.

The minimal value for η is $|M|$. We define $|\alpha_{\beta, \phi}\rangle$ to be the final state after a boost along the x-axis with strength β and a subsequent rotation around the z-axis by an angle ϕ for an initial number state $|M, \eta = |M|\rangle$. That is

$$|\alpha_{\beta, \phi}\rangle_M = e^{-i\hat{K}_z\phi} e^{-i\hat{K}_y\beta} |M, \eta = |M|\rangle \quad (\text{II.2.16})$$

$$= e^{-i\hat{H}_{\text{boost}}(\lambda, \varphi)t} |M, \eta = |M|\rangle \quad (\text{II.2.17})$$

where we used the Hamiltonian \hat{H}_{boost} from Equ.II.2.15 with $\phi = \varphi - \frac{\pi}{2}$ and $\beta = \lambda t$. For a state $|M, \eta = |M|\rangle$ the expectation value of \hat{K}_z is $\frac{|M|+1}{2}$ while those for \hat{K}_x and \hat{K}_y vanish. The expectation values after a time evolution given by $\hat{U}_{\text{boost}} = e^{-i\hat{H}_{\text{boost}}(\lambda, \varphi)t}$ are

$$\begin{aligned} \vec{\alpha}_{\beta, \phi} &= \begin{pmatrix} \langle \hat{K}_x \rangle \\ \langle \hat{K}_y \rangle \\ \langle \hat{K}_z \rangle \end{pmatrix}_{\text{out}} = \langle \hat{K}_z \rangle_{\text{in}} \begin{pmatrix} \sinh(\beta) \cos(\phi) \\ \sinh(\beta) \sin(\phi) \\ \cosh(\beta) \end{pmatrix} \\ &\Leftrightarrow \begin{pmatrix} \hat{K}_x \\ \hat{K}_y \\ \hat{K}_z \end{pmatrix}_{\text{out}} = e^{i\hat{H}_{\text{boost}}(\lambda, \varphi)t} \begin{pmatrix} 0 \\ 0 \\ \hat{K}_z \end{pmatrix}_{\text{in}} e^{-i\hat{H}_{\text{boost}}(\lambda, \varphi)t}. \end{aligned} \quad (\text{II.2.18})$$

These vectors are the coordinates for points on an hyperbolic surface. The exponent in Equ.II.2.17 reads

$$\begin{aligned} -i\frac{\lambda t}{2} \left(e^{-i\varphi} \hat{K}_+ + e^{i\varphi} \hat{K}_- \right) &= -\frac{\beta}{2} e^{-i\phi} \hat{K}_+ + \frac{\beta}{2} e^{i\phi} \hat{K}_- \\ &= \xi \hat{K}_+ - \xi^* \hat{K}_- \end{aligned} \quad (\text{II.2.19})$$

with $\phi = \varphi - \frac{\pi}{2}$ and $\xi = -\frac{\beta}{2}e^{-i\phi}$. Using this Equ.II.2.17 becomes

$$|\alpha_{\beta,\phi}\rangle_M = e^{\xi\hat{K}_+ - \xi^*\hat{K}_-} |M, \eta = |M|\rangle. \quad (\text{II.2.20})$$

which is the analogue to Equ.II.1.6 and we see that the $|\alpha_{\beta,\phi}\rangle$ are the coherent states of the SU(1,1)-group ([51, 54]) which are not orthogonal but form a basis. We set $k = \frac{|M|+1}{2}$ and $\mu = k + n \Rightarrow \eta = 2\mu - 1$ where n is an integer number equal or larger zero. The number states can then be written in the form

$$|M, \eta\rangle \longrightarrow |k, \mu\rangle = |k, k + n\rangle. \quad (\text{II.2.21})$$

The previous equation becomes [49]

$$\begin{aligned} |\alpha_{\beta,\phi}\rangle_M = |\zeta\rangle &= e^{\xi\hat{K}_+ - \xi^*\hat{K}_-} |k, k\rangle = (1 - |\zeta|^2)^k e^{\zeta\hat{K}_+} |k, k\rangle \\ &= (1 - |\zeta|^2)^k \sum_{n=0}^{\infty} \sqrt{\frac{\Gamma(n+2k)}{n! \Gamma(2k)}} \zeta^n |k, k + n\rangle \end{aligned} \quad (\text{II.2.22})$$

with $\zeta = -\tanh\left(\frac{\beta}{2}\right)e^{-i\phi}$ and Γ being the gamma function. Analogue to the Husimi distribution (Equ.II.1.8) calculated with the CSS on the Bloch sphere for the SU(2), we can know use the coherent states of the SU(1,1)-group to visualise their contributions to a particular state described by the density matrix $\hat{\rho}$ on the hyperbolic surface via

$$Q(\alpha_{\beta,\phi}) = \langle \alpha_{\beta,\phi} | \hat{\rho} | \alpha_{\beta,\phi} \rangle. \quad (\text{II.2.23})$$

Figure II.2.1 and II.2.2 show this for coherent and number states with differing η .

In this section we introduced the SU(1,1)-group and their defining operators \hat{K}_x , \hat{K}_y and \hat{K}_z . The transformation of their expectation values for evolution operators of the kind $\hat{U}_\kappa = e^{-i\hat{K}_\kappa\gamma}$ was discussed and we found that the coherent states $|\alpha_{\beta,\phi}\rangle$ of the SU(1,1)-group are created by a Lorentz-boost of strength β along the x-axis and a subsequent rotation around the z-axis by an angle ϕ . These states can be represented on an hyperbolic surface which is the SU(1,1) analogue to the Bloch sphere.

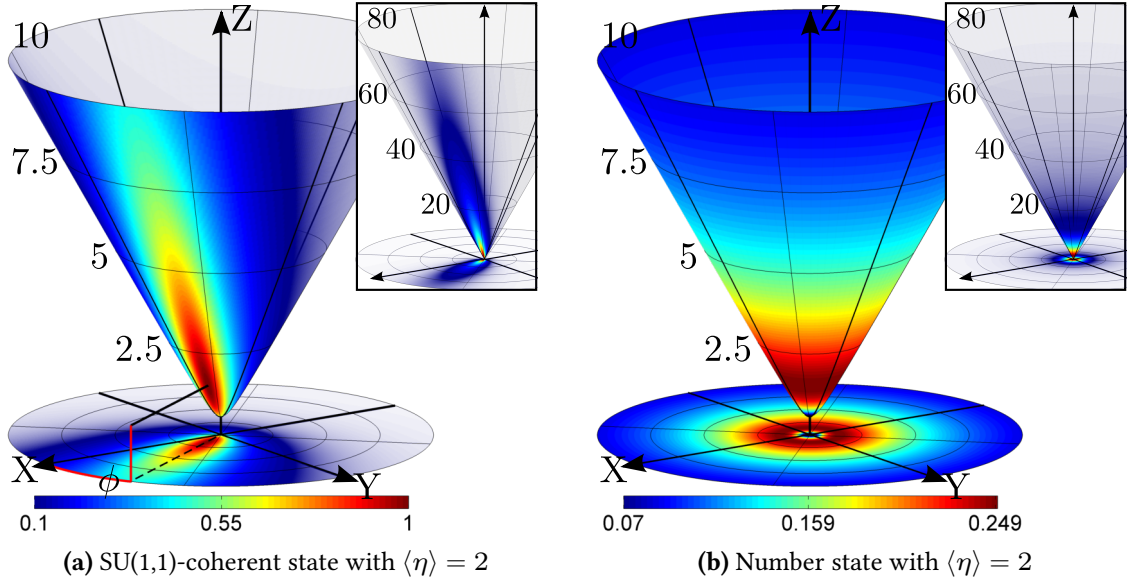


Fig. II.2.1. **a)** $SU(1,1)$ -coherent and **b)** number state both with $\langle \eta \rangle = 2$ in Husimi representation on the hyperbolic surface. The colour codes the overlap with the $SU(1,1)$ -coherent states at the respective positions on the hyperbolic surface and the projection onto the x-y-plane. In contrast to the Bloch sphere the z-axis is a measure for the population sum η since $\langle \hat{K}_z \rangle = \frac{1}{2}(\langle \eta \rangle + 1)$.

a) Analogue to the $SU(2)$ case the coherent state $|\alpha_{\beta, \phi}\rangle$ has an angle ϕ relative to the x-axis. The z-component is given by a Lorentz-boost with strength β . The intersection of the horizontal line at $z = 1.5$ with the surface shows the position $(\langle \hat{K}_x \rangle, \langle \hat{K}_y \rangle, \langle \hat{K}_z \rangle)$ of the $|\alpha_{\beta, \phi}\rangle$ state. In contrast to the coherent state of the $SU(2)$ -group on the Bloch sphere the Husimi distribution is no longer radially symmetric but stretches out far beyond the actual expectation value of \hat{K}_z . For comparison the same colour scale as in Fig.II.1.1a was chosen.

b) Number state on the hyperbolic surface with $\langle \eta \rangle = 2$. The x-y-projection shows that the phase is again completely undetermined. It shall be emphasized again that a number state has no fluctuations in the z-direction.

The respective insets have the same colour scale and show the full extent of the Husimi distributions. The numerical calculations were performed in the $M = 0$ manifold and β was chosen such that $\langle \eta \rangle = 2$, that is $\langle \hat{K}_z \rangle = 1.5$.

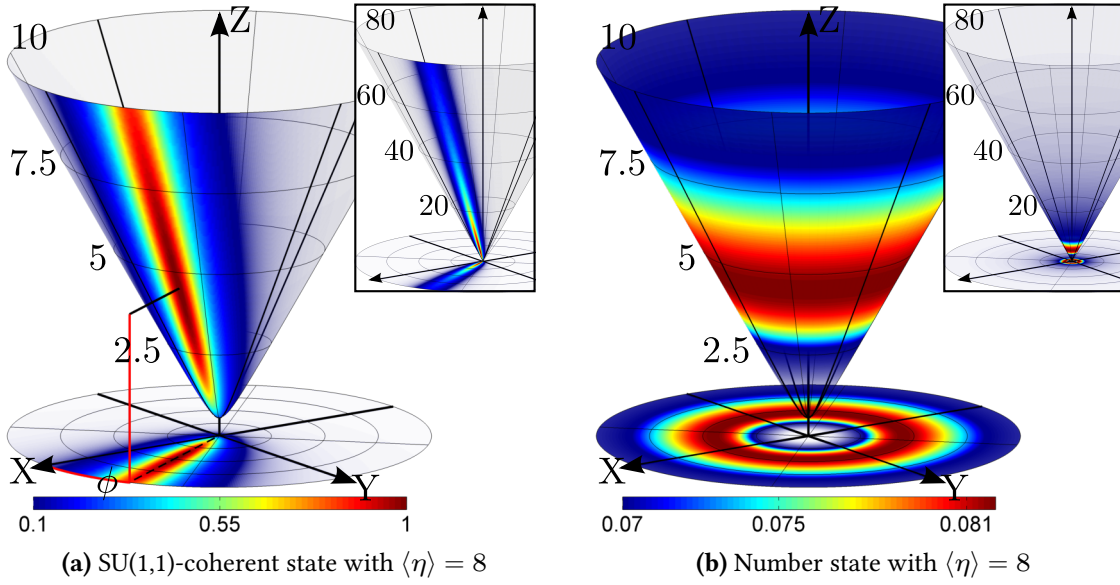


Fig. II.2.2. $SU(1,1)$ -coherent (a) and number state (b) with $\langle \eta \rangle = 8$ in Husimi representation on the hyperbolic surface. The figures show the same as in Fig.II.2.1 but with $\langle \eta \rangle = 8$. Note that the distribution of the coherent state stretches now further up but is narrower in the ϕ -direction.

II.3. The ideal $SU(1,1)$ -interferometer

In this section we consider the $SU(1,1)$ -interferometer within the framework of the previously introduced $SU(1,1)$ -group. As mentioned before the beam splitters in the Mach-Zehnder interferometer are replaced with parametric amplifiers (PA) which are realised by spin changing collisions in atom optics. We follow mainly [10]. Figure II.3.1 shows the interferometer schematically. The $|0\rangle$ state is called the pump mode, $|\uparrow\rangle$ and $|\downarrow\rangle$ the signal and idler mode respectively (Sec.II.2).

A constant magnetic field is applied in the experiment and the resulting energy difference between the $|0\rangle$ and the two side modes hinders the SCC (Sec.I.1.4). The pump beam “passing through” the parametric amplifier corresponds to shining in suitable microwave radiation and thereby shifting the energy of the $|0\rangle$ state to the same level as the two side modes. Now the SCC are energetically allowed and two atoms in the $|0\rangle$ state can scatter into the $|\uparrow\rangle$ and $|\downarrow\rangle$ state and - if the side modes are already populated - vice versa.

II.3.1. Interferometric sequence

Let us start with the theoretical description of the interferometer. As we have seen in Ch.I the SCC are described by the Hamiltonian Equ.I.1.49. To get an analytic expression for the phase

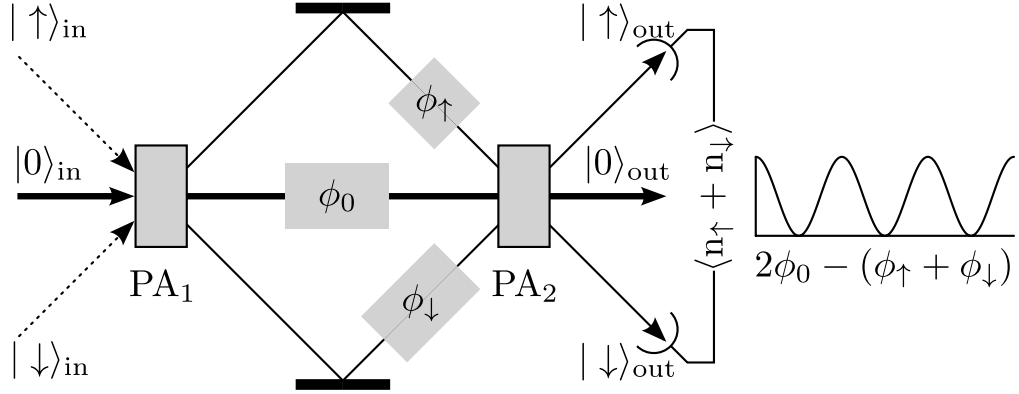


Fig. II.3.1. $SU(1,1)$ interferometer. In the sequence employed in the experiment, the incoming signal and idler modes ($|\uparrow\rangle_{\text{in}}, |\downarrow\rangle_{\text{in}}$) are empty. When the pump ($|0\rangle_{\text{in}}$) passes through the first parametric amplifier correlated particle pairs are produced in the side modes. After mode-dependent phase evolution the three beams pass a second parametric amplifier. The particle sum in $|\uparrow\rangle_{\text{out}}$ and $|\downarrow\rangle_{\text{out}}$ shows a sinusoidal dependence on the relative phases between the pump, signal and idler modes [9, 55].

In our experiments the three modes are the magnetic substates in the internal spin degree of freedom in the $F = 1$ hyperfine level of the electronic ground state of ^{87}Rb . The beams “passing through” a parametric amplifier corresponds to matching the energies of the $|0\rangle$, $|\uparrow\rangle$ and $|\downarrow\rangle$ states with microwave dressing.

sensitivity $\Delta\phi$ we assume to stay in the *non-depletion limit* throughout the whole interferometric sequence. This holds for large atom numbers, a suitable chosen q and short evolution times for the SCC such that $n_0 \approx N_{\text{tot}}$ and $2\hat{n}_0 - 1 + \frac{q}{\lambda} \approx 0$.

With this we can approximate the Hamiltonian by

$$\begin{aligned} \hat{H}_{\text{PA}} &= 2\lambda (\hat{a}_0 \hat{a}_0 \hat{a}_\uparrow^\dagger \hat{a}_\downarrow^\dagger + \hat{a}_0^\dagger \hat{a}_0^\dagger \hat{a}_\uparrow \hat{a}_\downarrow) \approx 2\lambda n_0 (\hat{a}_\uparrow^\dagger \hat{a}_\downarrow^\dagger + \hat{a}_\uparrow \hat{a}_\downarrow) \\ &= 4\lambda n_0 \hat{K}_x \end{aligned} \quad (\text{II.3.1})$$

where we replaced $\hat{a}_0 \approx \sqrt{n_0} e^{-i\phi_0}$ and $\hat{a}_0^\dagger \approx \sqrt{n_0} e^{i\phi_0}$ [56] and set the initial phase of the pump mode $\phi_0 = 0$. If we set the $|0\rangle$ mode at zero energy and use $\omega = \omega_\uparrow = \omega_\downarrow$ since both side modes have the same energy, the Hamiltonian during the phase evolution reads

$$\begin{aligned} \hat{H}_\phi &= \omega_\uparrow \hat{a}_\uparrow^\dagger \hat{a}_\uparrow + \omega_0 \hat{a}_0^\dagger \hat{a}_0 + \omega_\downarrow \hat{a}_\downarrow^\dagger \hat{a}_\downarrow \stackrel{\omega_0=0}{=} \omega (\hat{a}_\uparrow^\dagger \hat{a}_\uparrow + \hat{a}_\downarrow^\dagger \hat{a}_\downarrow) \\ &= 2\omega \hat{K}_z. \end{aligned} \quad (\text{II.3.2})$$

Comparing this with Equ.II.2.15 we see that the $S(1,1)$ -interferometer is a sequence of two boosts along the y -axis with strength β and an intermediate rotation around the z -axis by an angle ϕ . The interferometer is shown in Fig.II.3.1 and the corresponding sequence reads

$$\begin{aligned}
 |\alpha\rangle_{\text{final}} &= e^{-i\hat{K}_x\beta} e^{-i\hat{K}_z\phi} e^{-i\hat{K}_x\beta} |\alpha_{0,0}\rangle_{\text{initial}} \quad (\text{II.3.3}) \\
 \text{with } \beta &= 4\lambda n_0 t_{\text{SCC}} \cdot 2\pi \\
 \phi &= 2\omega t_{\text{phase}}.
 \end{aligned}$$

Figure II.3.2 shows the interferometric sequence as boosts and rotation on the hyperbolic surface. The atom number in the pump mode n_0 is close to the total atom number since we are in the non-depletion limit. The parameter λ is determined by the trap geometry and n_0 . Since these are supposed to be constants, the boost strength β depends only on the time t for which the microwave dressing is applied. ω is two times the energy difference between pump mode and side modes and also constant during the sequence. Therefore the phase ϕ depends only on the time t_{phase} between the two boosts. It is scanned by changing the time t_{phase} between the two periods of spin changing collisions, lasting for time t .

Note that in contrast to the Mach-Zehnder interferometer the rotation angle here is given by the sum of the phases of the two side modes assuming $\phi_0 = 0$. Using Equ.II.2.10 and Equ.II.2.11 the transformation of the \hat{a}_\uparrow and $\hat{a}_\downarrow^\dagger$ reads

$$\begin{pmatrix} \hat{a}_\uparrow \\ \hat{a}_\downarrow^\dagger \end{pmatrix}_{\text{final}} = \underbrace{T_x \cdot T_z \cdot T_x}_{T_{SU(1,1)}} \begin{pmatrix} \hat{a}_\uparrow \\ \hat{a}_\downarrow^\dagger \end{pmatrix}_{\text{initial}} \quad (\text{II.3.4})$$

with the transformation matrix

$$T_{SU(1,1)} = \begin{pmatrix} \mu^2 e^{-i\frac{\phi}{2}} + \nu^2 e^{i\frac{\phi}{2}} & -i2\mu\nu \cos\left(\frac{\phi}{2}\right) \\ i2\mu\nu \cos\left(\frac{\phi}{2}\right) & \mu^2 e^{i\frac{\phi}{2}} + \nu^2 e^{-i\frac{\phi}{2}} \end{pmatrix} \quad (\text{II.3.5})$$

where we used $\mu = \cosh\left(\frac{\beta}{2}\right)$ and $\nu = \sinh\left(\frac{\beta}{2}\right)$. We want to know how the atom number in $|\uparrow\rangle$ and $|\downarrow\rangle$ at the output of the interferometer depends on the phase ϕ . Adopting the notation from Ch.I we will call the side mode population at the input, inside and at the output of the interferometer η_{in} , n and η respectively.

We know from Equ.II.2.18 that for an input state $|\alpha_{0,0}\rangle$ ($\eta_{\text{in}} = |M|$) the expectation value of \hat{K}_z after the first boost is $\frac{1}{2}(\eta_{\text{in}} + 1) \cosh \beta$ and therefore the atom number in the side modes *inside* the interferometer is

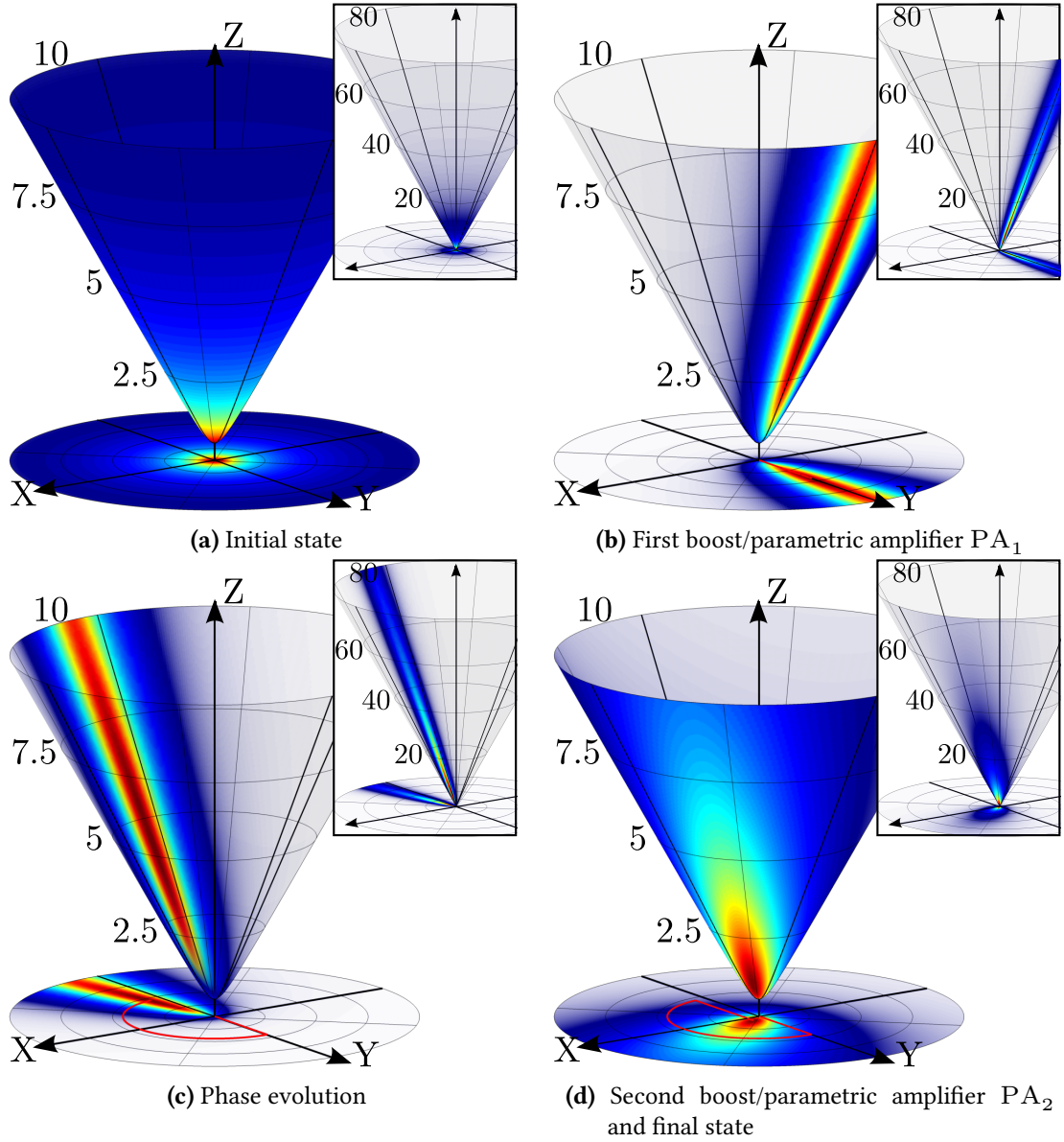


Fig. II.3.2. The $SU(1,1)$ interferometer on the hyperbolic surface. The colour code is the same as in-

Fig.II.2.1a. **a)** The initial state has no atoms in the side modes and $\langle \hat{K}_z \rangle = \frac{1}{2}$. Note that this is number state and it has no fluctuations in the z -direction. As mentioned before this can not be revealed in the Husimi representation. **b)** A first boost with strength β is performed along the y -axis. **c)** The phase evolution corresponds to a rotation around the z -axis by an angle ϕ . **d)** Finally, the state is boosted in the same direction and with the same strength as before. The readout is the sum of the atom numbers in the side modes and thus related to the z component of the pseudospin vector. Its expectation value is given by $2\langle \hat{K}_z \rangle - 1$.

Any boost with $\phi \neq \pi$ that does not reverse the initial Lorentz boost will lead to a mean population of the side modes with fluctuations, both depending on the phase and the strength of the boosts. β was chosen such that $\langle \eta \rangle = 8$ after the first boost as in Fig.II.2.2a and the shown phase evolution has $\phi = 0.95\pi$.

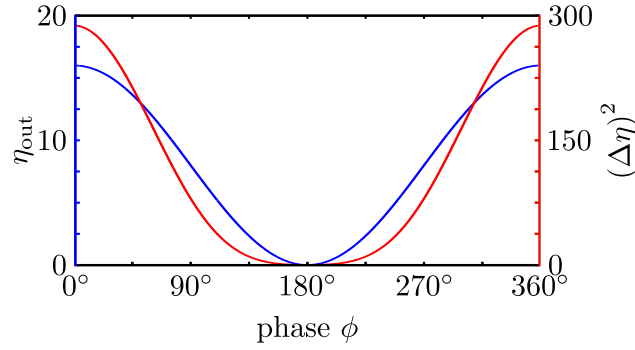


Fig. II.3.3. η_{out} and $(\Delta\eta_{\text{out}})^2$ for $n = 2$ inside the interferometer. In the ideal case without any additional noise contribution $(\Delta\eta_{\text{out}})^2$ flattens faster than η_{out} and the best phase sensitivity is reached at $\phi = \pi$ (blue curve Fig.II.3.4a).

$$\begin{aligned} n &= \eta_{\text{in}} + n_{\text{SCC}} = (\eta_{\text{in}} + 1) \cosh(\beta) - 1 \\ &\Leftrightarrow n_{\text{SCC}} = (\eta_{\text{in}} + 1) (\cosh(\beta) - 1). \end{aligned} \quad (\text{II.3.6})$$

One sees that the number of atoms scattered into the side modes (n_{SCC}) increases with increasing initial population η_{in} (seed) for constant boost strength β . If the side modes are initially empty this becomes

$$n = \cosh(\beta) - 1 = 2 \sinh^2\left(\frac{\beta}{2}\right) = 2\nu^2. \quad (\text{II.3.7})$$

Using Equ.II.3.5 the outcome $\eta = n_{\uparrow} + n_{\downarrow}$ of the interferometer is then calculated to be

$$\eta = n(n+2)(1 + \cos(\phi)). \quad (\text{II.3.8})$$

For $\phi = 180^\circ$ the second boost reverses the effect of the first one and the side modes are empty again. The variance at the output reads

$$(\Delta\eta)^2 = 2n(n+2)(1 + \cos(\phi)) + [n(n+2)(1 + \cos(\phi))]^2 \quad (\text{II.3.9})$$

and vanishes for $\phi = 180^\circ$. Figure II.3.3 shows a comparison between η and $(\Delta\eta)^2$.

II.3.2. Phase sensitivity

Via error propagation the phase sensitivity is calculated to be

$$(\Delta\phi)^2 = \frac{(\Delta\eta)^2}{\left(\frac{\partial\eta}{\partial\phi}\right)^2} = \frac{1}{1 - \cos(\phi)} \left[\frac{2}{n(n+2)} + (1 + \cos(\phi)) \right]. \quad (\text{II.3.10})$$

The results of Equ.II.3.7 to Equ.II.3.10 can be found in [10]. There it is assumed that the second boost is opposed to the first one giving a phase difference of 180° compared to our results. The phase sensitivity surpasses the SQL of the classical interferometer (Equ.II.1.20) and shows a $\frac{1}{n^2}$ scaling. This is due to the non-linear production of entangled atom pairs in the side modes by the SCC. This purely quantum mechanical effect allows to beat the classical limit. However, this is only the case under certain conditions. The second term has to be small compared to the first one. This means that for a phase ϕ we only find quantum advantage if

$$n \lesssim \sqrt{\frac{3 + \cos(\phi)}{1 + \cos(\phi)}} - 1. \quad (\text{II.3.11})$$

The best phase sensitivity is reached at $\phi = 180^\circ$. There we get

$$(\Delta\phi)_{\phi=\pi}^2 = \frac{1}{n(n+2)}. \quad (\text{II.3.12})$$

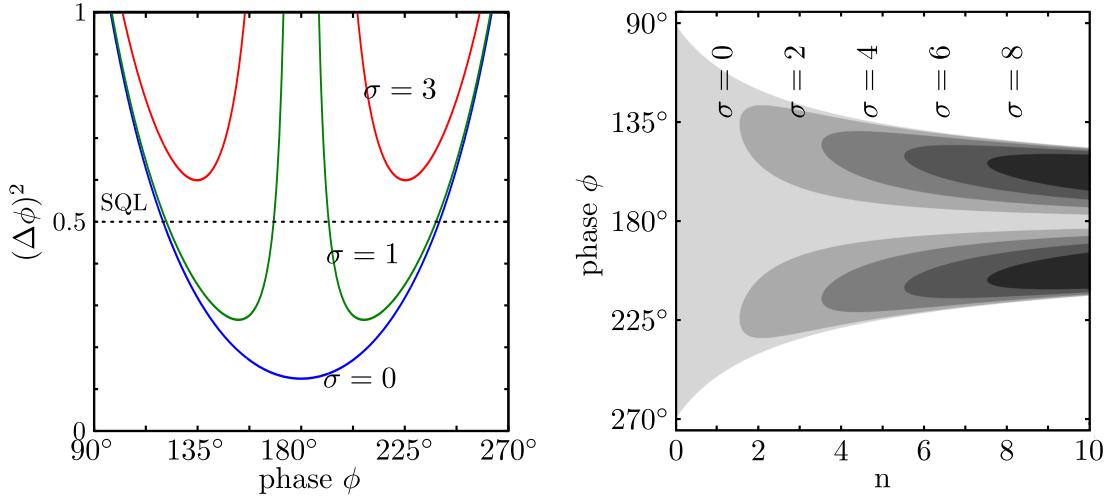
For other values of ϕ the second term does not vanish anymore and the phase region where the SQL is surpassed is given by

$$(\Delta\phi)^2 \leq \frac{1}{n} \quad \Leftrightarrow \quad \cos(\phi) \leq -\frac{n}{n+2}. \quad (\text{II.3.13})$$

However, these results are only valid as long as Equ.II.3.9 is the only contribution to the overall variance. At $\phi = 180^\circ$ the value for η and its first derivative with respect to ϕ as well as $(\Delta\eta)^2$ vanish, leading to a division of zero by zero. The $(\Delta\phi)^2$ does not diverge there because Equ.II.3.9 contains a term quadratic in $\cos(\phi)$ and therefore it decreases faster than η . Additional noise adds a constant term σ_{add}^2 to the variance. Taking this into account the reachable phase sensitivity reads

$$(\Delta\phi)_{\text{noise}}^2 = (\Delta\phi)^2 + \frac{\sigma_{\text{add}}^2}{[n(n+2)\sin(\phi)]^2} \quad (\text{II.3.14})$$

which diverges at the former optimal phase $\phi = 180^\circ$. Figure II.3.4a shows $(\Delta\phi)^2$ with and without detection noise. The SQL can still be surpassed but the region where this is the case is split and narrows down (Fig.II.3.4b).



(a) Phase sensitivity squared ($(\Delta\phi)^2$) for a mean atom number of $n = 2$ inside the interferometer. The three curves are the results for different values of Gaussian noise on the detected atom number variance with $\sigma_{\text{add}} = 0, 1, 3$. The corresponding standard quantum limit is indicated as a dashed line.

(b) Phase regions (grey) where the ideal $SU(1,1)$ interferometer surpasses the SQL depending on the mean side mode occupation inside the interferometer. The different shades of grey correspond to different values of additional Gaussian noise.

Fig. II.3.4. Phase sensitivity of the ideal $SU(1,1)$ interferometer. **a)** Without any additional noise ($\sigma_{\text{add}} = 0$) the best phase sensitivity is reached at $\phi = 180^\circ$ since the variance $(\Delta\eta_{\text{out}})^2$ approaches the zero faster than the mean η_{out} (Fig.II.3.3). The SQL is surpassed in a phase region around $\phi = 180^\circ$. Adding constant noise σ_{add} , e.g. due to detection noise, in Equ.II.3.14 leads to the divergence at the former best point.

b) The phase regions (grey) in which the SQL is surpassed depends on the mean atom number n inside the interferometer. With increasing n the region narrows down. The different shades of grey show the behaviour for additional Gaussian noise.

II.4. Experimental results of the $SU(1,1)$ -interferometer in the non-depleted regime

We will now discuss the experimental results in the non-depleted regime. Initially, all the atoms ($N_{\text{tot}} \approx 500$) are in the $|1, 0\rangle$ state which serves as the pump mode $|0\rangle$. The side modes, $|1, -1\rangle$ and $|1, +1\rangle$, are the corresponding signal ($|\uparrow\rangle$) and idler ($|\downarrow\rangle$) and remain empty. A constant magnetic field ensures that the three magnetic sub states are not mixed.

The standard sequence of the $SU(1,1)$ -interferometer is realised by two equal periods of MW-dressing with a varied waiting time (wt) in between. No dressing is applied during the waiting time. According to Equ.I.1.45 the relevant energy difference between the pump and the side modes during the waiting time is given by

$$\Delta E = 71.89 \text{ Hz/G}^2 \cdot B^2 \quad (\text{II.4.1})$$

which results in a phase of (Equ.II.3.3)

$$\phi = 2\omega_{\text{wt}}. \quad (\text{II.4.2})$$

Therefore we expect an oscillation of the side mode population η at the output of the interferometer versus hold time with a frequency of

$$f = 2 \frac{\omega_{\text{wt}}}{2\pi} = 2 \cdot 71.89 \text{ Hz/G}^2 \cdot B^2. \quad (\text{II.4.3})$$

II.4.1. Interferometric fringes

The output of the interferometer is sensitive to various parameters. Some of them have to be adjusted in the experiment (B-field, dressing and waiting times) while others are post selected in the data analysis (analysed well, total atom number).

Three different parameters were changed in the data analysis for the examples in Fig.II.4.1. These parameters are: dressing time (DT), the selected subset of lattice sites (well) and total atom number N_{tot} .

The two fringes shown in Fig.II.4.1a result from the dataset post selected for the same wells (10, 11, 12) and $N_{\text{tot}} = 500 \dots 600$ but different dressing times in the interferometric sequence. The amplitude of the fringe is larger for a longer dressing time. This is expected since the boost strength β increases with the dressing time (Equ.II.3.3).

However, the theory predicts completely empty side modes at the minima of the fringes inde-

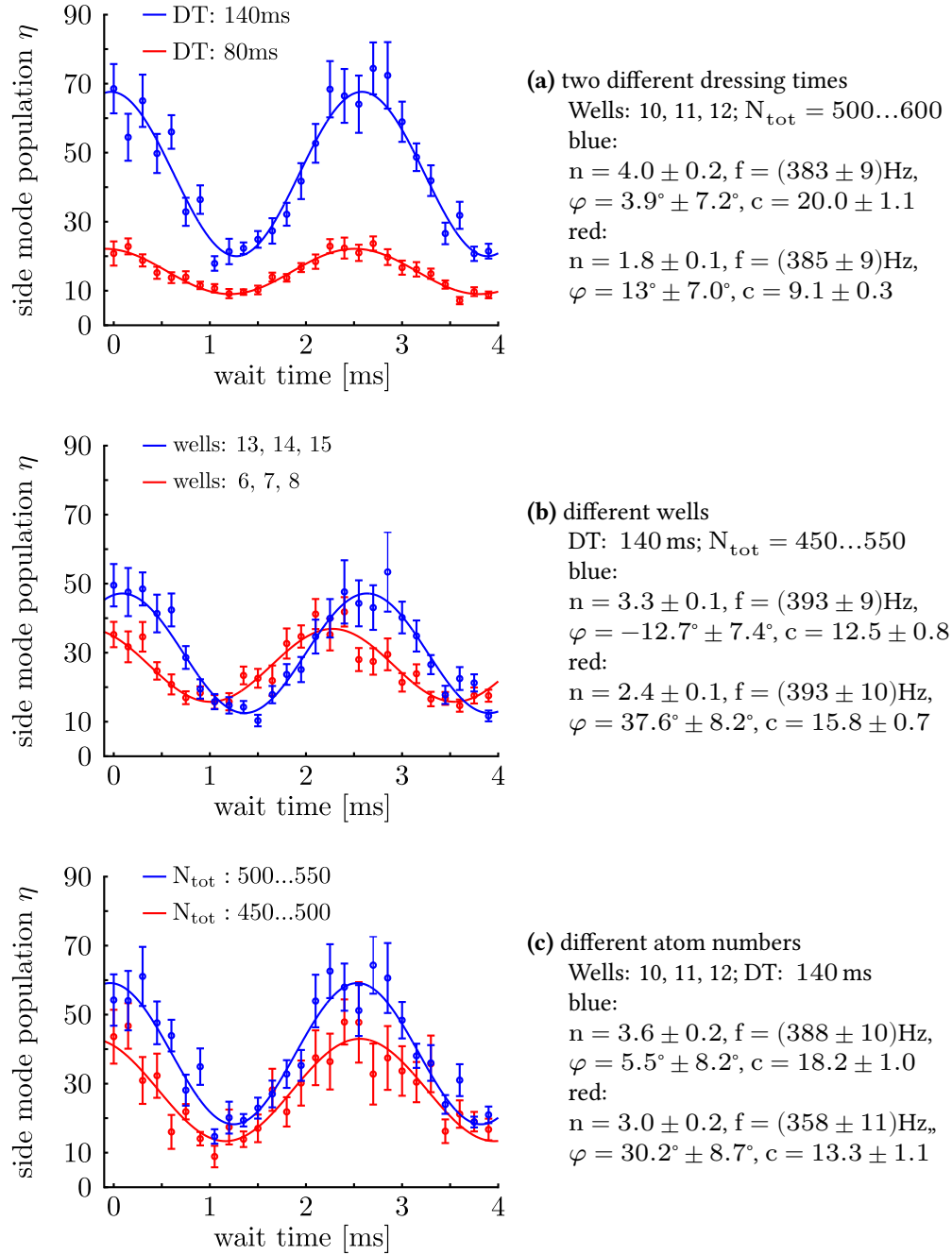


Fig. II.4.1. Experimental fringes in the $SU(1,1)$ -interferometer. The output of the interferometer is sensitive to various parameters. The two fringes in each plot show the result if one parameter is changed while the others remain constant. The lines are fits of Equ.II.3.8 with an additive constant c and an additional phase φ . **a)** The offset and amplitude of the fringe increase with a longer dressing time due to a larger boost strength β . The increase in the amplitude is expected whereas perfect reversal is expected also for stronger boosts. **b)** Choosing different wells results in different values of φ due to different q . It also has an impact on the amplitude and the constant offset. This is due to inhomogeneities (e. g. MW-power gradient, varying N_{tot}) over the lattice. **c)** Post selection of an higher total atom number N_{tot} increases the amplitude due to a larger boost strength β . The atom number enters also in the additional phase term ($n_0 \approx N_{\text{tot}}$) and influences the mean field shift leading to different phase offsets.

pendent of the dressing time, whereas we observe a finite minimal value. Possible reasons will be discussed below.

Figure II.4.1b shows fringes with equal dressing time $DT = 140$ ms and $N_{\text{tot}} = 450 \dots 550$. Choosing distinct wells results in different values of the initial phase φ .

These can be explained with the additional phase term $\lambda \left(2\hat{n}_0 - 1 + \frac{q}{\lambda} \right)$ (Equ.I.1.50) not captured by the non-depletion theory. The MW-power gradient mentioned in Sec.I.2 leads to different values of the Rabi frequency – and hence q (Equ.I.1.48) – in different wells during the dressing periods which causes the additional phase offsets.

The difference in the Rabi frequency between two adjacent lattice sites was determined to be $\Delta\Omega \approx 3.9$ Hz at the measured $\Omega \approx 7.5$ kHz [57]. The change in q due to this is

$$\Delta q = \frac{(\Omega + \Delta\Omega)^2}{4\delta} - \frac{\Omega^2}{4\delta} \approx \frac{\Omega}{2\delta} \Delta\Omega. \quad (\text{II.4.4})$$

The dephasing term is negligible for small evolution times, but its influence increases for longer times. Therefore the phase offset observed is mainly due to the second dressing time. With the used detuning $\delta = 98$ kHz it is estimated to $\Delta q \cdot 140$ ms $\approx 8^\circ$ per lattice site. This yields $\varphi \approx 56^\circ$ between seven wells which agrees with the observed phase difference in II.4.1b.

Also, the different total atom numbers of different lattice sites due to the trapping potential lead to different values for λ , leading to changes in the effective boost strengths in the interferometer and therefore the amplitude.

This can be seen in Fig.II.4.1c, where the data is post selected for the same dressing time $DT = 140$ ms and wells (10, 11, 12). The two fringes differ in the range of the total atom number causing different amplitudes. The atom number enters also in the additional phase term ($n_0 \approx N_{\text{tot}}$) and influences the mean field shift leading to different phase offsets.

During the measurement the constant magnetic field was 1.64G so that equation II.4.3 gives an expected frequency of 387 Hz. All fit results are close to this value.

The fact that we cannot perfectly reverse the first period of spin changing collisions can partially be explained by an additional characterisation of the absorption imaging in the absence of signal. We characterize this by performing additional measurements with empty side modes and analysing the detected atom number distributions in every well and both side modes. Figure II.4.2 shows an atom number distribution for such a measurement in the $|1, -1\rangle$ state in one of the central wells. The mean value is $\mu = 3.6$. The width of $\sigma = 4.8$ characterises our detection noise.

The detected μ depends on the particular well and state whereas the detection noise varies

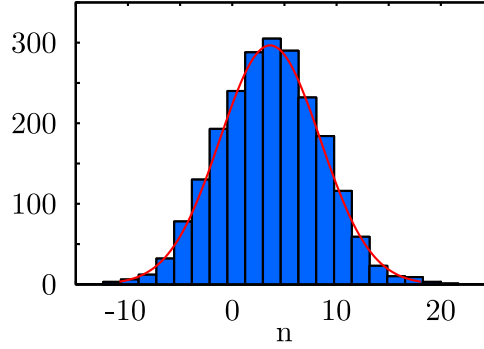


Fig. II.4.2. Measured atom number distribution of regions without atoms. The in Fig.II.4.1 detected offsets can (partially) be explained by analysing data of a measurement without atoms in the side modes. The histogram shows the detected atom number distribution and a Gaussian fit from one well for such a measurement. The analysed region would normally contain atoms in the $|1, -1\rangle$ state. The fit gives a mean offset of $\mu = 3.6$ and width of $\sigma = 4.8$ which is a measure for the detection noise (mainly photon shot noise) in our system. The detection noise is almost constant whereas the offset depends on the well due to imperfections of the absorption imaging.

only slightly. The sum of the distribution means of both states contributes to the offset of the fringes in Fig.II.4.1b.

However, the previous observations cannot explain the entire offset of the fringes. A reason for the imperfect reversal might be atom loss during time evolution if the dressing times are too long. Another assumption is phase jitter due to fluctuations in microwave and B field during the measurement which causes the value of the fringe minimum to increase by averaging over the data.

II.4.2. Phase sensitivity

Having obtained a phase dependent fringe at the output of the interferometer, we now turn to the analysis of the sensitivity of the interferometer. In this measurement, a short dressing time of 90 ms was chosen in order to remain in the non-depleted regime and justify the application of the $SU(1,1)$ theory. Since the phase sensitivity is symmetric with respect to $\phi = 180^\circ$ we focused on the first half of the fringe to be able to acquire more data in the relevant phase region. The phase sensitivity is obtained according to Equ.II.3.10 and depends on the slope of the fringe for the mean atom number in the side modes as well as on the variance of the side mode population. A fit of Equ.II.3.8 gives the frequency and phase offset which allow the transformation of the experimental waiting time into a phase. It also yields a value n for the atoms in the side modes inside the interferometer and the slope $\frac{\partial \eta}{\partial \phi}$ of the measured fringe. This value of n is used to

calculate the applicable standard quantum limit for comparison.

The variance $(\Delta\eta)^2$ of the output side mode population η is calculated and corrected by subtracting the detection noise obtained from interleaved measurements with empty side modes. A resampling method as discussed in Sec.I.2.2 is used to calculate the errors of the variances.

The corrected variance is divided by the squared slope of the fringe to obtain the phase sensitivity.

Figure II.4.3a and II.4.3b show examples for fringes (blue) and variances (red). The curves are fits of the corresponding equations (Equ.II.3.8, Equ.II.3.9) yielding values for n and the slope $\frac{\partial\eta}{\partial\phi}$. Figure II.4.3c and II.4.3d show the inferred phase sensitivity corresponding to **a**) and **b**) respectively. The blue lines are fits of the equation for the phase sensitivity $\Delta\phi$ (square root of Equ.II.3.10) to the data. The red dotted lines are the theoretical results for $\Delta\phi$ calculated with the n resulting from the fit to the fringes in **a**) and **b**) and the horizontal line depicts the SQL for the same n .

The data points around $\phi = 120^\circ$ ($\Delta\phi \approx (0.6 \pm 0.4)$ at $\phi \approx 135^\circ$) indicate that the SQL can be surpassed with our experimental setup. The comparison of **c**) and **d**) shows the significance of a correct post selection of the data on the result.

Differences in the atom numbers affect the additional phase term resulting in different phase offsets. We see that the data points in Fig.II.4.3b and II.4.3d (smaller N_{tot} than in **a** and **b**) are at phase values up to $\approx 170^\circ$. In this phase region the former discussed problem of the “zero by zero” division starts to play a role since the measured variance does not entirely vanish (Equ.II.3.14).

Extraction of λ from experimental observations

In the following sections we want to use the theory of Ch.I for comparison with experimental results and further theoretical predictions. For that reason the parameter λ will be extracted with help of the ideal $SU(1,1)$ -theory valid only in the non-depletion regime.

Equation II.3.7 gives the connection between the boost strength β and the atom number n in the side modes inside the interferometer. The parameter λ can be calculated from β from Equ.II.3.3 in the following way

$$\lambda = \frac{\cosh^{-1}(n+1)}{4n_0 t_{\text{SCC}} \cdot 2\pi}. \quad (\text{II.4.5})$$

Using $n = 1.3 \pm 0.1$ from the fit in Fig.II.4.3a, $n_0 \approx \bar{N}_{\text{tot}} = 470$ and the duration time of the initial SCC ($t_{\text{SCC}} = 90$ ms) we get $|\lambda| \approx (1.4 \pm 0.1)$ mHz.

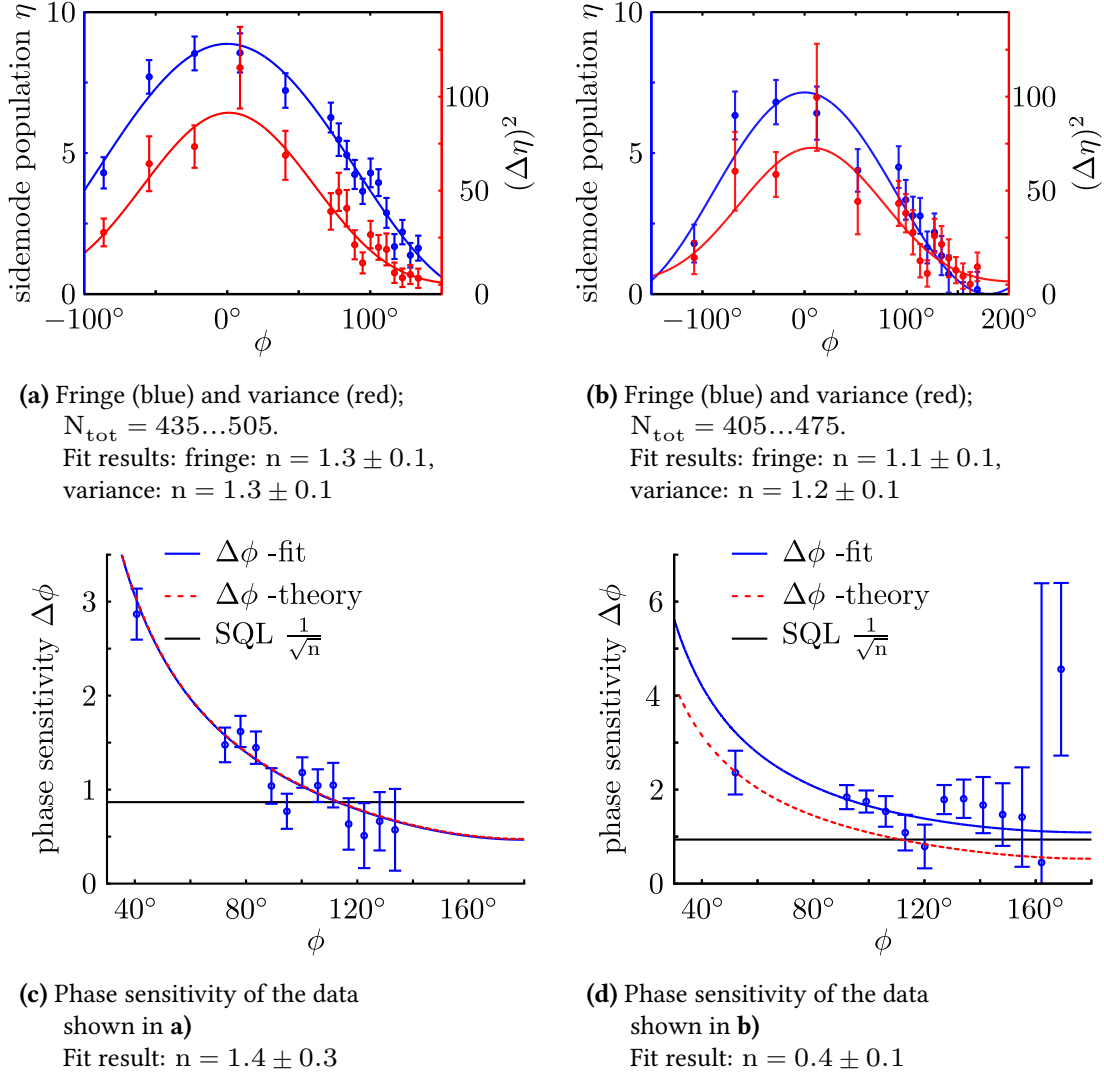


Fig. II.4.3. Fringe, variance and phase sensitivity of the SU(1,1)-interferometer.

a), b) Fringe (blue) of mean and variance (red). During the measurement we collected data analogue to those shown in Fig.II.4.2. The offset μ was subtracted from the fringe and the photon shot noise σ^2 from the variance. Equation II.3.8 (Equ.II.3.9) was fitted to the fringe (variance) yielding a value for the atom number n inside the interferometer.

a) shows the fringes for a larger post-selected atom number N_{tot} than **b)**.

c), d) Inferred phase sensitivity for **a)** and **b)**, respectively. The blue line is a fit of the square root of Equ.II.3.10 to the inferred data points. The red line is the theoretical result, the black line the SQL. Both are calculated using the value of n resulting from the fit to the fringes in **a)** and **b)**.

The comparison of **c)** and **d)** shows the significance of a correct post selection of the data on the result. Already minor changes in the selected N_{tot} affect the phase offset such that the former discussed problem of the “zero by zero” division starts to play a role since the measured variance does not entirely vanish (Equ.II.3.14).

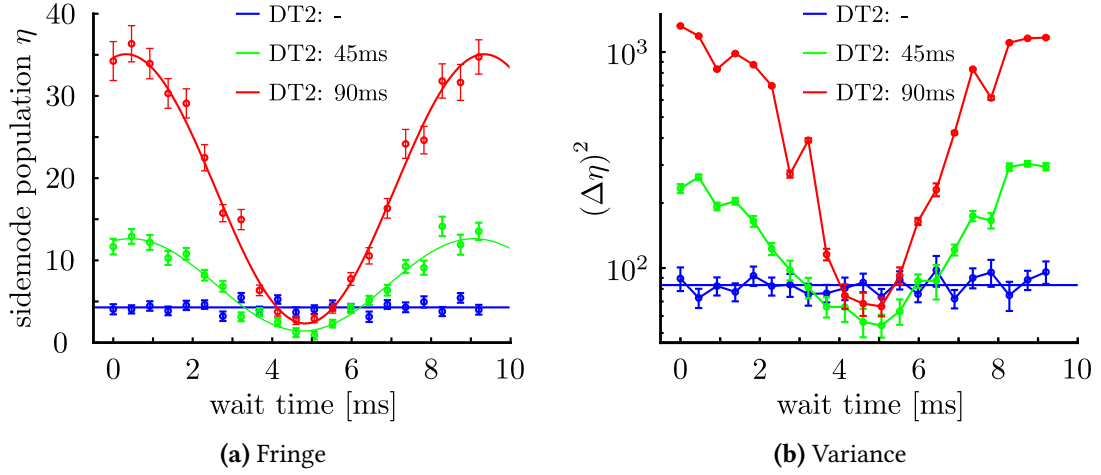


Fig. II.4.4. Fringe of mean occupancy and variance for fixed dressing time ($DT1 = 90$ ms) in the first beam splitter and varied second dressing time ($DT2$). **a)** Fringes of mean side mode occupancy. Without any second dressing time the atom number in the side modes is constant for different wait times as expected (blue line). A second dressing leads to the appearance of the known sinusoidal shape with the minima falling below the blue line. The plot also shows the non-linear amplification of the atom number in the side modes depending on the wait time. **b)** The corresponding variances (logarithmic scale) show the same behaviour.

This demonstrates that the second dressing partially reverses the initial SCC at $\phi = \pi$. The fact that the minimum for $DT1 \neq DT2 = 45$ ms is below the minimum for $DT1 = DT2 = 90$ ms shows that the reversal is not perfect as predicted by the $SU(1,1)$ theory for the latter case (Fig.II.3.3).

II.4.3. Varying the second dressing time in the $SU(1,1)$ -interferometer

The previously mentioned offset of the interferometry fringes raises the question of the reversibility of the ideal process in the case of a phase shift of π during phase evolution. To check this we performed measurements where the first dressing time ($DT1$) was kept constant at 90 ms and the second dressing time ($DT2$) was varied. For each dressing time, a number of data points with different wait times corresponding to one period of a fringe was recorded.

Figure II.4.4a shows the result of such a measurement for three different $DT2$. The constant offset due to the detection (Fig.II.4.2) is subtracted.

The blue points correspond to data collected without a second dressing period. As expected, the outcome does not depend on the waiting time. These data points give the atom number in the side modes measured after one SCC-evolution for 90 ms. The blue line marks the mean value.

The green and red data show the outcome for two different second dressing times $DT2 = 45$ ms (green) and $DT2 = 90$ ms (red). The lines are fits of Equ.II.3.9 with an additive constant yielding the frequencies $f = (115 \pm 6)$ Hz and $f = (111 \pm 4)$ Hz for $DT2 = 45$ ms and $DT2 = 90$ ms

respectively. Evidently, the frequency is independent of the second dressing time. It is also in good agreement with the theoretical value of $f = 119$ Hz at the experimental magnetic field $B = 0.91$ G (Equ.II.4.3).

The ideal theory predicts perfect reversal at the fringe minimum for two equal periods ($DT1 = DT2$) spin-changing collisions (Fig.II.3.3). It is observable from the graph that the first SCC are partially reversed since the minima are considerably below the blue data points. However, contrary to expectation the reversal is better for $DT2 < DT1$ and the minimal value is not zero.

Figure II.4.4b shows the significant reduction of the corresponding variances at the minima of the fringe.

Figure II.4.5a depicts the described fringes in a different manner and with more different $DT2$, Fig.II.4.5b shows a corresponding numerical calculation with the same values for $B = 0.91$ G, $\Omega = 5.41$ kHz and $\bar{N}_{\text{tot}} = 600$ as in the experiment. The detuning $\delta = 125$ kHz ($\delta_{\text{exp}} = 197$ kHz) and $\lambda = -1.8$ mHz were adjusted to resemble the experimental result. The found λ differs from the previously determined and the two values should be understood as a rough estimation.

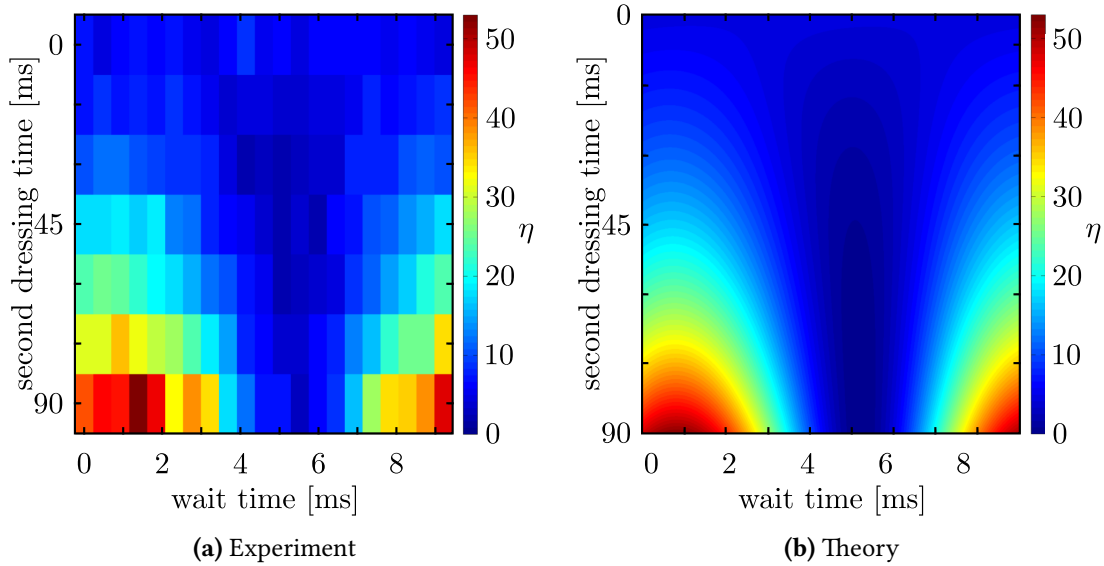


Fig. II.4.5. Experimental and theoretical atom number in the side modes for fixed first dressing time depending on wait and second dressing time. **a)** Shown is the outcome of a measurement analogous to Fig.II.4.4a, but in colour code and with more intermediate time steps for $DT2$. **b)** The result of a numerical calculation using the theory of Ch.I qualitatively reproduces the experimental observations. The theoretical result shows perfect reversal of the SCC which is not observed in the experiment.

II.5. $SU(1,1)$ -interferometer in the depletion regime

The theory used so far is only valid in the non-depletion regime (nd), meaning the pump mode $|0\rangle$ holds much more atoms than the side modes $|\uparrow\rangle$ and $|\downarrow\rangle$ at all times. The complete SCC theory (ct) from Ch.I was approximated by Equ.II.3.1.

In this section we want to enter the depletion regime and therefore have to use the complete SCC theory. Figure II.5.1 illustrates the increasing difference between the two theories for growing dressing times. The blue curves emerge from numerical calculations employing the full Hamiltonian. The dotted red lines are fits to this using the ideal non-depletion regime theory. We see that the theories coincide well for $\tau = 90$ ms, which is the dressing time mostly used in our experiments. Increasing τ leads to deviations of the ct-curves from the sinusoidal form of the nd-theory and the development of a slight asymmetry. This is due to the fact that the number of atoms in the pump mode (n_0) decreases while η increases with ongoing SCC. Therefore the term $\lambda \left(2\hat{n}_0 - 1 + \frac{q}{\lambda} \right) \hat{\eta}$ can not be neglected anymore. This causes an additional phase evolution which develops faster the further the pump is depleted. Note that even for a long dressing time ($\tau = 240$ ms) the SCC cancel and yield a fringe minimum at $\eta \approx 0$. Therefore the second SCC can theoretically still reverse the first.

The numerical calculations were performed using the sequence

$$|\psi\rangle(t_{\text{wt}}, \tau) = e^{-i\hat{H}_{\text{on}}\tau} e^{-i\hat{H}_{\text{off}}t_{\text{wt}}} e^{-i\hat{H}_{\text{on}}\tau} |\psi\rangle_0 \quad (\text{II.5.1})$$

with the Hamiltonians

$$\hat{H}_{\text{on}} = \lambda 2 (\hat{\eta}_+ + \hat{\eta}_-) + \lambda \left(2\hat{n}_0 - 1 + \frac{q_{\text{on}}}{\lambda} \right) \hat{\eta} \quad (\text{II.5.2})$$

$$\hat{H}_{\text{off}} = \lambda 2 (\hat{\eta}_+ + \hat{\eta}_-) + \lambda \left(2\hat{n}_0 - 1 + \frac{q_{\text{off}}}{\lambda} \right) \hat{\eta} \quad (\text{II.5.3})$$

and

$$q_{\text{on}} = 71.89 \text{ Hz/G}^2 \text{B}^2 - \frac{\Omega^2}{4\delta} \quad (\text{II.5.4})$$

$$q_{\text{off}} = 71.89 \text{ Hz/G}^2 \text{B}^2. \quad (\text{II.5.5})$$

The parameter τ denotes the dressing time, t_{wt} the waiting time in the interferometer. The values for B , Ω and N_{tot} coincide with the experimental parameters and the previously determined λ was used (Sec.II.4.2); δ was adjusted such that the numerically calculated fringes resemble the experimental results for small dressing times τ .

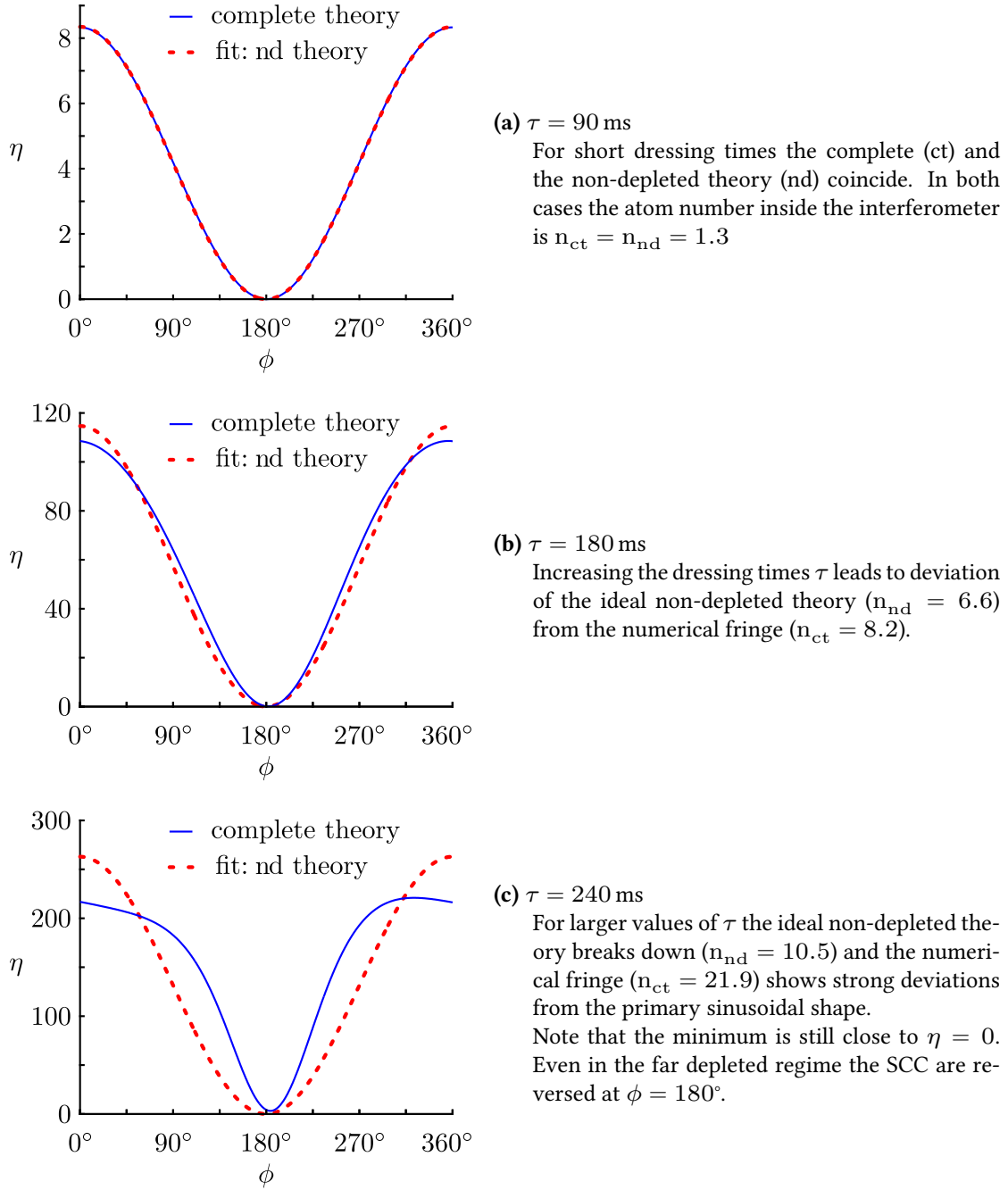


Fig. II.5.1. Theoretical fringes of the $SU(1,1)$ -interferometer for different dressing times. The blue lines are the results of numerical calculations using the complete time evolution in Equ.II.5.1 for the cases **a)** $\tau = 90$ ms, **b)** $\tau = 180$ ms and **c)** $\tau = 240$ ms. The used total atom number was $N_{tot} = 470$ and $\lambda = 1.4$ mHz as obtained in Sec.II.4.2. The fringes in **a)** resemble the experimentally obtained fringe in Fig.II.4.3a. The resulting atom number in the interferometer is denoted as n_{ct} . The red lines correspond to fits applying the ideal non-depleted theory (Equ.II.3.8), which also gives a value for the atom number inside the interferometer labeled with “nd”.

II.5.1. Fisher information

With the break down of the non-depletion regime theory the former used method employing standard error propagation to extract the phase sensitivity is no longer valid, since the slope of the fringe cannot be obtained as before by a fit of Equ.II.3.8. A more general way to get $\Delta\phi$ is by means of the Fisher information F_I . This method will be discussed theoretically with regard to the phase sensitivity in the course of this section. A general discussion can be found in [8, 58]. The Cramér-Rao bound [59] gives a lower limit for the square of the phase sensitivity $\Delta\phi$ which reads

$$(\Delta\phi)^2 \geq \frac{1}{F_I(\phi)} \quad (\text{II.5.6})$$

where $F_I(\phi)$ is the Fisher information with respect to the estimation of ϕ given for a certain input state and phase estimation scenario. With $P(\eta|\phi)$ being the probability to find the side mode population η at the phase value ϕ , $F_I(\phi)$ is defined as

$$F_I(\phi) = \sum_{\eta} \frac{1}{P(\eta|\phi)} \left(\frac{\partial P(\eta|\phi)}{\partial \phi} \right)^2 = \left\langle \left(\frac{\partial}{\partial \phi} \log(P(\eta|\phi)) \right)^2 \right\rangle. \quad (\text{II.5.7})$$

The definition is based on the derivatives of probability amplitudes which can only be calculated exactly if the functional dependence of the probability $P(\eta|\phi)$ on ϕ is known. This makes it experimentally hard to obtain a value for $F_I(\phi)$ since a great amount of data has to be collected in order to have sufficient statistics.

However, an approximate value of $F_I(\phi)$ can be obtained with the squared Hellinger distance dH^2 which is a measure of the statistical distance [60, 61] between two probability distributions $P(\eta|\phi)$ and $P(\eta|\phi + \Delta)$. It is defined as

$$dH_{\phi, \phi+\Delta}^2 = \frac{1}{2} \sum_{\eta} \left[\sqrt{P(\eta|\phi)} - \sqrt{P(\eta|\phi + \Delta)} \right]^2. \quad (\text{II.5.8})$$

The zeroth and first order of the Taylor expansion of dH^2 vanish for small Δ , resulting in

$$\begin{aligned} dH_{\phi, \phi+\Delta}^2 &\approx \frac{1}{8} \sum_{\eta} \left[P(\eta|\phi) \cdot \left(\frac{1}{P(\eta|\phi)} \frac{\partial P(\eta|\phi)}{\partial \phi} \right)^2 \right] \cdot \Delta^2 + \mathcal{O}(\Delta^3) \\ &\approx \frac{1}{8} F_I(\phi) \cdot \Delta^2. \end{aligned} \quad (\text{II.5.9})$$

This yields the connection between the squared Hellinger distance and the Fisher information:

$$F_I(\phi) \approx 8 \frac{dH_{\phi, \phi+\Delta}^2}{\Delta^2}. \quad (\text{II.5.10})$$

The calculation of the theoretical F_I is done in the following way.

A constant dressing time τ and waiting times t_{wt} varied in small steps are used in a numerical equivalent of Equ.II.5.1 to calculate $|\psi\rangle(t_{\text{wt}}, \tau)$. The waiting time t_{wt} is transferred to a phase ϕ giving $|\psi\rangle(\phi)$. The time steps of t_{wt} lead to small changes Δ in the interferometric phase. The probability distributions for the side mode population are then given by

$$P(\eta|\phi) = (\langle \eta | \psi \rangle(\phi))^2. \quad (\text{II.5.11})$$

The squared Hellinger distance for every pair of two adjacent probability distributions is calculated according to Equ.II.5.8. The result is used to calculate F_I with Equ.II.5.10 and the consequent phase sensitivity $\Delta\phi = \frac{1}{\sqrt{F_I}}$.

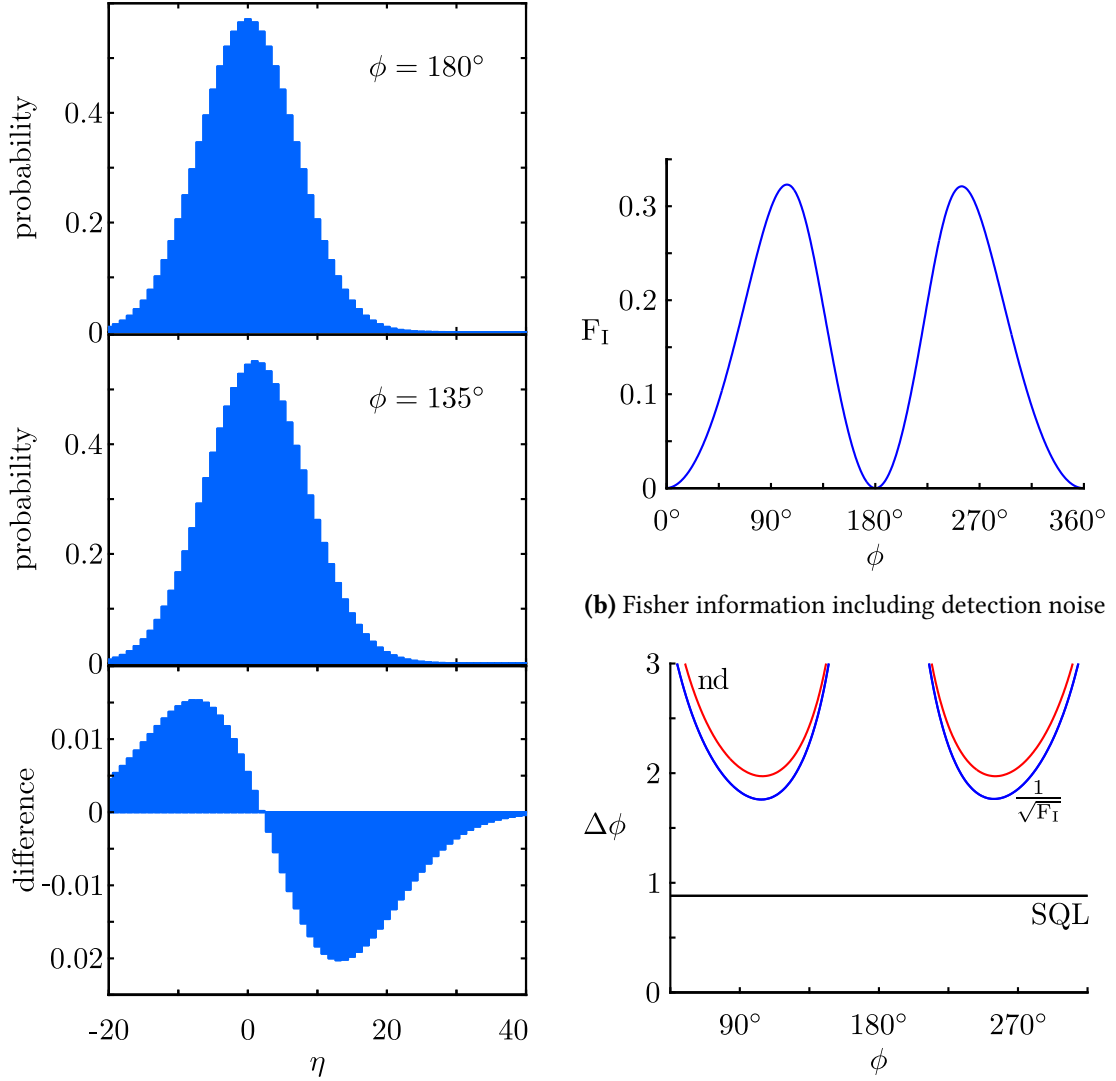
The Figures II.5.2, II.5.3 and II.5.4 show examples for the probability distributions, Fisher information and the resulting phase sensitivities for different dressing times τ . The shown results correspond to the three examples in Fig.II.5.1. The probability distributions were convoluted with a Gaussian function of width $\sigma = \sqrt{2} 4.8$ to account for the detection noise of both side modes in our experiment. For comparison, the red curves represent the phase sensitivity obtained from the non-depleted theory via error propagation with identical noise (Equ.II.3.14) and the same side mode population n_{ct} inside the interferometer.

In the non-depletion regime (Fig.II.5.2) the numerically calculated phase sensitivity does not beat the SQL. This is due to the effect of detection noise, which cannot be removed in this method for detection of the Fisher information. The divergence occurring at $\phi = 180^\circ$ is reproduced in the non-depleted theory with noise (Fig.II.3.4a).

Increasing the dressing time τ to 180 ms (Fig.II.5.3) causes the minimum of $\Delta\phi$ to surpass the SQL despite of the noise. In contrast to the non-depletion theory the phase sensitivity calculated with the Fisher information is no longer symmetric around $\phi = 180^\circ$.

An even longer dressing time of $\tau = 240$ ms (Fig.II.5.4) leads to a further increase in the phase sensitivity. The important difference to the non-depleted theory with detection noise is that the range in which the $\Delta\phi$ surpasses the SQL is broadened.

The probability distributions $P(\eta|\phi)$ for the entire fringes and the three different dressing times $\tau = 90$ ms, $\tau = 180$ ms and $\tau = 240$ ms are shown in Fig.II.5.5. The red line corresponds to the mean value of η in the course of the phase. These plots show the development of an asymmetry of the distribution with increasing dressing time, which explains the asymmetric behaviour of the interferometer at longer evolution times.

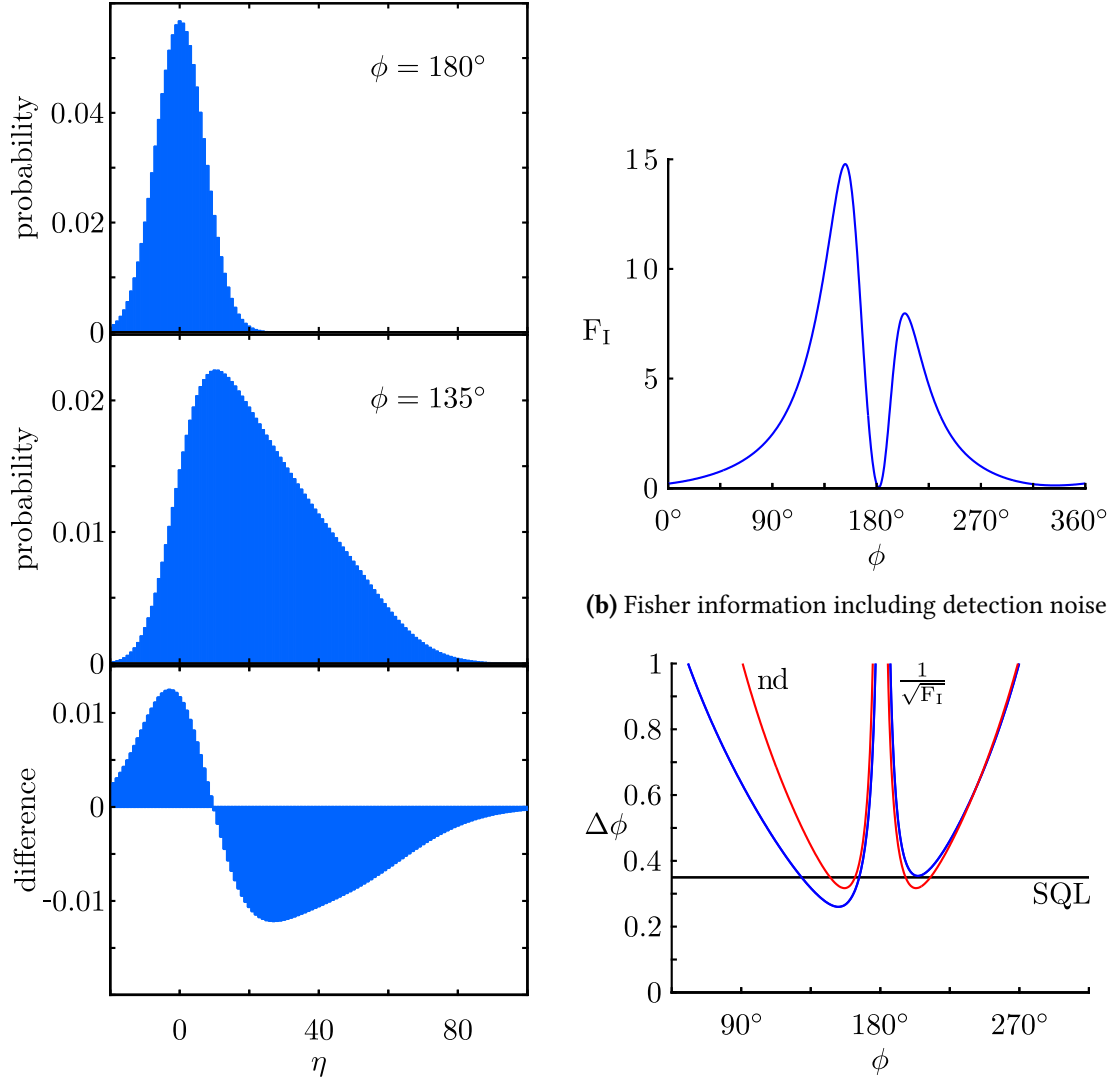


(a) Probability distributions of the side mode population η at the output of the interferometer for $\phi = 180^\circ$ (top) and $\phi = 135^\circ$ (middle) and the difference of their square roots (bottom). The histograms were chosen as examples to illustrate their different shape and the difference of their square roots. The actual phase step for the calculation of the Hellinger distance was $\Delta = 0.6^\circ$.

(c) Phase sensitivity $\Delta\phi$ calculated with the Fisher information F_I (blue) and the ideal non-depleted theory (red). In both cases the detection noise of $\sigma = 7$ is included.

Fig. II.5.2. Probability distributions and phase sensitivity in the non-depleted regime ($\tau = 90$ ms, corresponds to Fig.II.5.1a including detection noise). **a)** The histograms were obtained using Equ.II.5.1 and convoluted with a Gaussian of width $\sigma = 7$ to include our detection noise. **b)** To calculate the Fisher information F_I Equ.II.5.8 and II.5.10 were used. **c)** The blue line represents the phase sensitivity calculated with F_I , the red line the ideal non-depleted theory (Equ.II.3.14) with the same detection noise and mean atom number in the side modes inside the interferometer $n_{ct} = 1.3$. The respective SQL is depicted by the black line.

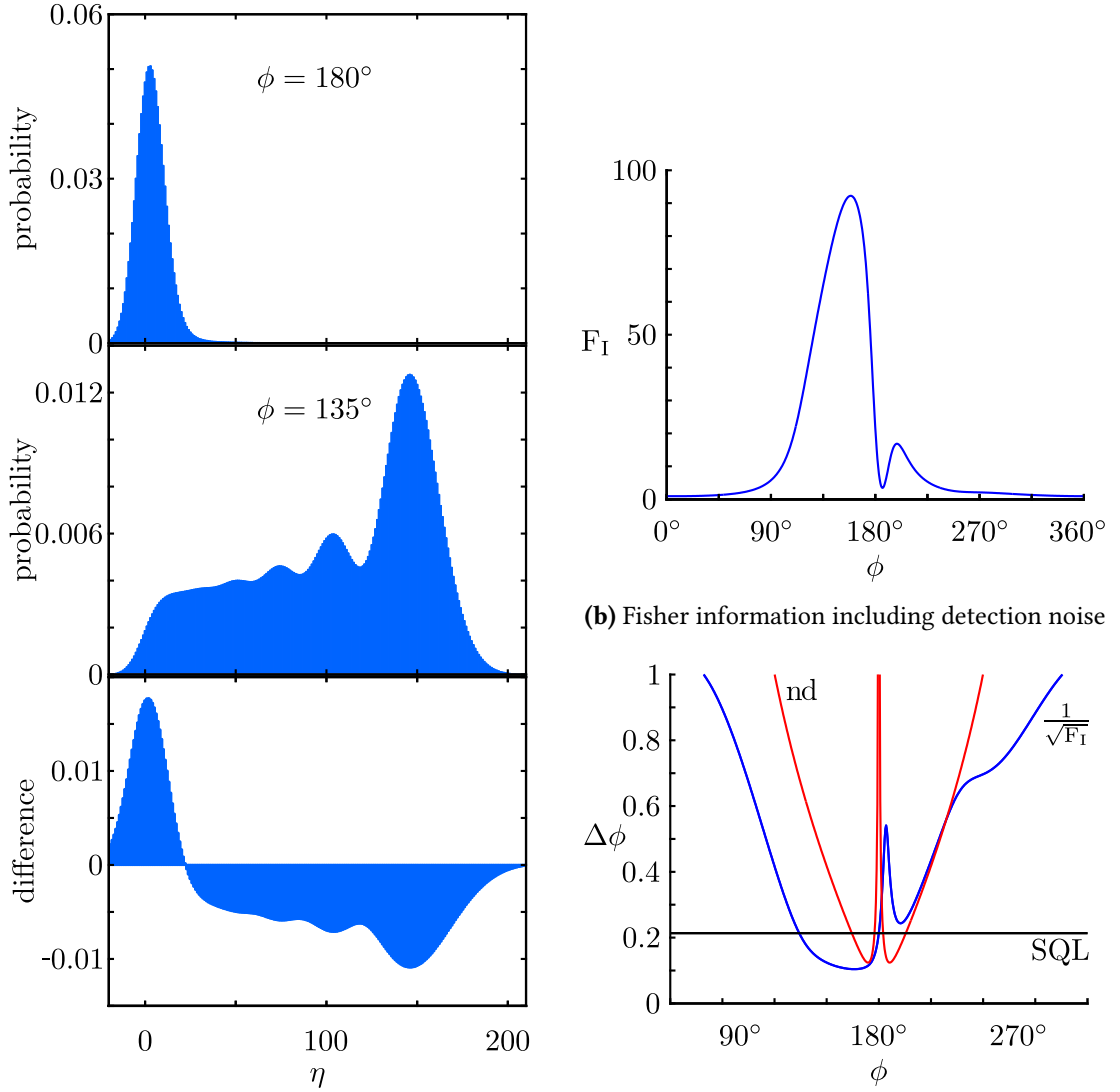
The numerical results show that a sensitivity beyond the SQL is not attainable with our current detection noise for small values of n .



(a) Probability distributions of the side mode population η at the output of the interferometer for $\phi = 180^\circ$ (top) and $\phi = 135^\circ$ (middle) and the difference of their square roots (bottom). The histograms were chosen as examples to illustrate their different shape and the difference of their square roots. The actual phase step for the calculation of the Hellinger distance was $\Delta = 0.6^\circ$. (b) Phase sensitivity $\Delta\phi$ calculated with the Fisher information F_I (blue) and the ideal non-depleted theory (red). In both cases a detection noise of $\sigma = 7$ is included.

Fig. II.5.3. Probability distributions and phase sensitivity in the crossover between non-depleted and depleted regime ($\tau = 180$ ms, corresponds to Fig.II.5.1b including detection noise). The procedure and all the parameters, except for τ , are identical to the ones in Fig.II.5.2. Due to the increased τ the mean atom number in the side modes inside the interferometer is $n_{ct} = 8.2$ (Fig.II.5.1b).

The maximal Fisher information increases and the corresponding phase sensitivity surpasses the SQL. This results from an increased value of n leading to a smaller influence of the detection noise. The observed asymmetry is due to the increased effect of the additional phase term neglected in the ideal non-depleted theory.



(a) Probability distributions of the side mode population η at the output of the interferometer for $\phi = 180^\circ$ (top) and $\phi = 135^\circ$ (middle) and the difference of their square roots (bottom). The histograms were chosen as examples to illustrate their different shape and the difference of their square roots. The actual phase step for the calculation of the Hellinger distance was $\Delta = 0.6^\circ$. (c) Phase sensitivity $\Delta\phi$ calculated with the Fisher information F_I (blue) and the ideal non-depleted theory (red). In both cases a detection noise of $\sigma = 7$ is included.

Fig. II.5.4. Probability distributions and phase sensitivity deep in the depleted regime ($\tau = 240$ ms, corresponds to Fig.II.5.1c including detection noise). The procedure and all the parameters, except for τ , are identical to the ones in Fig.II.5.2. Due to the increased τ the mean atom number in the side modes inside the interferometer is $n_{ct} = 21.9$ (Fig.II.5.1b). In comparison to Fig.II.5.3 the maximal Fisher information increases further and the region where the corresponding phase sensitivity surpasses the SQL broadens. The asymmetry of the fringe is reflected strongly onto the shape of the Fisher information and phase sensitivity.

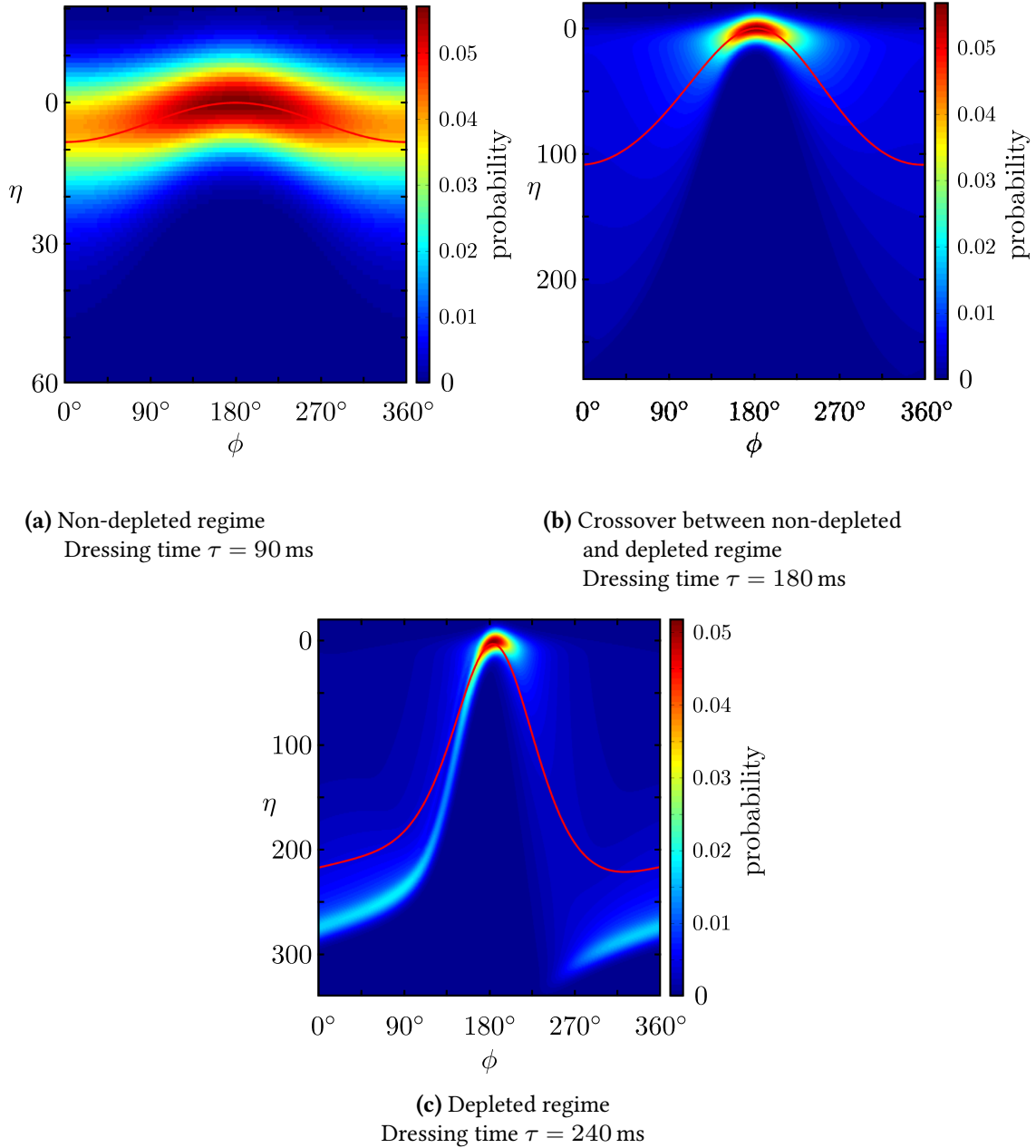


Fig. II.5.5. Probability distributions of the side mode population η at the output of the interferometer for different dressing times and $N_{\text{tot}} = 470$ in the range $\phi = 0^\circ \dots 360^\circ$. The numerical calculations were done using the complete theory. The histograms shown in Fig.II.5.2, II.5.3 and II.5.4 are equivalent with these data sets. The red lines show the expectation value of the complete theory (blue lines in Fig.II.5.1). The colour codes the probability and the y-axes were adjusted for better visibility to the relevant range of η .

II.5.2. Experimental results

To obtain an experimental result for the phase sensitivity with help of the Fisher information F_I , the probability distributions of η in the course of an interferometric fringe have to be determined.

According to Equ.II.5.10 the Fisher information $F_I(\phi)$ at the phase value ϕ can be calculated from the squared Hellinger-distance dH^2 between two probability distributions, separated by an infinitesimal Δ . Two distributions cannot be distinguished with certainty for arbitrarily small Δ in the experiment since the exact probabilities can only be approximated due to finite statistics within a reasonable measurement time.

A workaround is given by Equ.II.5.9. In a small region Δ around a reference phase ϕ_{ref} the Hellinger distance is described by a parabola with curvature $F_I/8$.

The probability distributions for several closely separated points on the fringe are measured in the experiment. One of them is chosen as the reference. The squared Hellinger distances from this point to the neighbouring phases are calculated with Equ.II.5.8 and plotted versus the corresponding phase distance to the reference $\Delta = \phi_{\text{ref}} - \phi_i$ (Fig.II.5.6b). A fit of Equ.II.5.9 gives the curvature of the resulting parabola. Out of this the Fisher information is calculated.

The data obtained in a measurement with $\tau = 90$ ms (in the depletion regime) with a post selected total atom number of $N_{\text{tot}} = 460 \dots 490$ is used to illustrate the procedure. Figure II.5.6a depicts the probability distributions for $\phi = 136^\circ$ and $\phi = 90^\circ$ and the difference of their square roots. The histogram for $\phi = 136^\circ$ is used as reference to determine the squared Hellinger distances shown in Fig.II.5.6b. A fit of the equation

$$dH^2 = a(b - \Delta)^2 + c \quad (\text{II.5.12})$$

yields the curvature used to calculate the value for the Fisher information (red data points in Fig.II.5.6c). The other points represent the F_I determined in an analogue way but with a different choice of the reference histograms for the respective phase ϕ_{ref} .

The best experimentally extracted Fisher information of $F_I = 0.36 \pm 0.06$ is in good agreement with the theoretical prediction of $F_I = 0.32$. This demonstrates the validity of the Fisher information method in this situation.

The corresponding phase sensitivity is $\Delta\phi = 1/\sqrt{F_I} = 1.7 \pm 0.1$. The side mode population inside the interferometer is $n = 1.3 \pm 0.1$ yielding an SQL of $1/\sqrt{n} \approx 0.9$. The phase sensitivity determined with the Fisher information does not surpass the SQL. However, this is not expected in the non-depletion regime with small n since the effect of detection noise cannot be removed in this method.

Determining the phase sensitivity analogue to the procedure in Sec.II.4.2 yields the better value

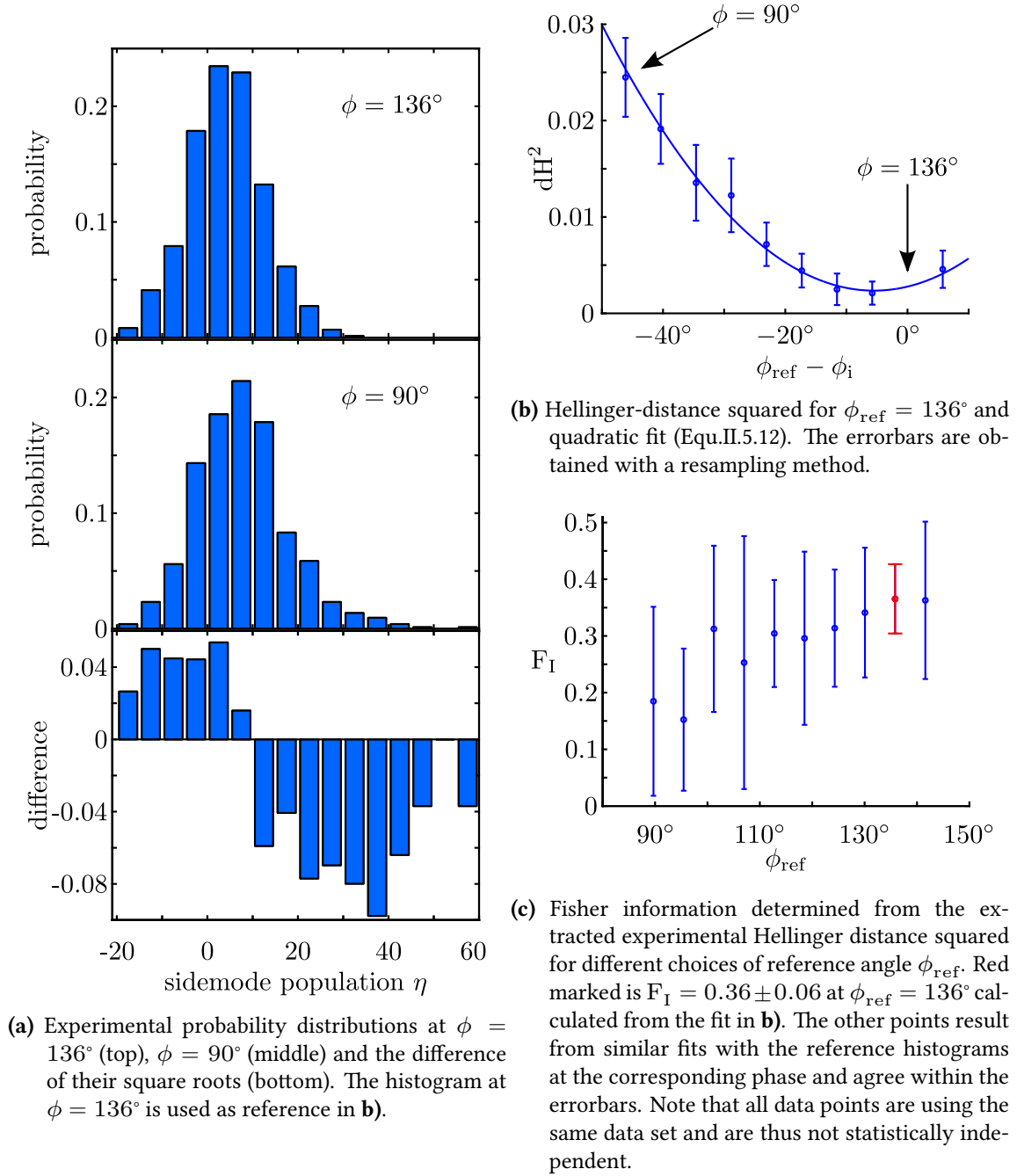


Fig. II.5.6. Experimental probability distribution, Hellinger distance squared and Fisher information in the non-depleted regime. The data was measured with a dressing time of $\tau = 90$ ms. The total atom number was post-selected to $N_{\text{tot}} = 460 \dots 490$. The best experimentally extracted Fisher information of $F_I = 0.36 \pm 0.06$ is in agreement with the best theoretical result of $F_I = 0.32$ in Fig.II.5.2. This demonstrates the validity of the Fisher information method in this situation.

II. *SU(1,1)*-interferometer

$\Delta\phi \approx 1.0 \pm 0.2$ at the same ϕ_{ref} . The reason for this is the correction of the variance by subtracting the detection noise.

The numerical results show that the interferometric sensitivity can be further improved for larger side mode population when the $SU(1,1)$ theory breaks down. In the depleted regime, the region where the SQL is surpassed is broader compared to the result of the $SU(1,1)$ theory with the same n and detection noise. This may allow an easier experimental detection of the phase sensitivity below the SQL. However, the numerical results predict a reversal of the SCC at the fringe minimum that is more effective than the one observed in the experiment. This has to be overcome before we can extend the analysis via Hellinger distance and Fisher information to the depleted regime.

Summary

In this thesis the dynamics of the internal spin degree of freedom of atoms and the realisation of a non-linear interferometer were studied in a spinor Bose-Einstein condensate of ^{87}Rb .

The first chapter was dedicated to the mentioned dynamics emerging from the process of spin-changing collisions.

We discussed the underlying theory and the effect of magnetic fields which inhibit the process at larger magnetic fields due to the second order Zeeman splitting. Microwave dressing was introduced as a tool to overcome the inhibition of the SCC due to the quadratic Zeeman effect and gain control over them. Numerical calculations with the derived Hamiltonian were performed to analyse the SCC-evolution dependent on the initial conditions.

We found a good qualitative agreement between the experimentally measured SCC-evolution and theory. We observed significant changes in the atom number distribution in the side modes, which resembles the one of a thermal state for small evolution times. In the further course of the evolution broadening and narrowing of the distribution occurs.

We experimentally demonstrated that the magnetisation is conserved during an SCC-evolution by the strong squeezing of its variance, indicating that the atoms in the side modes are always produced in pairs. The first chapter was concluded with a discussion about the dependence of the SCC-evolution on the detuning of the microwave employed for dressing of the atomic levels.

In the second chapter we discussed the realisation of an active non-linear interferometer in the non-depleted regime by two subsequent equal periods of SCC-evolutions. In this interferometer, the relative phase between the pump and side modes is observed as an amplification or reduction of the side mode population by the second SCC.

The theory was approached by the introduction of the $SU(1,1)$ -group. We saw that the $SU(1,1)$ -interferometer can be visualised by Lorentz boosts and rotations on a hyperbolic surface in conceptual analogue to the rotations on a Bloch sphere in the $SU(2)$ -group description of the Mach-Zehnder interferometer. The phase sensitivity $\Delta\phi$ with and without additional noise was discussed theoretically using error propagation.

The experimental results for $\Delta\phi$ indicate that the $SU(1,1)$ -interferometer realised with our setup

might allow to surpass the SQL. A measurement revealed that the first SCC are not entirely reversed as expected from the ideal non-depleted theory. Reasons for this may be atom loss and dephasing of the three modes during the experiment. The reduction of the detection noise is planned in order to improve the accuracy of the phase sensitivity. To achieve this, preparations to include precise atom number counting detection [62] in our current experimental setup are in progress.

In the last part we used numerical calculations under the consideration of experimentally comparable detection noise to analyse the interferometric fringes and resulting phase sensitivities in the depleted regime. The concept of the Hellinger-distance and Fisher information was introduced for the analysis. The simulations show that an enhanced performance of the interferometer in the depleted regime is achievable despite of our current detection noise. A first analysis of experimental data in the non-depleted regime via the Hellinger-distance yielded good agreement with the numerical determined Fisher information.

However, we observed a less effective reversion of the first SCC for longer dressing times in the experiment. This has to be overcome to extend the analysis via Hellinger-distance and Fisher information to the depleted regime.

We demonstrated the first realisation of an active non-linear interferometer with atoms. The strong amplification by the parametric process allows the detection of signals even for small side mode populations n inside the interferometer. Hence, already small atom numbers n can be used to extract the phase sensitivity and possibly show Heisenberg scaling ($\Delta\phi \propto 1/n$) if the performance of the interferometer is further increased. Due to the different magnetic sensitivity of the pump and side modes the interferometer can be used for magnetometry.

The presented experimental results for the SU(1,1)-interferometer were obtained in the $F = 1$ manifold. Currently we are investigating the performance of the interferometer in the $F = 2$ manifold where the side mode population due to the SCC grows faster. Therefore the whole interferometric sequence is shorter (≈ 30 ms instead of ≈ 200 ms) and dephasing might have less effect with an increased atom loss as a trade-off.

List of Figures

I.0.1.	Schematic scattering process	3
I.1.1.	Electronic ground state of ^{87}Rb	10
I.1.2.	Linear and quadratic Zeeman effect in $F = 1$	12
I.1.3.	Atomic two level system with incident microwave radiation	13
I.1.4.	Energies of dressed states	15
I.1.5.	Relevant energy shifts for SCC in $F = 1$	17
I.1.6.	Theoretical evolution of the relative population of the side modes for various parameters	19
I.1.7.	Theoretical evolution of variance of side mode population during SCC	20
I.2.1.	Example of an experimental image	21
I.2.2.	Atom number distribution in side modes during SCC-evolution	23
I.2.3.	Suppression of relative fluctuations with spin-changing collisions	25
I.2.4.	SCC evolution depending on microwave detuning in $F = 2$	27
II.0.1.	Mach-Zehnder interferometer	29
II.1.1.	Coherent and number state on Bloch sphere	32
II.1.2.	Mach-Zehnder interferometer sequence on the Bloch sphere	35
II.2.1.	SU(1,1)-coherent and number state on the hyperbolic surface with $\langle \eta \rangle = 2$	42
II.2.2.	SU(1,1)-coherent and number state on the hyperbolic surface with $\langle \eta \rangle = 8$	43
II.3.1.	SU(1,1) interferometer	44
II.3.2.	SU(1,1) interferometer sequence on hyperbolic surface	46
II.3.3.	Occupation and its variance of side mode population for the ideal SU(1,1) interferometer	47
II.3.4.	Phase sensitivity of the ideal SU(1,1) interferometer	49
II.4.1.	Experimental fringes in the SU(1,1)-interferometer	51
II.4.2.	Measured atom number distribution of regions without atoms	53
II.4.3.	Fringe, variance and phase sensitivity of the SU(1,1)-interferometer	55
II.4.4.	Fringe of mean occupancy and variance for varied second dressing time	56

II.4.5.	Experimental and theoretical atom number in the side modes for fixed first dressing time depending on wait and second dressing time	57
II.5.1.	Theoretical fringes of the SU(1,1)-interferometer for different dressing times .	59
II.5.2.	Probability distributions and phase sensitivity in the non-depleted regime . .	62
II.5.3.	Probability distributions and phase sensitivity in the crossover between non-depleted and depleted regime	63
II.5.4.	Probability distributions and phase sensitivity deep in the depleted regime . .	64
II.5.5.	Probability distributions of the side mode population η at the output of the interferometer for different dressing times	65
II.5.6.	Experimental probability distribution, Hellinger distance squared and Fisher information in the non-depleted regime	67

Bibliography

- [1] A. Peters, K. Y. Chung, and S. Chu. “High-precision gravity measurements using atom interferometry”. In: *Metrologia* 38.1 (2001), p. 25.
- [2] P. Aufmuth and K. Danzmann. “Gravitational wave detectors”. In: *New Journal of Physics* 7.1 (2005), p. 202.
- [3] R. Wynands and S. Weyers. “Atomic fountain clocks”. In: *Metrologia* 42.3 (2005), p. 64.
- [4] T. L. Gustavson, P. Bouyer, and M. A. Kasevich. “Precision Rotation Measurements with an Atom Interferometer Gyroscope”. In: *Phys. Rev. Lett.* 78.2046 (11 1997).
- [5] A. D. Cronin, J. Schmiedmayer, and D. E. Pritchard. “Optics and interferometry with atoms and molecules”. In: *Rev. Mod. Phys.* 81 (3 2009), pp. 1051–1129.
- [6] W. Demtröder. *Laserspektroskopie 2. Experimentelle Techniken*. ger. 6. neu bearbeitete und aktualisierte Auflage. SpringerLink : Bücher. Berlin, Heidelberg: Springer, 2013, Online–Ressource (XIV, 575 S. 469 Abb, digital).
- [7] C. M. Caves. “Quantum-mechanical noise in an interferometer”. In: *Phys. Rev. D* 23.1693 (8 1981).
- [8] V. Giovannetti, S. Lloyd, and L. Maccone. “Advances in quantum metrology”. In: *Nat Photon* 5.4 (Apr. 2011), pp. 222–229.
- [9] B. Yurke, S. L. McCall, and J. R. Klauder. “SU(2) and SU(1,1) interferometers”. In: *Phys. Rev. A* 33.4033 (6 1986).
- [10] A. M. Marino, N. V. Corzo Trejo, and P. D. Lett. “Effect of losses on the performance of an SU(1,1) interferometer”. In: *Phys. Rev. A* 86.023844 (2 2012).
- [11] F. Hudelist, J. Kong, C. Liu, J. Jing, Z. Ou, and W. Zhang. “Quantum metrology with parametric amplifier-based photon correlation interferometers”. In: *Nature Communications* 5 (2014).
- [12] M. H. Anderson, J. R. Ensher, M. R. Matthews, C. E. Wieman, and E. A. Cornell. “Observation of Bose-Einstein Condensation in a Dilute Atomic Vapor”. In: *Science* 269.5221 (1995), pp. 198–201.

- [13] K. B. Davis, M. O. Mewes, M. R. Andrews, N. J. van Druten, D. S. Durfee, D. M. Kurn, and W. Ketterle. “Bose-Einstein Condensation in a Gas of Sodium Atoms”. In: *Phys. Rev. Lett.* 75 (22 1995).
- [14] D. M. Stamper-Kurn, M. R. Andrews, A. P. Chikkatur, S. Inouye, H.-J. Miesner, J. Stenger, and W. Ketterle. “Optical Confinement of a Bose-Einstein Condensate”. In: *Phys. Rev. Lett.* 80.2027 (10 1998).
- [15] T.-L. Ho. “Spinor Bose Condensates in Optical Traps”. In: *Phys. Rev. Lett.* 81.742 (4 1998).
- [16] C. K. Law, H. Pu, and N. P. Bigelow. “Quantum Spins Mixing in Spinor Bose-Einstein Condensates”. In: *Phys. Rev. Lett.* 81.5257 (24 1998).
- [17] G. I. Mias, N. R. Cooper, and S. M. Girvin. “Quantum noise, scaling, and domain formation in a spinor Bose-Einstein condensate”. In: *Phys. Rev. A* 77.023616 (2 2008).
- [18] H. Pu, C. K. Law, S. Raghavan, J. H. Eberly, and N. P. Bigelow. “Spin-mixing dynamics of a spinor Bose-Einstein condensate”. In: *Phys. Rev. A* 60.1463 (2 1999).
- [19] A. Widera, F. Gerbier, S. Fölling, T. Gericke, O. Mandel, and I. Bloch. “Precision measurement of spin-dependent interaction strengths for spin-1 and spin-2 ^{87}Rb atoms”. In: *New Journal of Physics* 8.8 (2006), p. 152.
- [20] H. K. Pechkis, J. P. Wrubel, A. Schwettmann, P. F. Griffin, R. Barnett, E. Tiesinga, and P. D. Lett. “Spinor Dynamics in an Antiferromagnetic Spin-1 Thermal Bose Gas”. In: *Phys. Rev. Lett.* 111.025301 (2 2013).
- [21] H. Schmaljohann, M. Erhard, J. Kronjäger, M. Kottke, S. van Staa, L. Cacciapuoti, J. J. Arlt, K. Bongs, and K. Sengstock. “Dynamics of $F=2$ Spinor Bose-Einstein Condensates”. In: *Phys. Rev. Lett.* 92.040402 (4 2004).
- [22] S. R. Leslie, J. Guzman, M. Vengalattore, J. D. Sau, M. L. Cohen, and D. M. Stamper-Kurn. “Amplification of fluctuations in a spinor Bose-Einstein condensate”. In: *Phys. Rev. A* 79.043631 (4 2009).
- [23] C. S. Gerving, T. M. Hoang, B. J. Land, M. Anquez, C. D. Hamley, and M. S. Chapman. “Non-equilibrium dynamics of an unstable quantum pendulum explored in a spin-1 Bose-Einstein condensate”. In: *Nature Communications* 3 (2013).
- [24] C. Gross, H. Strobel, E. Nicklas, T. Zibold, N. Bar-Gill, G. Kurizki, and M. K. Oberthaler. “Atomic homodyne detection of continuous-variable entangled twin-atom states”. In: *Nature* 480.7376 (2011), pp. 219 –233.

-
- [25] C. Klempt, O. Topic, G. Gebreyesus, M. Scherer, T. Henninger, P. Hyllus, W. Ertmer, L. Santos, and J. J. Arlt. "Parametric Amplification of Vacuum Fluctuations in a Spinor Condensate". In: *Phys. Rev. Lett.* 104.195303 (19 2010).
- [26] C. D. Hamley, C. S. Gerving, T. M. Hoang, E. M. Bookjans, and M. S. Chapman. "Spinematic squeezed vacuum in a quantum gas". In: *Nature Physics* 8.4 (Feb. 2012), pp. 305–308.
- [27] S. Haroche and J.-M. Raimond. *Exploring the quantum. atoms, cavities and photons.* eng. Repr. Oxford graduate texts. Oxford [u.a.]: Oxford Univ. Press, 2008, X, 605 S.
- [28] M. Ueda and M. Koashi. "Theory of spin-2 Bose-Einstein condensates: Spin correlations, magnetic response, and excitation spectra". In: *Phys. Rev. A* 65.063602 (6 2002).
- [29] E. G. M. van Kempen, S. J. J. M. F. Kokkelmans, D. J. Heinzen, and B. J. Verhaar. "Interisotope Determination of Ultracold Rubidium Interactions from Three High-Precision Experiments". In: *Phys. Rev. Lett.* 88.093201 (9 2002).
- [30] J Rogel-Salazar. "The Gross-Pitaevskii equation and Bose-Einstein condensates". In: *European Journal of Physics* 34.2 (2013), p. 247.
- [31] H. Strobel. "Quantum Spin Dynamics in Mesoscopic Bose-Einstein Condensates". Diplomarbeit. Universität Heidelberg, 2011.
- [32] J. Heinze, F. Deuretzbacher, and D. Pfannkuche. "Influence of the particle number on the spin dynamics of ultracold atoms". In: *Phys. Rev. A* 82.023617 (2 2010).
- [33] D. A. Steck. *Rubidium 87 D Line Data, revision 2.1.4, 23 December 2010.*
- [34] W. Demtröder. *Experimentalphysik 3. Atome, Moleküle und Festkörper.* ger. 3rd ed. Springer-Lehrbuch ; SpringerLink : Bücher. Berlin, Heidelberg: Springer Berlin Heidelberg, 2005.
- [35] M. O. Scully and M. S. Zubairy. *Quantum optics.* eng. 6. print. Cambridge [u.a.]: Cambridge Univ. Press, 2008, XXI, 630 S.
- [36] D. A. Steck. *Quantum and Atom Optics, revision 0.9.10, 3 April 2014.*
- [37] C. C. Gerry and P. L. Knight. *Introductory quantum optics.* eng. Cambridge: Cambridge Univ. Pr., 2005, XIII, 317 S.
- [38] B. Eiermann. "Kohärente nichtlineare Materiewellendynamik - Helle atomare Solitonen". PhD thesis. Heidelberg, Univ., Diss., 2004.
- [39] A. Weller. "Dynamics and Interaction of Dark Solitons in Bose-Einstein Condensates". PhD thesis. Heidelberg, Univ., Diss., 2009.

- [40] W. Petrich, M. H. Anderson, J. R. Ensher, and E. A. Cornell. “Stable, Tightly Confining Magnetic Trap for Evaporative Cooling of Neutral Atoms”. In: *Phys. Rev. Lett.* 74.3352 (17 1995).
- [41] W. Muessel, H. Strobel, M. Joos, E. Nicklas, I. Stroescu, J. Tomkovič, D. Hume, and M. Oberthaler. “Optimized absorption imaging of mesoscopic atomic clouds”. English. In: *Applied Physics B* 113.1 (2013), pp. 69–73.
- [42] B. Efron and C. Stein. “The Jackknife Estimate of Variance”. In: *The Annals of Statistics* 9.3 (May 1981), pp. 586–596.
- [43] The LIGO Scientific Collaboration. “A gravitational wave observatory operating beyond the quantum shot-noise limit: Squeezed light in application”. In: *Nature Physics* 7 (2011), pp. 962 –965.
- [44] A. Micheli, D. Jaksch, J. I. Cirac, and P. Zoller. “Many-particle entanglement in two-component Bose-Einstein condensates”. In: *Phys. Rev. A* 67.013607 (1 2003).
- [45] N. F. Ramsey. “A Molecular Beam Resonance Method with Separated Oscillating Fields”. In: *Phys. Rev.* 78.695 (6 1950).
- [46] M. A. Nielsen and I. L. Chuang. *Quantum computation and quantum information*. eng. 10. print. Cambridge [u.a.]: Cambridge Univ. Press, 2009, XXV, 676 S.
- [47] M. Fox. *Quantum optics. an introduction*. eng. Reprint. Oxford master series in physics: Atomic, optical, and laser physics 15. Oxford [u.a.]: Oxford Univ. Press, 2011, XVII, 378 S.
- [48] J. M. Radcliffe. “Some properties of coherent spin states”. In: *Journal of Physics A: General Physics* 4.3 (1971), p. 313.
- [49] A. M. Perelomov. “Generalized coherent states and some of their applications”. In: *Soviet Physics Uspekhi* 20.9 (1977), p. 703.
- [50] T. Zibold. “Classical bifurcation and entanglement generation in an internal bosonic Josephson junction”. eng. PhD thesis. Heidelberg, Univ., Diss., 2012, Online–Ressource (III, 78 S.)
- [51] C Brif, A Vourdas, and A Mann. “Analytic representations based on SU (1,1) coherent states and their applications”. In: *Journal of Physics A: Mathematical and General* 29.18 (1996), p. 5873.
- [52] C. C. Gerry and J Kiefer. “Classical and quantum Liouville dynamics of SU(1,1) coherent states”. In: *Journal of Physics A: Mathematical and General* 24.15 (1991), p. 3513.
- [53] X. Wang, B. C. Sanders, and S. hua Pan. “Entangled coherent states for systems with SU (2) and SU (1,1) symmetries”. In: *Journal of Physics A: Mathematical and General* 33.41 (2000), p. 7451.

-
- [54] K. Berrada, M. E. Baz, and Y. Hassouni. “On the construction of generalized SU(1,1) coherent states”. In: *Reports on Mathematical Physics* 68.1 (2011), pp. 23–35.
- [55] D. Li, C.-H. Yuan, Z. Y. Ou, and W. Zhang. “The phase sensitivity of an SU(1,1) interferometer with homodyne detection”. In: *eprint: arXiv/1305.4769* (2013).
- [56] F. Dalfovo, S. Giorgini, L. P. Pitaevskii, and S. Stringari. “Theory of Bose-Einstein condensation in trapped gases”. In: *Rev. Mod. Phys.* 71 (3 1999), pp. 463–512.
- [57] D. Linnemann. “Realization of an SU(1,1) Interferometer with Spinor Bose-Einstein Condensates”. Masterarbeit. Universität Heidelberg, 2014.
- [58] Z. Hradil and J. Řeháček. “Quantum interference and Fisher information”. In: *Physics Letters A* 334.4 (2005), pp. 267–272.
- [59] H. Cramér. *Mathematical methods of statistics*. eng. 11. print. Princeton mathematical series 9. Princeton: Princeton Univ. Pr., 1966, XVI, 574 S.
- [60] Z. Bar-Yossef, T. Jayram, R. Kumar, and D. Sivakumar. “An information statistics approach to data stream and communication complexity”. In: *Journal of Computer and System Sciences* 68.4 (2004). Special Issue on {FOCS} 2002, pp. 702–732.
- [61] S. Luo and Q. Zhang. “Informational distance on quantum-state space”. In: *Phys. Rev. A* 69.032106 (3 2004).
- [62] D. B. Hume, I. Stroescu, M. Joos, W. Muessel, H. Strobel, and M. K. Oberthaler. “Accurate Atom Counting in Mesoscopic Ensembles”. In: *Phys. Rev. Lett.* 111 (25 2013).

Danksagung

Ich möchte mich bei Herrn Prof. Markus Oberthaler bedanken. Angefangen von der Betreuung in Übungsgruppen und während meiner Bachelorarbeit bis hin zur Aufnahme in seine Gruppe für diese Arbeit war seine angenehme und lockere Art stets motivierend. Mein Interesse an der Quantenmechanik ist zweifelsfrei auch seinem Engagement zu verdanken.

Ich danke Herrn Prof. Selim Jochim für die Übernahme der Zweitkorrektur dieser Arbeit und den stets freundlichen Kontakt im Verlauf meines Studiums.

Großer Dank geht an Daniel, Wolfgang und Helmut für die Aufnahme in die BEC-Gruppe, die gemeinsame Zeit und das ausführliche Beantworten meiner vielen Fragen, sowie das Korrekturlesen meiner Arbeit. Daniel möchte ich einen besonderen Dank aussprechen für die Zeit im Labor und das Einlernen in den experimentellen Aufbau.

Den NaLis danke ich für ihre jederzeit optimistisch-humorvolle Art, sei es im Labor, Büro oder beim gemeinsamen Abendessen mit Erfrischung im Botanik.

AEgIS und ATTA danke ich für den, wenn auch seltenen, immer angenehmen Umgang.

Für die vielen Päckchen, Briefe und Beiträge zu meinem leiblichen Wohl danke ich meiner Oma Esther. Meinen Eltern danke ich für ihre Unterstützung während meines Studiums, der Zeit davor und der Zeit, die noch kommt.

Erklärung:

Ich versichere, dass ich diese Arbeit selbstständig verfasst habe und keine anderen als die angegebenen Quellen und Hilfsmittel benutzt habe.

Heidelberg, den 18. Juni 2014

.....